Effects of Spin-Orbit Interaction on Quantum States in Semiconducting Dots and Wires

INAUGURALDISSERTATION

zur

Erlangung der Würde eines Doktors der Philosophie

vorgelegt der

Philosophisch-Naturwissenschaftlichen Fakultät

der Universität Basel

von

Marcel Serina

aus Trnava, Slowakei

Basel, 2018

Genehmigt von der Philosophisch-Naturwissenschaftlichen Fakultät auf Antrag von

Prof. Dr. Daniel Loss

Prof. Dr. Jaroslav Fabian

Basel, den 18. September 2018

Prof. Dr. Martin Spiess
Dekan

Acknowledgments

First of all I would like to thank to my supervisor Prof. Daniel Loss for guiding me through my studies for the past four years. It was a pleasure and a great honour to work with him on the cutting-edge theoretical problems. Daniel kept suprising me by his exceptionally broad view of the condensed matter theory in strong connection to contemporary expemeriments.

I am also very grateful to Prof. Jaroslav Fabian for accepting the duty to co-referee my thesis and be a member of the examination committee.

This work was made possible due to my collaboration with Christoph Klöffel, Jelena Klinovaja, Peter Stano, Chen-Hsuan Hsu, Leon C. Camenzind and Dominik M. Zumbühl. I am very grateful to all of you and it was a great pleasure to work with you.

I would also like to thank to all my colleagues from the group which created an outstanding social climate necessary for my work, namely Ehud Amitai, Pavel Aseev, Prof. Christoph Bruder, Denis Chevallier, Victor Kooi Ming Chua, Oindrila Deb, Sebastián Díaz, Olesia Dmytruk, Tamás Heidekker Galambos, Silas Hoffman, Adrian Hutter, Christoph Klöffel, Martin Koppenhöfer, Viktoriia Kornich, Katharina Laubscher, Axel U. J. Lode, Niels Loerch, Franziska Maier, Tobias Meng, Dmitry Miserev, Kouki Nakata, Simon Nigg, Andreas Nunnenkamp, Christoph Orth, Christina Psaroudaki, Marko Rancic, Christopher Reeg, Alexandre Roulet, Arijit Saha, Thomas Schmidt, Tibor Sekera, Pawel Szumniak, Manisha Thakurathi, Rakesh Tiwari, Luka Trifunovic, Stefan Walter, James Wootton, Yanick Volpez and Alexander Zyuzin.

Without the outstanding pedagogical performance of my former supervisors and professors in Bratislava I would never decide to continue my career towards the PhD studies in condensed matter theory. So my gratitude and deep appreciation belongs to Andrej Gendiar, Richard Hlubina, Martin Moško, Marián Fecko, Martin Mojžiš, Vladimír Černý and Pavol Zlatoš.

I would also like to thank to all my friends which have been around me and helped me to reach my goals. I am grateful to my former classmates from grammar school in Trnava and from bachelor and master studies of physics in Bratislava. Special thanks goes to Peter Gálik and Filip Krištofiak for sharing with me the passion for natural wine, science and political discussions, Christoph Orth and Yemliha Bilal for being my mountaineering and hiking buddies and to Stefan Degen for insights into the Swiss life and society.

Finally, I would like to thank to my parents, since all this was made possible thanks to them and they supported me at all times.

Summary

Steming from the pivotal idea of Feynman to use quantum degrees of freedom for computing substantial effort in condensed matter theory is nowadays aimed at the theoretical understanding of systems which can be harnessed as solid state qubits. As many of solid state systems under investigation like Josephson junctions and cold atoms have for the time being clear limit in scaling towards reliable many-qubit architectures we aim our effort towards one of the simplest qubits at hand being lateral quantum dots.

Lateral quantum dots are fabricated by confining electron or hole two-dimensional electron gas in the semiconductors by patterned metallic gates and their quantum states can be understood in terms of discrete harmonic-oscillator-like states. In order to operate such qubits, it is vital to understand how states interact with external fields applied in the sample, as well as describe all the effects coming from hosting heterostructure, mainly effects of spin-orbit interaction in the semiconductors.

As introduced by Rashba and Dresselhaus spin-orbit interaction in semiconductors can be understood within the framework of $\mathbf{k} \cdot \mathbf{p}$ theory and considering the point group of the specific lattice structure.

In the second chapter of this thesis, we employ this approach in order to describe cross-coupling of hybrid qubit to multiple other types of qubits. We start from the $\mathbf{k} \cdot \mathbf{p}$ description of the underlying semiconductor, and we introduce a capacitive coupling via the floating gate adjacent to both qubits. We show that sufficient coupling strength can be provided in this scenario between the two hybrid qubits, as well as between the hybrid qubit and single-triplet, single-spin qubit.

In the third chapter of this thesis, we provide a detailed theory in order to understand g-factor contributions for the electrons in GaAs. Based on the theory of invariants, we use a Hamiltonian up to the fourth order in $\mathbf{k}$ including also terms up to the second order in the in- plane magnetic field $\mathbf{B}$. We show that the leading contribution to the g-factor comes from the Rashba term and so-called H_{43} term, which is nowadays not consid-

ered in most of the studies.

The main challenge for spin qubits is to overcome decoherence due to the coupling to external noise. Apart from thorough understanding of all possible sources of local noise, we can also form a new type of qubit as proposed by Kitaev. So-called topological qubits are based on non-local properties of degenerate ground states of topologically non-trivial phases and are inherently immune to all sources of local noise. The main challenge here remains to reliably identify Majorana fermions, which are the manifesatation of topological phase and are used to define topological qubits.

In the fourth chapter of this thesis, we adress this issue by looking at a realistic model of a nanowire hosting Majorana fermions, and try to find other signatures of the topological phase transition, not relying on the presence of Majorana fermions. We find that boundary spin along the direction of the applied magnetic field can be used as a reliable signature of the topological phase transition.

Contents

Contents **vii**

1 Introduction **1**
1.1 Quantum computing 2
1.2 Low dimensional quantum systems: 2DEGs and NWs . . . 4
1.3 Quantum dots and spin qubits 9
1.4 Topological superconductors and Majorana Fermions . . . 14

2 Long-range Interaction Between Charge and Spin Qubits in Quantum Dots **21**
2.1 Introduction 21
2.2 H-H and H-ST coupling 23
2.3 H-LD coupling 30
2.4 Dependence on setup geometries and host materials 33
2.5 Conclusions 36
2.A Derivation of the electron-electron coupling mediated by the floating gate 38
2.B Schrieffer-Wolff transformation 41
2.C Expansion of the interaction potential 42

3 Lateral Quantum Dot in a Strong In-plane Magentic Field **44**
3.1 Introduction 45
3.2 Definitions and methods 47
3.3 The perturbation theory 56
3.4 Results for g-factor corrections 60
3.5 Conclusions 70
3.A List of the off-diagonal effective Zeeman terms 71
3.B Derivation of the spin-dependent corrections 72
3.C List of all dimensionless constants 83
3.D Symmetric quantum well 86
3.E Magnetic-field-dependent corrections 88

3.F Mixed contribution example 90

4 Boundary Spin Polarization as a Robust Signature of a Topological Phase Transition 92
4.1 Introduction 93
4.2 Model 95
4.3 Signature of topological phase transition 98
4.4 Conclusions 102
4.A Results for boundary spin component S^x_{Lm} and boundary charge ρ_{Lm} 103
4.B Local properties of boundary spin component $\tilde{S}^z_{Lm}$ 104
4.C Effect of on-site disorder - stability of topological phase transition signature in $\tilde{S}^z_{Lm}$ 105
4.D Boundary spin $\tilde{S}^z_{Rm}$ at the boundary between topological and trivial phases 109
4.E Signatures of topological phase transition in bulk values of spin 111

Bibliography 113

CHAPTER 1

Introduction

In this Introduction we would like to recall the basic concepts relevant for our work and put our research into a broader context.

In the first section, we review the concept of quantum computing, motivate its vital importance for future applications and give a short overview of quantum systems harnessed nowadays for this purpose.

In the second section, we move our attention to low-dimensional quantum systems, namely two-dimensional electron gases (2DEGs) and nanowires (NWs). We first give a broader overview of various platforms and materials used to fabricate these systems and we motivate why these systems are supposed to be ideal platforms for quantum computation. We then introduce basic theoretical concepts to describe these systems and review the current state-of-the-art in this field.

In the third section, we would like to introduce the concept of a quantum dot (QD) as a zero-dimensional quantum system and focus on their realizations in 2DEGs and NWs. Based on that, we review the notion of spin qubit, give an overview of their properties, introduce terminology and also characterize them as a platform for quantum computing.

In the fourth section, we introduce the notion of topological phases and argue, why such systems should host an ideal candidate for qubit immune against local noise. We give an overview of platforms for topological quantum computation and introduce the Kitaev model of topological superconductor. Based on that, we describe realistic systems currently used to realize topological superconductors in proximitized NWs.

1.1 Quantum computing

The notion of quantum computing was pioneered by R.P. Feynman in his seminal paper [1] and even before at his lecture "There's Plenty of Room at the Bottom" in 1959. He introduced the idea that in order to simulate quantum systems efficiently, one should also rely on using quantum degrees of freedom, and therefore build a *quantum* computer. He proposed a lattice of nearest-neighbour interacting spins 1/2, which is expected to simulate any given quantum system. Since that time quantum computing expanded into a field on its own.

In simulation of interacting many-body quantum systems, we have to face the following issue. Imagine we have a system composed of the N interacting spin-1/2 particles and thus the dimension of the total Hilbert space is 2^N. In order to diagonalize such Hamiltonian by classical computer and draw some conclusions about the thermodynamical limit, one needs to overcome the exponential growth of Hilbert space with system size by the plethora of specific methods. Feynmans idea to overcome this issue was to use quantum systems *themselves* to simulate any given quantum system. This should at least theoretically provide us with an exponential speed-up and make such simulations routinely tractable.

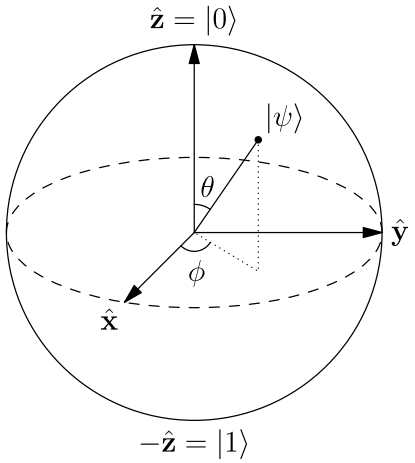

Figure 1.1: Bloch sphere representation of a single qubit [2].

The central concept is the one of a *qubit*. In contrast to the classical bit, which can be either in a state 0 or 1, qubit is a two-level quantum system (always equivalent to spin 1/2), which can be in any superposition $|\psi\rangle$ therefore in general (leaving out normalization) $|\psi\rangle = a\,|0\rangle + b\,|1\rangle\,, a, b \in \mathbb{C}$. The standard way to depict a single-qubit state is using the Bloch

sphere representation, see Fig. 1.1. In this representation angles are given as following $a = \cos\left(\frac{\theta}{2}\right)$, $b = e^{i\phi}\sin\left(\frac{\theta}{2}\right)$ (a can be chosen real due to the normalization). So in this representation, states allowed by classical bit are only the north and south pole of the Bloch sphere.

Furthermore, we need that our qubit can be operated and manipulated in a reliable way. We now list basic properties necessary for a "good" qubit [3]. Firstly, qubit must be reasonably decoupled from its environment, living long enough to perform desired computation. Secondly, we need a reliable way of initialization of the qubit into the given state. Thirdly, we need to manipulate it in order to access any state on a Bloch sphere and we need to implement coupling to other qubit. Finally, we need to read out the quantum state. We will explain this properties in greater detail later for a specific example of the spin qubit. Naturally, as we typically need rather big number of qubits to implement any specific task, we need that quantum computer is designed in a scalable way. For that reason, we need a single design in which we can essentially fabricate a device with (reasonably) any number of qubits.

The following natural question arises: Which of the two level systems are good candidates for qubits? Here we would like to give a brief overview of qubit platforms currently pursued in research. First group of devices fits into the class of superconducting qubits [4]. Their common feature is using Josephson junctions (JJs) as a key building block of the qubit. Currently their main advantage lies in the fact that systems of 50 qubits can be already fabricated, what has a fundamental importance for testing of theoretical proposals of quantum protocols on real systems. Main challenge for this class of devices seems to currently be the scalability, giving practically no hope for devices of around $10^8 - 10^9$ qubits with current designs, as well as reliable fabrication of exactly identical qubits necessary for reliable operation of scalable qubit network.

Second group of proposals is based on ions trapped in optical lattices [5]. Their main advantage is preparation of identical qubits, as well as extremely good isolation from enviroment. Therefore, their main disadvantage lies in slow operation times demonstrating usual trade-off between isolation from environment and operation times. Most stable qubits in these systems are typically based on hyperfine levels of electron/nuclear spins. For current architectures we also cannot expect scalability beyond 10^3 qubits.

Finally, third group of devices is based on spin qubits in solid state quantum dots [6], which stemmed out of seminal paper [7]. Quantum dot can be simply imagined as an artificial atom, featuring discrete en-

ergy levels caused by spatial confinement in a potential trap. By tuning the confinement and fields in the sample we can reach regimes with various fillings by electrons and holes, which can be used to define multiple types of qubits. We will discuss QDs in the greater detail later in the following sections. Their main advantage lies in fast operation and control of the qubit by external fields as well as in a reasonable hope for scalability. Realistic proposal for CMOS on-chip network of 480 qubits [8] is already available. The main challenge remains to be decoherence from the surrounding environment.

We would also like to briefly explain in which sense can be quantum computer "better" than classical one. Apart from simulation of quantum systems various problems have been shown to have lower complexity when solved by quantum computer. Pivotal among them was an integer factorization algorithm by Shor [9]. Theoretically this allows one to solve instead of a problem with sub-exponential complexity on classical computer one with polynomial complexity on quantum computer. As currently broadly used RSA cryptosystem is based on the complexity of this specific problem, this result boosted a tremendous interest in the field of quantum algorithms. Other prominent example is an algorithm by Grover [10], which provides quadratic speed-up for a database search problem. Search for different quantum algorithms expanded into a field by itself [11]. To sum up, quantum computer is not automatically supreme to classical one in all tasks. But, for a specific class of problems which are of general interest, it provides us with as much as exponential speedup.

1.2 Low dimensional quantum systems: 2DEGs and NWs

One of the goals in theoretical physics is to describe the complexity of our reality by the simplest model which explains our observations. In the condensed matter systems we have the luxury at our disposal: we can *design* systems which are easier to describe and at the same time useful for practical applications. With an advance of fabrication techniques and nanoscience of semiconductors, it became possible to obtain systems behaving as their lower-dimensional model counterparts.

First result of this process are 2DEGs [12]. From many of examples we will focus on ones which will be used further to create quantum

dots within them and which we describe theoretically in our work. With an advance of the semiconductor technology 2DEG platforms based on Si/SiO_2 metal-oxide-semiconductor (MOS) [13] were among the first broadly used devices. On Fig. 1.2 we present an example of such structure. It consists of a sandwich of p-doped Si covered by insulating SiO_2 with metallic gate on top. Once we apply V_G we create a depletion layer under the oxide. As V_G reaches a specific treshold thin inversion layer of the negative charge carriers is created directly under the oxide. This is the result of a well-known band-bending by the applied gate voltage in semiconductors.

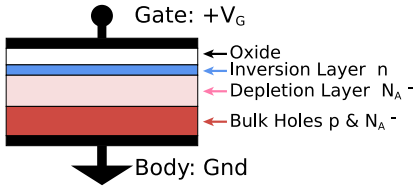

Figure 1.2: Example of a MOS structure [14].

The other frequently used platform for 2DEG is based on heterojunctions of two semiconductors with different band gaps, therefore creating also the desired band-bending. As a typical example we can take $GaAs/Al_xGa_{1-x}As$ heterostructure [15], where the band gap difference is tunable by the concentration of Al atoms, see Fig. 1.3.

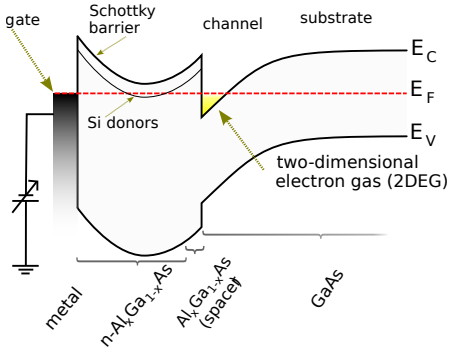

Figure 1.3: Example of a heterojunction used for 2DEG fabrication [16].

In the last 30 years fabrication of nanostructures reached another milestone by reliable growth of semiconducting quasi-1d NWs [17], and more recently of core/shell NWs [18]. As both aforementioned cases 2DEGs and NWs can be used to fabricate quantum dots as well as in case of

NWs used to engineer topological states in topological superconductors, we turn now our attention towards a suitable theoretical description of electron states in semiconductors.

Method of our interest is $\mathbf{k}\cdot\mathbf{p}$ theory [19] as it can successfully explain relevant spin-orbit interaction (SOI) phenomena. Our goal is to obtain an effective Hamiltonian for both cases of interest (valence band and conduction band). So we start from the Hamiltonian of free electrons in a crystal lattice potential $V_0(\mathbf{r})$. In the empty lattice Hamiltonian and its Bloch solution are given by

$$H^{emp} = \frac{\hat{\mathbf{p}}^2}{2m_0} + V_0(\mathbf{r}), \quad \psi_{n\mathbf{k}}(\mathbf{r}) = u_{n\mathbf{k}}(\mathbf{r})e^{i\mathbf{k}\cdot\mathbf{r}}, \quad u_{n\mathbf{k}}(\mathbf{r}+\mathbf{R}) = u_{n\mathbf{k}}(\mathbf{r}), \tag{1.1}$$

where $\mathbf{R}$ is an arbitrary lattice vector. Momentum operator acts on the Bloch states as

$$\hat{\mathbf{p}}\psi_{n\mathbf{k}}(\mathbf{r}) = (\tilde{\mathbf{p}} + \hbar\mathbf{k})\psi_{n\mathbf{k}}(\mathbf{r}), \tag{1.2}$$

where now $\tilde{\mathbf{p}}$ acts on the crystal periodic part $u_{n\mathbf{k}}(\mathbf{r})$ only. We would like to to obtain the perturbation theory close to the point $\mathbf{k} = 0$ therefore using the notation from before $\hat{\mathbf{p}}^2 \to \tilde{\mathbf{p}}^2 + 2\mathbf{k}\cdot\tilde{\mathbf{p}} + \mathbf{k}^2$ and then close to $\mathbf{k} = 0$

$$H^{emp} = H_0 + H_{\mathbf{k}\cdot\tilde{\mathbf{p}}}, \quad H_0 = \frac{\tilde{\mathbf{p}}^2}{2m_0} + \frac{\hbar^2k^2}{2m_0} + V_0(\mathbf{r}), \quad H_{\mathbf{k}\cdot\tilde{\mathbf{p}}} = \frac{\hbar}{m_0}\mathbf{k}\cdot\tilde{\mathbf{p}}. \tag{1.3}$$

Theoretically, one should include all the bands labeled by n. In practice, one usually includes the set of bands closest to the conduction band minimum/valence band maximum at a given point $\mathbf{k}_0$. In our case, we focus on the case $\mathbf{k}_0 = 0$ (Γ point) relevant in GaAs or valence band Si. One can thus expand the lattice-periodic part of the wave function as $|\nu\mathbf{k}\rangle = \sum_{n,\sigma} c_{\nu n\sigma}(\mathbf{k})\,|n\sigma\rangle$ in terms of band-edge wave function $|n\sigma\rangle = |n\sigma, \mathbf{k} = 0\rangle$ with energies $E_n(0)$. Then, at the moment without spin-orbit interaction one gets

$$\sum_{n',\sigma'}\left(\left(E_{n'}(\mathbf{0}) + \frac{\hbar^2k^2}{2m_0}\right)\delta_{nn'}\delta_{\sigma\sigma'} + \frac{\hbar}{m_0}\mathbf{k}\cdot\mathbf{P}_{nn'\sigma\sigma'}\right)c_{\nu n'\sigma'}(\mathbf{k}) = E_\nu(\mathbf{k})\,c_{\nu n\sigma}(\mathbf{k}), \tag{1.4}$$

$$\mathbf{P}_{nn'\sigma\sigma'} = \langle n\sigma|\,\tilde{\mathbf{p}}\,|n'\sigma'\rangle. \tag{1.5}$$

Now one chooses a reasonable subset of states and treats $\mathbf{k}\cdot\mathbf{p}$ as a perturbation. In our case as we are also interested in SOI effects, we have to substitute $\tilde{\mathbf{p}}$ by $\boldsymbol{\pi} = \tilde{\mathbf{p}} + \frac{\hbar}{4m_0c^2}\boldsymbol{\sigma}\times\nabla V_0$, where $\boldsymbol{\sigma}$ is a vector of Pauli

matrices. One also gets the additional term on LHS of Eq. 1.4 $\mathbf{\Delta}_{nn'\sigma\sigma'} = \frac{\hbar}{4m_0^2c^2}\langle n\sigma|\,\tilde{\mathbf{p}}\cdot\boldsymbol{\sigma}\times(\nabla V_0)\,|n'\sigma'\rangle$. Here we can already see that this term will influence splittings at $\mathbf{k}=0$ and give rise to the split-off band. The same procedure applies when one wants to include external fields into the calculation. In that case one substitutes $\hbar\mathbf{k}\to(-i\hbar\nabla+e\mathbf{A})$, where $\mathbf{A}$ is the gauge field corresponding to external magnetic field and adds Zeeman coupling and potential corresponding to external electric field $V(\mathbf{r})$ in each band n. In this scenario is $\mathbf{k}\cdot\mathbf{p}$ theory usually called as envelope function approximation (EFA), since fields act only on the crystal periodic part, which is well-justified if applied fields change on a scale much bigger than lattice spacing.

Another crucial step in the development of $\mathbf{k}\cdot\mathbf{p}$ theory is to exploit symmetries of the underlying lattice potential V_0. Semiconductors of our interest $\mathrm{Si}, \mathrm{GaAs}$ are known to have point groups O_h and T_d respectively. T_d is symmetry group of the tetrahedron and O_h symmetry group of the cube which includes all the elements of T_d plus full spatial inversion and its combinations with all other elements of T_d. Therefore T_d has 24 elements and O_h has 48 elements.

Now we recall the well-known scenario of symmetries in quantum mechanics. If our system is symmetric under an action of a finite group G then for the Hamiltonian $\mathcal{H}$ of our system it means $D_\alpha(G)^{-1}\mathcal{H}D_\alpha(G)=\mathcal{H}$, where $D_\alpha(G)$ is a matrix from the representation of G labeled by integer α. For each crystallographic group, one has at hand tables of its elements, characters and representations see for example [20].

One continues as follows: chooses the number of bands included in the calculation, for each band obtains to which representation of the underlying point group it belongs (from spectral data or density functional theory), and based on these assumptions construct the resulting Hamiltonian. This approach was pioneered by Kane [21] and systematically formulated by Bir, Pikus [22]. These models need experimental inputs in order to determinate free parameters which can not be obtained from any symmetry argument.

As an example we will now discuss one case relevant for our work, what is EFA for conduction band of GaAs in external magnetic field. So starting point is the band structure of GaAs labeled by respective representations, see Fig. 1.4. Furthermore, we follow analysis of this case presented by Braun, Rössler [23].

We begin by writing the most general Hamiltonian invariant under the T_d group and time-reversal symmetry. In our case, including ex-

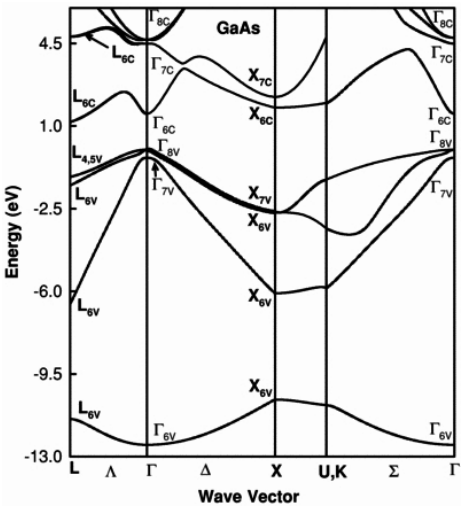

Figure 1.4: Band structure of GaAs [24].

ternal magnetic field, one has three ingredients to "cook" the Hamiltonian namely three vectors $\mathbf{k}, \mathbf{B}$,$\boldsymbol{\sigma}$ (and identity in the spin-space). Time-reversal symmetry acts as following : $\mathbf{k}, \mathbf{B}, \boldsymbol{\sigma} \rightarrow -\mathbf{k}, -\mathbf{B}, -\boldsymbol{\sigma}$, so only terms invariant under this transformation are allowed. Resulting Hamiltonian is 2×2 due to spin, therefore it can be decomposed into basis matrices $\boldsymbol{\sigma}, \mathbb{I}$ and functions of $\mathbf{k}, \mathbf{B}$. Both matrices and functions can be characterized by the representation of T_d to which they belong and the only way to obtain a scalar under any action of the group is to combine matrices and functions belonging to the same representation (this is based on Wigner-Eckart theorem). Following this procedure one obtains the resulting invariant Hamiltonain up to the given order in $\mathbf{k}, \mathbf{B}$. Up to the fourth order in $\mathbf{k}$ (we recall $[k_i, k_j] \sim \epsilon_{ijk} B_k$ thus B_i counts as being second order in $\mathbf{k}$, $\{\}$ stands for anticommutator):

$$
\begin{aligned}
&H_{CB} = H_1 + H_4, \quad H_1 = \mathbb{I}\left(c_{11} + c_{12}k^2 + c_{13}k^4 + c_{14}\left(\{k_x k_y\}^2 + \right.\right. \\
&\left.\left.\{k_y k_z\}^2 + \{k_z k_x\}^2\right) + c_{15}B^2\right), \quad H_4 = c_{41}\mathbf{B}\cdot\boldsymbol{\sigma} + c_{42}k^2\mathbf{B}\cdot\boldsymbol{\sigma} + \\
&c_{43}\left(k_x^2 B_x\sigma_x + k_y^2 B_y\sigma_y + k_z^2 B_z\sigma_z\right) + \\
&c_{44}\left(\left\{\left(k_y^2 - k_z^2\right)k_x\right\}\sigma_x + \left\{\left(k_z^2 - k_x^2\right)k_y\right\}\sigma_y + \left\{\left(k_x^2 - k_y^2\right)k_z\right\}\sigma_z\right) + \\
&c_{45}\left(\left(\{k_x k_y\}B_y + \{k_x k_z\}B_z\right)\sigma_x + \left(\{k_y k_z\}B_z + \{k_y k_x\}B_x\right)\sigma_y + \right. \\
&\left.\left(\{k_z k_x\}B_x + \{k_z k_y\}B_y\right)\sigma_z\right).
\end{aligned} \tag{1.6}
$$

We can immediately distinguish many familiar terms, for example c_{44} term corresponds to Dresselhaus spin-orbit term in inversion-asymmetric

semiconductor (such term is prohibited in cubic semiconductors like Si, as it changes sign under spatial inversion). In the second step, Kane's 14×14 model is taken and fourth-order Löwdin partitioning is used to decouple the 2×2 subspace of conduction band from the other bands. Resulting Hamiltonian is then compared with Eq. 1.6 and all the constants are obtained in terms of band-structure parameters. This provides us with the compact description of spin states in conduction band of GaAs.

Depending on the context, the same method can be used to obtain effective Hamiltonians in other materials and also up to the order neccessary to describe desired effects. In practice, people usually include terms up to the second order in $\mathbf{k}$ (effective mass approximation, where bare mass m_0 is renormalized by $\mathbf{k} \cdot \mathbf{p}$ interaction), and lowest-order SOI terms, whats means Dresselhaus SOI in inversion-asymmetric materials and Rashba SOI resulting from inclusion of also electric field as an external field. By the same symmetry analysis, one can also include additional terms coming from strain within the sample, especially at the interfaces of MOS strutures, which are not lattice matched in contrast to $\mathrm{GaAs/Al_xGa_{1-x}As}$ heterostructures.

As can be seen from the presented band structure of GaAs, physics of holes around valence band maximum at $\mathbf{k} = 0$ is expected to be much richer due to the degenerate heavy hole, light hole valence band providing therefore 4×4 subspace and proximity of SOI split-off band. This gap is particularly small in Si providing thus a rich playground for the field of spin qubits.

1.3 Quantum dots and spin qubits

Since the seminal paper [7] it is well-understood how quantum dots can be used as a building block of the quantum computer. It was shown that within a simple scenario of two coupled quantum dots one can perform all single-qubit gates and a two-qubit entangling gate, which is known to be a complete set of gates necessary to perform any quantum computation [25]. Typically, this sets consists of three single-qubit gates and one two-qubit entangling gate. For the set of single-qubit gates there are many choices, important point is to reach any point on a Bloch sphere by composition of such gates. For two-qubit gates, typical choice is a CNOT-gate or $\sqrt{\mathrm{SWAP}}$ gate.

In the following we will focus on one specific type of quantum dots fabricated by confining carriers in 2DEGs by metallic gates, so-called lat-

eral quantum dots [26]. On the Fig. 1.5 we can see a typical example of such structure fabricated in GaAs 2DEG sample.

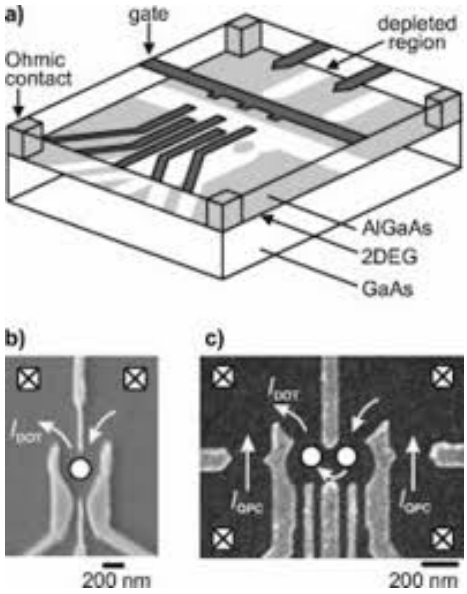

Figure 1.5: Scheme of a typical lateral double quantum dot in GaAs [26] In a) we see a generic scheme of such device and in b) and c) real samples of fabricated single- and double-quantum dots respectively. In c) we also see quantum point contacts (QPCs) which can be used to measure charge occupation within the neigbouring dots.

From there, we can see that we have a great amount of control over the sample by tuning the various gates fabricated within the sample. We can tune depletion in each single dot, shape of the dot as well as inter-dot tuneling. Moreoever, we can use QPCs to detect charge occupation within the neighbouring dots. In practice, this amount of tunability can be also problematic as it can be time-intensive to reach a desired regime. Recently, great progress was done in order to use computer algorithms to tune the sample into a desired regime [27]. With current lithography one can get quantum dots of this kind with diameter ~ 100nm [6].

In order to theoretically describe electron states in these structures, one has to include potentials created by gates into the calculations. Remarkably, in most cases one gets satisfactory results by treating confinement creating the dot as a parabolic potential in case of single QDs and as bi-parabolic in case of double QDs. In these cases, one can employ exact analytical solutions. If one aims at more precise treatment of surround-

ing gate potentials, self-consistent solving of Schrödinger and Poisson equations is necessary [28].

As an example we provide one of the effective Hamiltonians used extensively in the literature for a single quantum dot

$$H_{QD} = H_0 + H_Z + H_{\mathrm{SOI}} \tag{1.7}$$

with

$$H_0 = \frac{p_x^2 + p_y^2}{2m^*} + \frac{m^*\omega^2}{2}\left(x^2 + y^2\right), \tag{1.8}$$

$$H_Z = \frac{g\mu_B}{2}\boldsymbol{B}\cdot\boldsymbol{\sigma}, \tag{1.9}$$

$$H_{\mathrm{SOI}} = \alpha\left(p_x\sigma_y - p_y\sigma_x\right) + \beta\left(p_x\sigma_x - p_y\sigma_y\right). \tag{1.10}$$

In this case, H_0 represents an effective-mass approximation for carriers in the semiconductor 2DEGs grown along $[001]$ direction, H_Z is a Zeeman term with material-dependent g-factor and H_{SOI} represents Rashba and Dresselhaus SOI (higher-order terms and other forms can be found in the literature depending on the 2DEG growth-direction and material).

At this moment, we can introduce the notion of a spin qubit. We can think about a QD modeled as a parabolic potential and fill it by a single electron (hole). Zeeman-split spin state of this electron (hole) with known orbital state can be now used as a qubit. To characterize any realistic qubit we have to introduce a few important timescales.

Usually for any qubit one defines $|0\rangle$ as a ground state of the qubit and $|1\rangle$ as an excited state of the qubit. In an ideal case of a qubit separated from the environment state $|1\rangle$ has an infinite lifetime since it is an eigenstate. In a real system, qubit is weakly coupled to multiple external fluctuations, namely nuclear spins, phonons, gate voltage fluctuations and can also interact via SOI. Due to this fact excited state has always only a finite life-time. This timescale is usually called T_1 in the literature and referred to as relaxation time. As we can see this timescale provides us an absolute upper-limit in the "memory" sense, since one cannot store any quantum information for a scale longer than T_1.

In general, one processes and stores quantum information in superpositions. Therefore, another relevant time scale is the decay of state $\frac{1}{\sqrt{2}}\left(|0\rangle + |1\rangle\right)$ into state $|0\rangle$ called usually decoherence time T_2. Since many of the fluctuation sources behave as random white-noise, one needs to also average over an ensemble of spin qubits in order to obtain a descriptive timescale. This is usually referred to as dephasing time T_2^*. As

expected, for spin qubits we typically get $T_1 > T_2 > T_2^*$. On the Fig. 1.6 we provide an extensive review of these timescales from the current literature on solid state spin qubits.

Qubit type	T1[ns]	T2[ns]	T2*[ns]
GaAs spin ½	10^9 [1]	300 [2]	61 [3]
GaAs ST	2.1*10^6 [4]	8.7*10^5 [5]	2*10^3 [6]
GaAs exchange	10^5 [7]	100 [7]	25 [7]
Self assembl InGaAs electron	2*10^7 [8]	3*10^3 [9]	2 [9]
Self assembl InGaAs 2electron			200 [10]
Self assembl InGaAs hole	10^6 [11]	10^3 [12]	460 [12]
Nat SiGe spin ½	3*10^9 [13]	3.7*10^4 [14]	920 [14]
Nat Si spin ½	10^9 [15]	50*10^3 [16]	10^3 [16]
Purif Si spin ½		2.8*10^7 [17]	1.2*10^5 [17]
e in P donor in nat Si	7*10^8 [18]	2*10^5 [18]	55 [18]
P donor nuclear spin in nat Si	65*10^10 [19]	6*10^7 [19]	3.3*10^6 [19]
e in P donor in pur Si		9.5*10^7 [20]	2.7*10^5 [20]
P donor nuclear spin in pur Si		1.8*10^9 [20]	6*10^8 [20]
NV Center	10^6 [21]	1.8*10^6 [22]	2.7*10^3 [23]
Nuc spin close to NV	6*10^6 [24]	0.4*10^6 [24]	
Si vacancy in diamond	2.4*10^6 [25]		45 [25]

[1] Gossard PRL 100, 046803 (2008), [2] Vandersypen PRL 100, 236802 (2008), [3] Tarucha PRL 113, 267601 (2014), [4] Hanson PRL 94, 196802 (2005), [5] Marcus Nat. Nanotechnology 12, 16 (2017) , [6] Yacoby Nat. Com. 5, 5156 (2014), [7] Marcus Nat. Nanotechnology 8, 654 (2013), [8] Finley Nature 432, 81 (2004), [9] Bayer Science 313, 341 (2006), [10] Imamoğlu PRL 109, 107401 (2012), [11] Warburton Nature 451, 441 (2008), [12] Warburton Nat. Materials 15, 981 (2016), [13] Eriksson PRL 106, 156804 (2011), [14] Vandersypen Nat. Nanotechnology 9, 666 (2014), [15] Dzurak Nat. Com. 4, 2069 (2013), [16] Vandersypen PNAS 113, 42, 11738 (2016), [17] Dzurak Nature 526, 410 (2015) , [18] Morello Nature 489, 541 (2012), [19] Morello Nature 496, 334 (2013), [20] Morello Nat. Nanotechnology 9, 986 (2014), [21] Hanson Science 330, 6000, 60 (2010), [22] Wrachtrup Nat. Materials 8, 383 (2009), [23] Corry PRL 105, 200402 (2010), [24] Meriles Nature Communications 4, 1651 (2013), [25] Jelezko PRL 113, 263602 (2014)

Figure 1.6: Overview of qubit time scales for current solid state spin qubit platforms under investigation.

One can appreciate the tremendous progress which happened in this field in the recent decade and broad range of systems studied for this purpose, among them various types of qubits (single spin, singlet-triplet, exchange), various hosting materials and also harnessing the nuclear spins to define the qubit. In the following we will focus exclusively on lateral QDs, but from this example one can see well how extensive current research on this topic is.

At this point, we can also comment why most of the experimental interest is recently shifting towards Si platforms [29] for lateral QDs. In GaAs one has to inevitably face the issue of decoherence by nuclear spins within the sample as both isotopes in natural Ga have nuclear spin $3/2$.

On the other hand, natural Si is composed of 92% from nuclear spin-free isotope. By further isotopal enriching of the sample material one can reach $T_2^* = 1.2 \times 10^5$ns [30] what is two orders of magnitude longer than for any qubit in GaAs.

Last topic to address in this section is spin qubit operation and respective timescales. We will discuss the two most broadly used types of qubits, single spin qubits and singlet-triplet (ST) qubit. For the single spin qubit states are split by magnetic field (both from an Overhauser field coming from within the sample due to nuclear spins and due to external magnetic field B_Z).

So we can identify the qubit states as $|0\rangle = |\uparrow\rangle, |1\rangle = |\downarrow\rangle$. One axis on the Bloch can be realized by coherent rotations $\frac{1}{\sqrt{2}}(|\uparrow\rangle + |\downarrow\rangle) \rightarrow \frac{1}{\sqrt{2}}(|\uparrow\rangle - |\downarrow\rangle)$. These transitions are very fast on the order of $\frac{\hbar}{2g\mu_B B_Z}$, times reported for GaAs are in sub-nanoseconds scale governed by effective g-factor, therefore not also problematic in Si.

Second axis corresponds to the transitions $|\uparrow\rangle \rightarrow |\downarrow\rangle$ driven by electric-dipole-induced spin resonance (EDSR). Due to the SOI, applied oscillating electric field $\mathbf{E}(t)$ leads to the induced oscillating magnetic field $\mathbf{B}_{IND}$, in general with components perpendicular to applied static magnetic field B_Z. This can then drive the desired transition on the timescale of ~ 10ns in GaAs. Due to weaker SOI this remains challenging in Si and can be resolved by switching to hole based devices, which provide richer SOI physics.

Two-qubit SWAP corresponding to $|\uparrow\downarrow\rangle \rightarrow |\downarrow\uparrow\rangle$ can be realized by controlling the overlap of electrons in the neighbouring dots by gates. Times on sub-nanosecond scales were obtained, not imposing thus any severe limits on operations of such qubits. Initialization and read-out of this qubit can be performed via spin-to-charge conversion. In this scenario, dot is electrically tuned into a regime where the residing electron does or does not tunnel out of the dot depending on its state. Single-shot readout of such tunneling events is performed through the QPC near the dot as shown on Fig. 1.5c).

Other broadly used qubit is based on the two-electron states in the double QD. One takes $|0\rangle = |S\rangle = \frac{1}{\sqrt{2}}(|\uparrow\downarrow\rangle - |\downarrow\uparrow\rangle)$ and $|1\rangle = |T_0\rangle = \frac{1}{\sqrt{2}}(|\uparrow\downarrow\rangle + |\downarrow\uparrow\rangle)$. Transitions $|0\rangle \rightarrow |1\rangle$ can be achieved by magnetic field gradient within the QD from a nearby micromagnet on sub-nanosecond scale. Other axis given by transitions $\frac{1}{\sqrt{2}}(|0\rangle + |1\rangle) \rightarrow \frac{1}{\sqrt{2}}(|0\rangle - |1\rangle)$ can be implemented by tuning the tuneling within the double QD by gates, controlling thus the overlap of the electron states. This manipulation can

be also achieved on sub-nanosecond scale. Finally, entangling CPHASE gate was demonstrated in four dot devices by capacitive coupling between the different charge states in respective double QDs on the scale of 30ns.

For initialization DQD is gated into the detuned regime given by the occupation $(2, 0)$, where one of the dots has a substantially lower energy, therefore once the second electron tunnels in, it creates a singlet state with both electrons in the orbital ground state. Same principle is used after operation in $(1, 1)$ regime to perfrom the readout via spin-to-charge conversion as in the triplet state second electron can not tunnel into the detuned dot due to the Pauli exclusion principle.

As we can see from the presented overview, spin qubits are practically limited by the timescales corresponding to various sources of noise due to to nuclear spins, SOI, phonons and fluctuating fields necessary for their operation. In order to overcome these limitations completely, we have to think about other platforms for quantum computation.

1.4 Topological superconductors and Majorana Fermions

Topology is mostly known as a field of mathematics studying invariant properties of spaces under any continuous deformation. This can be used in physics [31] as following: we have a Hamiltonian of our system, which depends on the set of parameters and for each set of parameters we can obtain its solutions. Can solutions for arbitrary parameters be always continuously deformed into each other (having the same "topology") or are there multiple so-called "topological phases" which cannot be continuously deformed into each other, being as a result separated by "topological phase transition"?

First example of such system was found to be the quantum Hall effect [32]. Approach taken is very similar to the one in topology. In order to prove that two phases are not topologically equivalent one has to find an integer topological invariant, which has a different value in respective phases. We will now present an elementary example of such topological invariant and we begin by introducing the Berry phase and the Berry connection.

We recall a generic Bloch Hamiltonian for a band insulator $H(\mathbf{k})\,|u_n(\mathbf{k})\rangle = E_n(\mathbf{k})\,|u_n(\mathbf{k})\rangle$. Here $\mathbf{k}$ serves as parameter of the Hamiltonian. One

then defines Berry connection as following (note the similarity with gauge field)

$$\mathcal{A}_j^n(\mathbf{k}) = i \langle u_n(\mathbf{k})| \partial_{k_j} |u_n(\mathbf{k})\rangle . \tag{1.11}$$

Intuitively, Berry connection measures change of the wave function along an infinitesimal step in the k-space. Due to the phase freedom in the wave function this quantity is not gauge invariant with respect to the change of the phase of the wave function. In order to obtain gauge invariant quantity we proceed in the same way as is known from electromagnetism and we define field strength tensor as

$$\mathcal{F}_{ij}^n(\mathbf{k}) = \partial_{k_i}\mathcal{A}_j^n(\mathbf{k}) - \partial_{k_j}\mathcal{A}_i^n(\mathbf{k}). \tag{1.12}$$

In this language one can now easily rephrase the original TKNN integer [32]. Firstly, we introduce the Chern number for n-th band of a 2d system, where BZ denotes the Brioullines zone, ∂R is a boundary of a region R including possible singularity in $\mathcal{A}_j^n(\mathbf{k})$ at $\mathbf{k}_0$, $\phi_n(\mathbf{k})$ is the phase factor following from "gauge" freedom $|u_n(\mathbf{k})\rangle \rightarrow e^{i\phi_n(\mathbf{k})} |u_n(\mathbf{k})\rangle$ which is used in order to get rid of a singularity in the region R and by using Stokes theorem (if there is no singularity in $\mathcal{A}_j^n(\mathbf{k})$ we get trivially zero)

$$Ch^n = \frac{1}{2\pi}\int_{BZ} \mathrm{d}k_x \mathrm{d}k_y \mathcal{F}_{xy}^n(\mathbf{k}) = \frac{1}{2\pi}\int_{\partial R} \mathrm{d}\mathbf{k}\cdot\partial_{\mathbf{k}}\phi_n(\mathbf{k}). \tag{1.13}$$

Because $e^{i\phi_n(\mathbf{k})}$ is a unique function on ∂R, Ch^n must have integer value. One then defines total Chern number as a sum through the occupied states $Ch = \sum_{E_n<E_F} Ch^n$ and this can be connected to Hall conductance as $\sigma_{xy} = -\frac{e^2}{h}Ch$. Now we can already obtain non-trivial result considering time-reversal symmetry in the system. As can be seen from Eqs. 1.11, 1.12 $\mathcal{F}_{ij}^n(\mathbf{k})$ is odd under time-reversal therefore one obtains that under time-reversal $Ch \rightarrow -Ch$. So we show that Hall conductance is trivially zero in time-reversal invariant system and non-zero when time-reversal symmetry is broken by magnetic field. We stress that this analysis was performed for spinless case, thus it does not imply anything for quantum spin Hall effect.

From this example we can see that in order to get topologically non-trivial phases of matter one has to analyze possible topological invariants of a generic given Hamiltonian considering its dimensionality and symmetries. This is a starting point for multiple classification schemes of topological phases [33,34].

In case of topological superconductors, one has to include particle-hole symmetry essential for the description of superconductors. We start by considering generic spinless 1d Hamiltonian

$$\mathcal{H} = \frac{1}{2}\sum_k \left(c_k^\dagger, c_{-k}\right) \mathcal{H}'(k) \begin{pmatrix} c_k \\ c_{-k}^\dagger \end{pmatrix} \quad \mathcal{H}'(k) = \begin{pmatrix} \varepsilon(k) & d(k) \\ d^*(-k) & -\varepsilon(-k) \end{pmatrix}. \quad (1.14)$$

This Hamiltonian can be diagonalized obtaining $E(k) = \sqrt{\varepsilon^2(k) + |d(k)|^2}$ and then recast into the following form, where $\boldsymbol{\tau}$ denotes the vector of Pauli matrices

$$\mathcal{H}(k) = E(k)\,\mathbf{x}(k)\cdot\boldsymbol{\tau}, \quad x_1(k) = \frac{\mathrm{Re}\, d(k)}{E(k)}, \quad (1.15)$$

$$x_2(k) = -\frac{\mathrm{Im}\, d(k)}{E(k)}, \quad x_3(k) = \frac{\varepsilon(k)}{E(k)}. \quad (1.16)$$

It follows that $\mathbf{x}^2(k) = 1$, therefore $\mathbf{x}(k)$ lives on the 2d sphere S^2 and maps the Brillouines zone onto a circle on the sphere. Particle-hole symmetry provides constraint $d(k) = -d(-k)$ and thus $d(k) = 0$ at $k = 0, \pi$. This has interesting consequences since then $x_3(0) = x_3(\pi)$ or $x_3(0) = -x_3(\pi)$. In the first case, one gets an image which passes the same pole of the sphere and can be thus shrunk to a point, in the latter case one gets an image which passes through different poles and is then not contractible to a point. So as we see, one obtains two topologically distinct phases based on the sign on the product $\varepsilon(0)\varepsilon(k)$.

We will now discuss Kitaevs toy model Hamiltonian [35] of a 1d spinless p-wave superconductor, which features topological phase transition. Model is given by the following Hamiltonian

$$H = -t\sum_{i=1}^{N-1}\left(c_i^\dagger c_{i+1} + \mathrm{h.c.}\right) - \mu\sum_{i=1}^{N}\left(c_i^\dagger c_i - \frac{1}{2}\right) - \Delta\sum_{i=1}^{N-1}\left(c_i c_{i+1} + \mathrm{h.c.}\right), \quad (1.17)$$

where Δ, t, μ are real and N is even. This model is in the topological phase when $2|t| > |\mu|, \Delta \neq 0$ and in the trivial phase in the opposite regime. This can be seen from the same argument as shown before.

Another interesting feature of the topological phases is the so-called bulk-boundary correspondence. It roughly means that the singularity coming from the structure of the bulk states is canceled by the presence of modes localized at the boundaries of the system where the topologically

non-trivial system is interfaced with the topologically trivial system (vacuum), thus resolving the mismatch in topologies. This can be also seen in the Kitaev model. In the first step one considers splitting the complex operators into real and imaginary part as following $c_i = \frac{1}{2}(\gamma_{i,1} + i\gamma_{i,2})$, therefore to each physical site we get two operators to represent its states. If one for simplicity considers now regime $\mu = 0, t = -\Delta > 0$ and introduces following operators $\tilde{c}_i = \frac{1}{2}(\gamma_{i+1,1} + i\gamma_{i,2})$, Hamiltonian Eq. 1.17 reduces to $H = 2t\sum_{i=1}^{N-1} \tilde{c}_i^\dagger \tilde{c}_i$. Both trivial and topological phases are depicted on Fig. 1.7

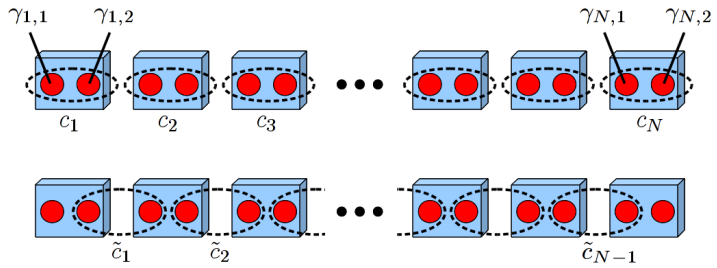

Figure 1.7: Pictorial representation of Kitaev model in the trivial phase (upper figure) and in the topological phase (lower figure) [36]. In the trivial phase operators defined at the same lattice sites are paired. In the topological phase operators across sites are paired leaving first and last γ operators unpaired.

We obtained the sum of $N-1$ mutually commuting terms, thus the ground state is given by $\tilde{c}_i^\dagger \tilde{c}_i = -1$. But in that case $\gamma_{1,1}$ and $\gamma_{N,2}$ do not appear in the Hamiltonian, so it follows that $[H, \gamma_{1,1}] = [H, \gamma_{N,2}] = 0$. This means that we obtained a twofold-degenerate ground state labeled by $i\gamma_{1,1}\gamma_{N,2} = \pm 1$ and that both modes have zero energy. These states are localized at the boundary of the system providing us therefore with an example of bulk-boundary correspondence in this specific model. In order to further understand the properties of obtained states we introduce now the notion of Majorana fermion.

Majorana fermion has been proposed by E. Majorana [37] in the context of quantum field theory as the real field solution of the Dirac equation $i\hbar\gamma_\mu\partial_\mu\psi - mc\psi = 0$. Then it follows that $\psi = \psi^\dagger, m = 0$ so the solutions is massless. Ideal candidates for such states are neutrinos, but from the recent experimental data we cannot satisfactory conclude neither their massless property nor the self-conjugation [38]. One can ask

whether such state would be also possible to obtain in the condensed matter physics as a quasiparticle excitation.

Obvious systems to look at are BCS supercoductors where particle-hole symmetry occurs naturally. Here one has two choices in order to obtain a fermionic state with desired properties. One either has conventional s-wave superconducting pairing of electrons obeying Dirac equation or exotic p-wave pairing of conventional electrons with parabolic dispersion. Due to the recent successful realization of the latter class of systems, we will further focus on systems with p-wave pairing.

We have already discussed Kitaev model, where we found zero-energy states in the topological phase being ideal candidates for Majorana fermions. Problem is that such toy model is not easy to realize in the current experiments. We have to look for a more complicated realistic model showing the same properties, or having Kitaev model as an effective limit. This was resolved in the seminal paper [39].

It was shown that Majorana fermions can be obtained in systems currently at hand. Main ingredients are provided by semiconducting NW with strong Rashba SOI placed on the top of bulk s-wave superconductor in the presence of magnetic field along the NW. In [40] exact solution of such realistic model for the Majorana state in the semi-infinite wire was obtained, so we will now briefly introduce the model and discuss the results.

Aforementioned hybrid system of semiconducting NW in proximity to bulk superconductor can be modeled in the continuous limit by the following Hamiltonian

$$H = H^{\mathrm{kin}} + H^{\mathrm{SOI}} + H^{\mathrm{Z}} + H^{\mathrm{SC}}, \tag{1.18}$$

$$H^{\mathrm{kin}} = \sum_{\sigma} \int dx\ \Psi^{\dagger}_{\sigma}(x) \left[\frac{(-i\hbar\partial_x)^2}{2m} - \mu \right] \Psi_{\sigma}(x), \tag{1.19}$$

$$H^{\mathrm{SOI}} = -i\alpha_R \sum_{\sigma,\sigma'} \int dx\ \Psi^{\dagger}_{\sigma}(x)(\sigma_3)_{\sigma\sigma'}\partial_x \Psi_{\sigma'}(x), \tag{1.20}$$

$$H^{\mathrm{Z}} = \Delta_Z \sum_{\sigma,\sigma'} \int dx\ \Psi^{\dagger}_{\sigma}(x)(\sigma_1)_{\sigma\sigma'}\Psi_{\sigma'}(x), \tag{1.21}$$

$$H^{\mathrm{SC}} = \frac{1}{2} \sum_{\sigma,\sigma'} \int dx\ \Delta_{SC}(\Psi_{\sigma}(i\sigma_2)_{\sigma\sigma'}\Psi_{\sigma'} + \mathrm{h.c.}), \tag{1.22}$$

where m denotes effective mass of the carriers in the $1d$ NW, μ denotes chemical potential, α_R denotes Rashba SOI coupling constant, $\Delta_Z = g\mu_B B/2$,

where g is the g-factor and μ_B the Bohr magneton denotes Zeeman gap, σ_i are Pauli matrices and finally Δ_{SC} denotes proximity-induced superconducting gap in the NW. Solving this Hamiltonian one obtains the following 4 bands as depicted on Fig. 1.8

$$E_{\pm}^2(k) = \left(\frac{\hbar^2 k^2}{2m}\right)^2 + (\alpha_R k)^2 + \Delta_Z^2 + \Delta_{sc}^2 \pm 2\sqrt{\Delta_Z^2\Delta_{sc}^2 + \left(\frac{\hbar^2 k^2}{2m}\right)^2 (\Delta_Z^2 + (\alpha_R k)^2)}. \tag{1.23}$$

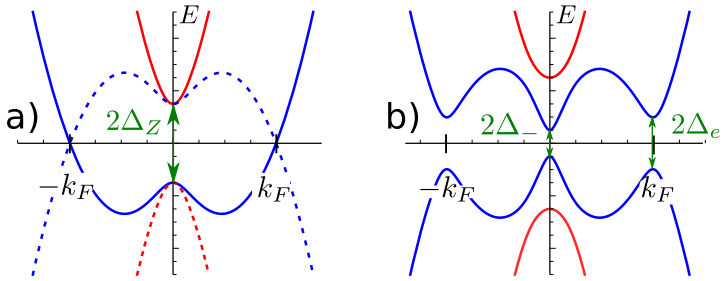

Figure 1.8: Energy dispersion of Hamiltonian Eq. 1.18. In the case a) without superconductivity and in the case b) including proximity induced superconductivity [40].

We see that Rashba SOI causes the splitting of two degenerate spins and shifts parabolas away from $k = 0$ where the Zeeman gap is opened. Once superconductivity is introduced, another so-called exterior gap opens at k_F given by $\Delta_e = 2\,|E_-(k_F)|$ and the interior gap at $k = 0$ is renormalized as $\Delta_- = \Delta_{SC} - \Delta_Z$ serving as a gap defining the topological phase transition. When $\Delta_{SC} > \Delta_Z$ system is in the trivial phase and in the regime $\Delta_{SC} < \Delta_Z$ is in the topological phase. Therefore, for a system with boundaries one expects Majorana fermions to be present and localized at the boundaries.

In the regime of strong SOI, which is also experimentally relevant for the current experiments in InSb NWs, one can also find exact solution for the Majorana fermion localized at the boundary of a semi-infinite system, solving first for zero-energy states and then imposing boundary condition on the edge. This procedure leads to the following Majorana wave function

$$\Phi_M(x) = \begin{pmatrix} i \\ 1 \\ -i \\ 1 \end{pmatrix} e^{-k_-^{(i)} x} - \begin{pmatrix} i\, e^{ik_F x} \\ e^{-ik_F x} \\ -i\, e^{-ik_F x} \\ e^{ik_F x} \end{pmatrix} e^{-k^{(e)} x}, \tag{1.24}$$

with $k_F = 2k_{so} = \frac{2m\alpha_R}{\hbar^2}$, $k^{(e)} = \frac{\Delta_{SC}}{\alpha_R}$, $k_-^{(i)} = \frac{|\Delta_{SC} - \Delta_Z|}{\alpha_R}$. From this relations we can see that Majorana mode has two localization lengths $k^{(e)}, k_-^{(i)}$. If one drives the topological phase transition by changing the magnetic field, the former scale is fixed and the latter changes depending on how deep in the topological phase one drives the system, and the deeper in the topological phase the more Majorana mode is localized.

In order to conclude this section, we would like to mention the latest results from state-of-the-art experiments in proximitized NWs and show that provided theoretical model can explain behaviour observed. First one has to ask how one can probe Majorana modes. As we have seen, they reside at zero energy therefore one can measure differential conductance in the trivial and topological phase and see if there is a zero-energy state appearing in the topological phase. Main problem here is that there are also other zero energy bound states known which are not Majoranas (like Andreev bound states). One has to then perform additional checks of how this zero-bias peak behaves with respect to parameters like temperature and external fields. Such transport simulations can be done within the framework of the presented model.

Latest results [41] performed at 20mK show, that one obtains the zero-bias peak in the topological phase reaching theoretical quantized value due to the perfect Andreev reflection $\frac{2e^2}{h}$ resolving thus a long-standing issue of observing such peaks with much lover value due to the dissipation and quasiparticle poisoning through the soft gap.

CHAPTER 2

Long-range Interaction Between Charge and Spin Qubits in Quantum Dots

Adapted from:
Marcel Serina, Christoph Kloeffel and Daniel Loss
"Long-range interaction between charge and spin qubits in quantum dots",
Phys. Rev. B **95**, 245422 (2017)

We analyze and give estimates for the long-distance coupling via floating metallic gates between different types of spin qubits in quantum dots made of different commonly used materials. In particular, we consider the hybrid, the singlet-triplet, and the spin-$1/2$ qubits, and the pairwise coupling between each type of these qubits with another hybrid qubit in GaAs, InAs, Si, and $\mathrm{Si_{0.9}Ge_{0.1}}$. We show that hybrid qubits can be capacitively coupled strongly enough to implement two-qubit gates, as long as the distance of the dots from the metallic gates is small enough. Thus, hybrid qubits are good candidates for scalable implementations of quantum computing in semiconducting nanostructures.

2.1 Introduction

One of the most promising ways to implement the concept of quantum computation [1] is to use the spins of electrons in quantum dots as qubits [7]. Quantum dots fabricated in semiconductor nanostructures are

used to confine electrons, which can then be manipulated and measured by electrical gates [42]. Many generalizations of qubits in quantum dots have been proposed and explored over the years [6,43,44]. A recent interesting addition is a proposal for a so-called hybrid qubit [45–48] formed in a double quantum dot (DQD) by different states of three electrons, where both charge and spin degrees of freedom of the electrons play a role. Since all types of spin qubits have their specific weaknesses and strengths, it is useful to ask if one can combine various types of such qubits to make optimal use of their particular advantages.

Furthermore, to successfully implement quantum computation, scalable architectures consisting of many qubits are needed. One of the possibilities to achieve such a goal is to couple the qubits in quantum dots over a long distance by using a metallic floating gate [49]. In this proposal, quantum dots could be hundreds of micrometers apart from each other, coupled in a similar way as electronic components are coupled by wires.

Here, we extend the proposal of Ref. [49] and study the long-distance coupling between the newly introduced hybrid qubit [45–48] and other types of qubits theoretically. For this, we consider two lateral DQDs [6,26,42,50,51] that are separated so far from each other that tunnel coupling is impossible. A floating metallic gate enables a capacitive coupling that depends on the positions of the DQDs with respect to the gate and that can therefore be controlled electrically. We study different host materials such as Si or GaAs, analyze the dependence of the qubit-qubit interaction on several system parameters, and find that strong interactions are achievable which can be used to implement entangling two-qubit gates with short operation times.

There are three different qubit combinations we consider. First, we study the case of two hybrid (H) qubits [45–48]. In the second case, one DQD contains two and the other DQD three electrons, i.e., one DQD hosts a singlet-triplet (ST) qubit [50, 52, 53] and the other one a hybrid qubit. In these two cases a spin-orbit interaction (SOI) is not required, since the qubit-qubit coupling can be induced solely by the Coulomb interaction and the Pauli exclusion principle. In the third case, we consider a system where one of the DQDs is singly occupied forming the spin-1/2 (LD) qubit [7,54] and the second one is triply occupied, i.e., a hybrid qubit. Each of these three cases will be studied separately. However, it is important to mention that experimentally it is possible to realize the different schemes within the very same experimental setup by only modifying the voltages on the gates.

The paper is organized as follows. First in Sec. 2.2 we focus on the H-H and H-ST qubit-qubit couplings in GaAs. Then, in Sec. 2.3 we calculate the H-LD coupling in GaAs, and in Sec. 2.4 we analyze the dependence on the setup geometry and compare all the couplings in four different semiconducting materials commonly used for the fabrication of quantum dots, namely GaAs, InAs, Si, and $\mathrm{Si}_{0.9}\mathrm{Ge}_{0.1}$. Finally, in Sec. 2.5 we summarize and give some conclusions. A detailed derivation of the electrostatic coupling via floating gates, the expansion of the electrostatic potential and details of a used Schrieffer-Wolff transformation are appended.

2.2 H-H and H-ST coupling

The DQD hybrid qubit, introduced recently in Ref. [46], operates on three different three-electron-states as illustrated in Fig. 2.1. In order to implement a universal set of quantum gates, one must be able to couple such qubits to each other pairwise [55].

The idea pursued here is to couple two such hybrid-qubits over a (possibly long) distance via a floating gate in the way proposed in Ref. [49] and to estimate the strength of the resulting coupling between them. This setup is promising due to its simplicity and scalability and provides a pathway for implementing large-scale quantum computing architectures. The coupling is mediated through the Coulomb interaction of the induced charges on the floating gate caused by the charge distributions in the qubits. As the different states of the hybrid qubit have different charge distributions (in contrast to qubits based on the spin states of a single quantum dot when SOI is absent), it is sufficient to take into account the Coulomb interaction in order to estimate the coupling. Thus, one may assume that the hybrid qubit is a charge qubit and may disregard the spin degrees of freedom (which are on the other hand important for the noise and decoherence description).

Following Refs. [49, 56], we now describe the setup analytically. The induced charge in a disc of the floating gate due to an electron at position $\boldsymbol{r}$ is

$$Q_{\mathrm{ind}}(\boldsymbol{r}) = \frac{2e}{\pi} \arcsin(R/\xi_{\boldsymbol{r}}), \tag{2.1}$$

where e is the elementary positive charge and R is the radius of the disc.

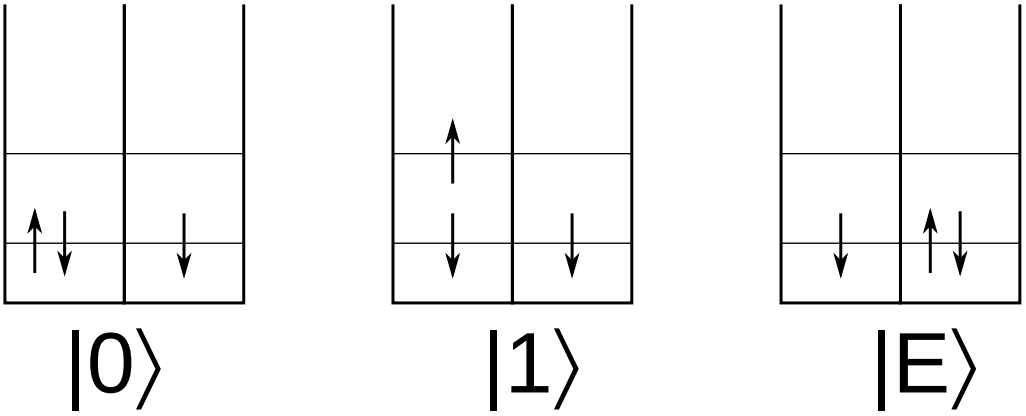

Figure 2.1: States of the double dot hybrid qubit [45–48]. The logical state $|0\rangle$ is defined as $|0\rangle = |S\rangle\,|\downarrow\rangle$, where $|S\rangle$ is the singlet of the two electrons in the ground state of the first dot and $|\downarrow\rangle$ denotes the electron with spin down in the second dot. The logical state $|1\rangle$ is $|1\rangle = \sqrt{1/3}\,|T_0\rangle\,|\downarrow\rangle - \sqrt{2/3}\,|T_-\rangle\,|\uparrow\rangle$, where $|T_0\rangle$ ($|T_-\rangle$) is the two-electron triplet state in the first dot with spin projection zero (-1) along the quantization axis, and $|\uparrow\rangle$ denotes the electron with spin up in the second dot. Our diagram for $|1\rangle$ is a simplified sketch of $|T_0\rangle\,|\downarrow\rangle$. The state $|E\rangle = |\downarrow\rangle\,|S\rangle$ depicted on the right is used as an intermediate state to prepare the logical states. We note that each of these three states can be written in the simple form "orbital part $\times$ spin part", because additional corrections are negligible in our calculations of the coupling strengths.

The ellipsoidal coordinate $\xi_{\boldsymbol{r}}$ is given by [1]

$$\begin{aligned} 2\xi_{\boldsymbol{r}}^2 &= R^2 + d^2 + x^2 + y^2 \\ &\quad + \sqrt{\left(R^2 + d^2 + x^2 + y^2\right)^2 - 4R^2\left(x^2 + y^2\right)}. \end{aligned} \tag{2.2}$$

Assuming that the electron occupies a quantum dot (or DQD in our case) within the two-dimensional electron gas (2DEG) of a heterostructure, the vertical distance d between the electron and the disc corresponds to the distance between the floating gate and the 2DEG, as illustrated in Fig. 2.2a. The coordinates x and y describe the in-plane position of the electron, where the origin $0 = x = y$ was chosen below the center of the disc.

[1] We note that ellipsoidal coordinates found in the literature sometimes have different underlying definitions. Details about the $\xi_{\boldsymbol{r}}$ used here are provided in Ref. [56].

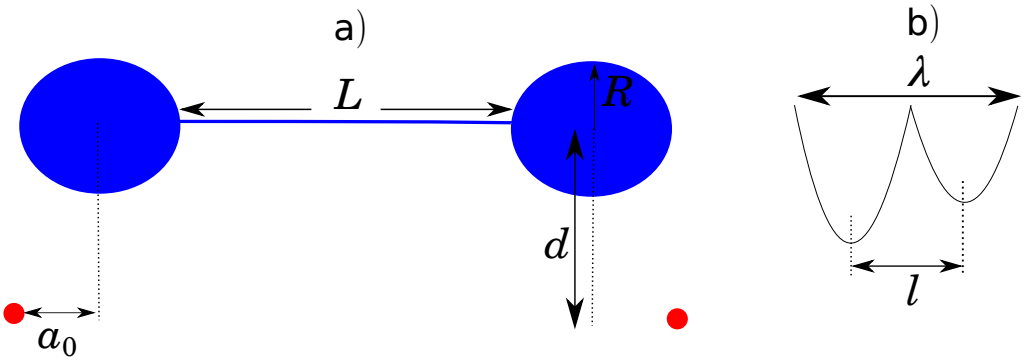

Figure 2.2: a) Setup consisting of a floating metallic gate (blue) and two DQDs (red dots). b) Sketch of the confinement potential of a DQD. Here, a_0 is an in-plane distance between the floating gate disc center and the DQD, d is the vertical distance between the floating gate disc center and the DQD, R is the radius of the floating gate disc, L is the length of the section connecting the discs, R_w is the radius of this section (modelled as a wire), λ is the length of the DQD and l is the distance between the DQD minima.

When one electron is located near the first disc of the floating metallic gate and another electron is located near the second disc, the two electrons are electrostatically coupled and the associated potential energy is[2]

$$v(\boldsymbol{r}_1, \boldsymbol{r}_2) = \frac{\alpha_q Q_{\text{ind}}(\boldsymbol{r}_1) Q_{\text{ind}}(\boldsymbol{r}_2)}{8\epsilon_r \epsilon_0 R}, \tag{2.3}$$

where $\boldsymbol{r}_1$ and $\boldsymbol{r}_2$ are the positions of the two electrons with respect to their nearby disc, ϵ_0 is the vacuum permittivity, ϵ_r is an effective relative permittivity that depends on the details of the setup, and $\alpha_q = C_d/(C_w + 2C_d)$ is a charge-distribution factor that is determined by the capacitances C_d and C_w of the discs and the connecting wire, respectively, of the floating gate [49]. A detailed derivation of Eq. (2.3) is provided in Appendix 2.A.

In order to obtain an estimate of the interaction we need to model the charge distributions in the DQDs for the different logical states. Electrons in the DQDs are trapped inside the two overlapping two-dimensional (2D) parabolic potential wells (see Fig. 2.2b), thus their orbital states in each quantum dot are in good approximation the same as the eigenstates of the 2D simple harmonic oscillator (SHO) [57]. The electron density in

[2]Our formula differs from the one given in Ref. [49] by a factor of 1/2. For the details see Appendix 2.A

a quantum dot, which differs from the charge density only by the factor $-e$ (electron charge), can therefore be modeled by summing up the probability densities of the occupied SHO states.

The probability density in the ground state of a SHO is Gaussian and in the first excited state [58] we have two disjoint peaks shifted with respect to the center of the well to both sides by $\lambda_0 = \sqrt{\hbar/(m^*\omega)}$, where $\hbar\omega$ is the single-particle level spacing in the quantum dot and m^* is the effective mass of the electron. We define $\lambda = l + 2\lambda_0$ as the length of the DQD, where l is the distance between the minima of the potential (see Fig. 2.2b). Using a model as described above, with 2D continuous charge distributions in the plane of a 2DEG, we obtain the following expression for the electrostatic coupling of the two states $|i\rangle$, $|j\rangle$ with electron densities $\rho_i(\boldsymbol{r}_1)$, $\rho_j(\boldsymbol{r}_2)$,

$$V_{ij} = \frac{\alpha_q}{8\epsilon_r\epsilon_0 R} \times \int \mathrm{d}^2\boldsymbol{r}_1 \int \mathrm{d}^2\boldsymbol{r}_2\, Q_{\mathrm{ind}}(\boldsymbol{r}_1) Q_{\mathrm{ind}}(\boldsymbol{r}_2) \rho_i(\boldsymbol{r}_1)\rho_j(\boldsymbol{r}_2). \tag{2.4}$$

These four-dimensional integrals can be evaluated numerically. However, in order to gain more insight, we will also evaluate the V_{ij} analytically by substituting the Gaussian wave functions by delta functions, thus considering the interaction of point charges.

The electron densities in Eq. (2.4) depend not only on the DQD potentials but also on the positions of the DQDs with respect to the discs of the floating gate. For our estimate of the feasible coupling strengths, we assume that the two DQDs have the same dimensions and the same relative positions. More precisely, we choose the two minima of a DQD potential to lie on the x axis (which can be an arbitrary in-plane direction due to the circular symmetry of the discs and which may, in fact, be different for each disc), with the first minimum at $x = a_0$ and the second minimum at $x = a_0 + l$. The parameter a_0 corresponds to the in-plane distance from the disc center, as sketched in Fig. 2.2. In order to enable two-qubit gates with short operation times, this distance should be chosen such that the energies V_{ij} differ strongly when changing the qubit states. In Ref. [49], it was shown that the floating-gate-mediated coupling between two charges is most sensitive to small variations in their positions when the charges are placed below the edges of the discs. Therefore, we set $a_0 = R$ in our model, and in our case of DQDs we choose the dots below the edges of the discs ($x = R$) to be the ones whose charge distributions depend strongest on the qubit states. Our assumptions are illustrated

in Fig. 2.3, which shows both the point charge approximation and the continuous charge distribution for a hybrid qubit.

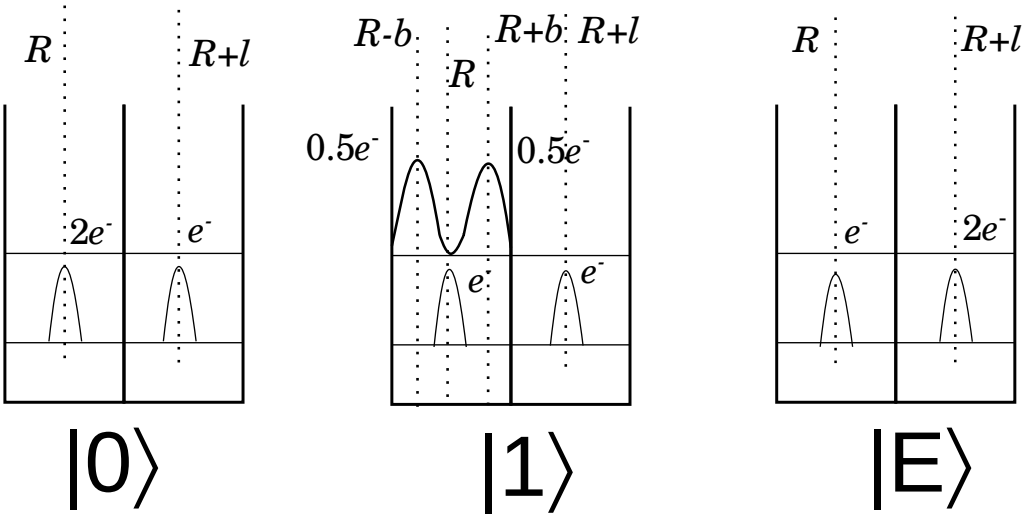

Figure 2.3: Charge distributions in the logical states of the DQD forming the hybrid qubit. In the point charge approximation we model the charge distribution via delta functions localized at the positions (x coordinates) shown by dotted lines, with the corresponding charges written in multiples of the elementary charge $e^- = -e$. In the numerical integration we use for the charge distributions the corresponding eigenfunctions of the parabolic potential.

Now we are prepared to calculate the matrix elements of the electrostatic coupling

$$V = \sum_{m,n} v(\boldsymbol{r}_m, \boldsymbol{r}_n) \tag{2.5}$$

between the different states of two DQDs. In Eq. (2.5), the sum over m and n runs over all possible pairs of electrons that do not occupy the same DQD and v is the electrostatic electron-electron coupling introduced in Eq. (2.3). As the Coulomb interaction does not contain any spin operators, the spins of the states are always conserved. Thus, because the logical states are orthogonal in spin space, we get (where $i, j, k, l = 0, 1, E$)

$$\langle i, j | \, V \, | k, l \rangle = \delta_{ik} \delta_{jl} V_{kl}. \tag{2.6}$$

The used notation $|k, l\rangle$ for a two-qubit state means here that the qubit at the first (second) disc is in state $|k\rangle$ ($|l\rangle$). As an example we can write the

expression for one of the matrix elements in the point charge approximation as follows

$$\begin{aligned}\langle 0,1|\, V\, |0,1\rangle &= v(R-b,R)+\frac{1}{2}v(R-b,R+l)\\ &\quad +v(R+b,R)+\frac{1}{2}v(R+b,R+l)\\ &\quad +2v(R,R)+v(R,R+l)\\ &\quad +2v(R+l,R)+v(R+l,R+l), \end{aligned} \tag{2.7}$$

where $v(x_1,x_2)$ denotes the Coulomb interaction of two electrons placed at the positions x_1, x_2. The charge in the hybrid qubit is equal to three elementary charges, thus the sum of the prefactors of all terms in Eq. (2.7) must be nine.

Due to the aforementioned orthogonality in spin space, projection of V onto the subspace spanned by the two-qubit states $|0,0\rangle$, $|0,1\rangle$, $|1,0\rangle$, and $|1,1\rangle$ yields a diagonal 4×4 matrix

$$V = \mathrm{diag}\left(V_{00}, V_{01}, V_{01}, V_{11}\right), \tag{2.8}$$

where we used $V_{01} = V_{10}$. We can construct a two-qubit gate that is equivalent to the CNOT gate up to single-qubit operations as follows [59],

$$\mathcal{H} = C\sigma_1^z\sigma_2^z, \tag{2.9}$$

$$e^{i\mathcal{H}\frac{\pi}{4C}} = e^{i\frac{\pi}{4}}\begin{pmatrix}1&0&0&0\\0&-i&0&0\\0&0&-i&0\\0&0&0&1\end{pmatrix}. \tag{2.10}$$

When the matrix in Eq. (2.8) is rewritten in terms of Pauli matrices, one obtains

$$\begin{aligned}V &= \frac{V_{00}+V_{11}+2V_{01}}{4}+\frac{V_{00}-V_{11}}{4}\left(\sigma_1^z+\sigma_2^z\right)\\ &\quad +\frac{V_{00}+V_{11}-2V_{01}}{4}\sigma_1^z\sigma_2^z. \end{aligned} \tag{2.11}$$

The last term in this decomposition enables us to implement the CNOT gate [7], and from comparison with Eqs. (2.9) and (2.10) we therefore identify

$$C_{\text{H-H}} = \frac{V_{00}+V_{11}-2V_{01}}{4} \tag{2.12}$$

as the qubit-qubit coupling in the H-H setup.

We choose the parameters of the setup as follows. For the spatial dimensions of the DQDs we assume $\lambda = 250$ nm and $l = 150$ nm, furthermore $d = 100$ nm for the vertical distance and $R = a_0 = 4d$. We estimate $\alpha_q = 0.19$ from [49]

$$\alpha_q \approx \frac{4R\ln(L/R_w)}{\pi L + 8R\ln(L/R_w)}, \tag{2.13}$$

with $L = 10\ \mu$m and $R_w = 30$ nm as the length and radius, respectively, of the thin wire that connects the two discs. Considering GaAs as the host material, we use $\epsilon_r = 13$ (the effective value may in fact be smaller, which would increase the coupling) and note that $\lambda_0 = 50$ nm and the effective electron mass result in $\hbar\omega \simeq 0.5$ meV. With these values, which are similar to those in Ref. [49], we obtain $C_{\text{H-H}} = 2.0 \times 10^{-10}$ eV from the point charge approximation, while $C_{\text{H-H}} = 2.6 \times 10^{-10}$ eV from the continuous charge distributions.

Since these results agree very well, we conclude that the numerical integration is well reproduced by the point charge approximation. One can significantly increase the coupling by varying the setup parameters. The coupling is most significantly dependent on the vertical distance d. Assuming that $d = 10$ nm can be realized, we are able to obtain a coupling strength of $C_{\text{H-H}} = 1\ \mu$eV (see Sec. 2.4).

Next we study the interaction between the ST qubit, i.e., singlet-triplet states of two electrons in the DQD, and the hybrid qubit, i.e., three electrons in the DQD with states $|0\rangle$, $|1\rangle$, and $|E\rangle$, see Fig. 2.3. We assume the DQD for the ST qubit to be in the strongly detuned regime, thus the singlet state is effectively a (2,0) charge state and the triplet state is effectively a (1,1) charge state (excited orbital states of the dots that form the DQD cannot be occupied). Then we are able to calculate the matrix elements, for instance

$$\begin{aligned}\langle S,1|\,V\,|S,1\rangle \;&=\; 2v(R,R) + v(R,R-b) \\ &\quad + v(R,R+b) + 2v(R,R+l).\end{aligned} \tag{2.14}$$

Proceeding analogously to the case of two H qubits, we find a qubit-qubit interaction of the form $C_{\text{H-ST}}\sigma_1^z\sigma_2^z$, where we obtain $C_{\text{H-ST}} = 5.5 \times 10^{-9}$ eV for the point charges and $C_{\text{H-ST}} = 1.4 \times 10^{-8}$ eV for the continuous charge distributions. As a check of the numerics we additionally calculate the ST-ST coupling with the continuous distributions and compare it to the expected value of 10^{-5}–10^{-6} eV obtained from Ref. [49]. We get [58] $C_{\text{ST-ST}} = 7.5 \times 10^{-7}$ eV.

It is then interesting to ask why the obtained H-H and H-ST couplings are much smaller than in the ST-ST case. When we look at the logical states $|0\rangle$ and $|1\rangle$ of the hybrid qubit, we can see that the charge distribution in the second quantum dot is the same in both logical states, thus the second quantum dot gives us no contribution to the coupling, in contrast to the states of the ST qubit. Moreover, the charge difference between the singlet and the triplet states in the single dot is small, $\delta q = 4.7 \times 10^{-5} e$ according to the calculations in Ref. [60], in contrast to the charge difference between the singlet and triplet states in the ST qubit where $\delta q = 2.7 \times 10^{-2} e$.

It is worth mentioning that when we use the state $|E\rangle$ instead of $|1\rangle$ as a computational basis state for the hybrid qubit, we obtain much larger couplings due to the different charge configurations in both wells in the different logical states. For H-H and H-ST we get about the same coupling strengths, $C_{\text{H-H}} \approx C_{\text{H-ST}} \approx 0.1\ \mu$eV, which is on the order of what one would expect for the charge qubit. In the next section we will pursue this idea further, because in order to implement the H-LD coupling it will be necessary to work in the $|0\rangle$, $|E\rangle$ basis.

Finally, we note that a magnetic field is not needed to obtain the H-H, H-ST, and ST-ST couplings. However, a magnetic field is usually applied in order to energetically separate the qubit subspace from other states. The presence of an out-of-plane field, if required, can easily be included by using states of Fock-Darwin type, whose spatial extent decreases (effective confinement increases) with increasing field strength [61,62]. When the magnetic field lies in the plane of the 2DEG, which is the case in most present-day experiments [45,51,53,63,64] , its effects on the orbital states are negligible because of the strong and narrow vertical confinement potential. As a consequence, neither magnetic fields nor SOI are important for the estimates of this section and we can omit them in the calculations. This is in stark contrast to the LD qubits discussed in the next section, where the qubit-qubit coupling depends strongly on both the SOI and the magnetic field.

2.3 H-LD coupling

In this section we want to evaluate the coupling between the hybrid qubit in a DQD and the LD qubit in a single quantum dot. Given the coordinate system introduced in the previous section, we assume that the center of the quantum dot that hosts a LD qubit is located at $x = a_0$ and $y = 0$.

For the sake of simplicity in the notation, the coordinate system which we use in the present section is shifted such that its origin $0 = x = y$ and the center of the quantum dot coincide.

The Hamiltonian of the single quantum dot reads

$$H_{\mathrm{LD}} = H_0 + H_Z + H_{\mathrm{SOI}} \tag{2.15}$$

with

$$H_0 = \frac{p_x^2 + p_y^2}{2m^*} + \frac{m^*\omega^2}{2}\left(x^2 + y^2\right), \tag{2.16}$$

$$H_Z = \frac{g\mu_B}{2}\boldsymbol{B}\cdot\boldsymbol{\sigma}, \tag{2.17}$$

$$H_{\mathrm{SOI}} = \alpha\left(p_x\sigma_y - p_y\sigma_x\right). \tag{2.18}$$

The p_x and p_y are kinetic momentum operators, g is the effective electron g-factor, and $\boldsymbol{\sigma}$ is the vector of Pauli matrices $\sigma_{x,y,z}$. Let us assume that the magnetic field lies in the plane of the 2DEG, i.e., $\boldsymbol{B} = (B_x, B_y, B_z) = B\left(\cos\phi, \sin\phi, 0\right)$, where $B = |\boldsymbol{B}|$. In this case, orbital effects due to $\boldsymbol{B}$ are negligible and one can simply use $p_{x,y} = -i\hbar\partial_{x,y}$. The Zeeman energy induced by $\boldsymbol{B}$ is $E_Z = g\mu_B B$. The Rashba SOI parameter is defined as $\alpha = \frac{\hbar}{m^*\lambda_{\mathrm{SO}}}$, where λ_{SO} is the spin-orbit length. We assume that the SOI is relatively weak and are interested in the regime $1 \gg \frac{|E_Z|}{\hbar\omega} \gg \frac{\lambda_0}{|\lambda_{\mathrm{SO}}|}$. (We allow E_Z and λ_{SO} to be positive or negative depending on the sign of g and α, respectively. As these signs, however, cannot affect the absolute values of the qubit-qubit couplings in our model, the parameters in our calculations will always be chosen positive.) In order to remove H_{SOI} in the first order, we can therefore employ a Schrieffer-Wolff (SW) transformation [61]. The details are described in Appendix 2.B.

The floating gate couples the three electrons forming the hybrid qubit, labeled by positions $\boldsymbol{r_1}, \boldsymbol{r_2}, \boldsymbol{r_3}$, to the electron of the LD qubit, labeled by $\boldsymbol{r_e}$, via the potential

$$V(\boldsymbol{r_e}, \boldsymbol{r_1}, \boldsymbol{r_2}, \boldsymbol{r_3}) = v(\boldsymbol{r_e}, \boldsymbol{r_1}) + v(\boldsymbol{r_e}, \boldsymbol{r_2}) + v(\boldsymbol{r_e}, \boldsymbol{r_3}) \tag{2.19}$$

from Eq. (2.5). By expanding this electrostatic potential around the positions where the confining potential of the dots is minimal, we obtain an effective term H_{int} that describes the floating-gate-mediated interaction between the electrons,

$$H_{\mathrm{int}} = \eta x_e(x_1 + x_2 + x_3), \tag{2.20}$$

$$\eta = \frac{\alpha_q}{8\epsilon_r\epsilon_0 R}\left(\frac{\partial Q_{\mathrm{ind}}}{\partial x}\right)^2\Bigg|_{\boldsymbol{r}_{\min}}. \tag{2.21}$$

The details of this expansion are provided in Appendix 2.C. Remarkably, the term $H_{\rm int}$ is equivalent to that of an electric field applied along the DQD axis, and the strength of this electric field depends on the coordinate x_e of the electron in the quantum dot for the LD qubit. We are now interested in the energy difference

$$J_{01} = \langle 0| H_{\rm int} |0\rangle - \langle 1| H_{\rm int} |1\rangle \tag{2.22}$$

which $H_{\rm int}$ causes between the logical states $|0\rangle$ and $|1\rangle$ of the hybrid qubit. As sketched in Fig. 2.3, the charge distributions of the states $|0\rangle$ and $|1\rangle$ differ only in one valley of the DQD, because one of the two electrons that occupy this valley is raised to an excited orbital state when $|0\rangle$ changes to $|1\rangle$. Consequently, we find $J_{01} = 0$ in our model, as it is known that an electric field applied to a SHO leads to a constant shift of all energy levels. It has already been proposed [46] to use the state $|E\rangle$ instead of $|1\rangle$ to perform a two-qubit gate as the charge difference between those states is large and one can easily pulse the state $|1\rangle$ into $|E\rangle$. One finds that

$$J_{0E} = \langle 0| H_{\rm int} |0\rangle - \langle E| H_{\rm int} |E\rangle \tag{2.23}$$

is non-zero, as a qubit based on the states $|0\rangle$ and $|E\rangle$ is effectively a charge qubit, see Fig. 2.3.

The orbital wave functions of the states $|0\rangle$ and $|E\rangle$ in the DQD are well approximated by

$$\psi_0 = \psi_L(x_1, y_1)\psi_L(x_2, y_2)\psi_R(x_3, y_3), \tag{2.24}$$
$$\psi_E = \psi_L(x_1, y_1)\psi_R(x_2, y_2)\psi_R(x_3, y_3), \tag{2.25}$$

where

$$\psi_L(x, y) = \sqrt{\frac{m^*\omega}{\pi\hbar}} e^{-\frac{m^*\omega}{2\hbar}(x^2+y^2)}, \tag{2.26}$$
$$\psi_R(x, y) = \psi_L(x - l, y). \tag{2.27}$$

Using these orbital wave functions one gets $J_{0E} = -\eta l x_e/2$ which corresponds to an interaction of the form

$$H_{\rm int} = -\frac{\eta l x_e \tau_z}{4}, \tag{2.28}$$

where the Pauli operator τ_z satisfies $\tau_z |0\rangle = |0\rangle$ and $\tau_z |E\rangle = -|E\rangle$.

Finally, we can calculate the H-LD qubit-qubit coupling by considering the aforementioned SW transformation [61]. As explained in detail in Appendix 2.B, the antihermitian operators

$$S_1 = \frac{i}{\lambda_{\rm SO}} \left(x\sigma_y - y\sigma_x \right), \tag{2.29}$$

$$T_1 = \frac{E_Z \lambda_0^2}{i\hbar^2 \omega \lambda_{\rm SO}} \left(p_x \cos\phi + p_y \sin\phi \right) \sigma_z \tag{2.30}$$

are chosen such that the eigenstates of the perturbatively transformed Hamiltonian $H_{\rm LD} + [S_1 + T_1, H_{\rm LD}]$ are eigenstates of the Pauli operator $\sigma_{z'} = \sigma_x \cos\phi + \sigma_y \sin\phi$, apart from small (higher-order) corrections. When we apply the same transformation to $H_{\rm int}$, keeping in mind that x_e in Eq. (2.28) corresponds to x in Eqs. (2.29) and (2.30), we identify

$$[T_1, H_{\rm int}] = C_{\text{H-LD}} \sigma_{y'} \tau_z \tag{2.31}$$

as the H-LD coupling. We note that the form of this qubit-qubit coupling differs from those in Sec. 2.2 because the axes of the Pauli operators $\sigma_{z'}$ and $\sigma_{y'} = \sigma_z$ are perpendicular to each other. The strength of the H-LD coupling is

$$C_{\text{H-LD}} = \frac{\alpha_q \lambda_0^2 l E_Z \cos\phi}{32 \epsilon_r \epsilon_0 R \lambda_{\rm SO} \hbar\omega} \left(\frac{\partial Q_{\rm ind}}{\partial x} \right)^2 \Bigg|_{\boldsymbol{r}_{\rm min}}, \tag{2.32}$$

and we recall that $\lambda_0 = \sqrt{\hbar/(m^*\omega)}$.

In this calculation we included Rashba SOI only. One can perform the SW transformation including both Dresselhaus and Rashba SOIs with the following modifications. If the magnetic field is in the plane and if the angle γ between the crystallographic [100] axis and the x axis of our coordinate system is tuned to $\pi/4$, it then follows from Eq. (B10) in Ref. [49] that the Dresselhaus SOI coefficient β induces a simple shift of the Rashba SOI as $\tilde{\alpha} = \alpha + \beta$. The same effect can also be achieved by choosing the in-plane magnetic field along the x axis, regardless of the value of γ, and in this case we have $\tilde{\alpha} = \alpha + \beta \sin(2\gamma)$.

2.4 Dependence on setup geometries and host materials

As evident from Eq. (2.32), we can obtain a stronger H-LD coupling by using a quantum dot material with a stronger SOI (like InAs). To verify

this statement, we calculated the couplings for the fixed setup parameters mentioned before for different materials, with the following material parameters: for GaAs [49] $\lambda_{\rm SO} = 2.0 \times 10^{-6}$ m, $m^* = 0.067m_e$, $\hbar\omega = 0.5$ meV, $\epsilon_r = 13$, for InAs [65] $\lambda_{\rm SO} = 1.64 \times 10^{-7}$ m, $m^* = 0.023m_e$, $\hbar\omega = 1.3$ meV, $\epsilon_r = 15.15$, in Si [66] $\lambda_{\rm SO} = 2.6 \times 10^{-5}$ m, $m^* = 0.26m_e$, $\hbar\omega = 0.1$ meV, $\epsilon_r = 11.7$, and for $\rm Si_{0.9}Ge_{0.1}$ [67] $\lambda_{\rm SO} = 2 \times 10^{-5}$ m, $m^* = 0.19m_e$, $\hbar\omega = 0.2$ meV, $\epsilon_r = 12.2$. We have chosen ω in every material such that it is experimentally well accessible and keeps λ_0 close to 50 nm. The Zeeman energy is always set to $E_Z = 0.5\hbar\omega$. Given these parameters, the results for the qubit-qubit couplings $C_{\text{H-H}}$, $C_{\text{H-ST}}$, and $C_{\text{H-LD}}$ are listed in Table I. However, the couplings for this setup are rather small. If we want to further enhance them, we need to consider smaller geometries. The simplest way is to equally shorten the distance d, the disc radius R, and the horizontal distance a_0 between the centers of disc and dot, such that $a_0 = R = 4d$ is preserved. Reducing R also results in a small decrease of α_q, which however does not dominate the parameter dependence of the qubit-qubit couplings. As expected from Eqs. (2.1)–(2.3), the couplings depend strongest on the vertical distance d between the dots and the metallic gate. To quantify this dependence, we calculated the couplings again for two smaller setups. In Table II, we present the results for currently feasible [43] fabrication parameters with $d = 57$ nm, $R = a_0 = 228$ nm, and $\alpha_q = 0.13$, and in Table III for $d = 10$ nm, $R = a_0 = 40$ nm, and $\alpha_q = 0.03$ to demonstrate the strong dependence on d. The parameters $\lambda = 250$ nm and $l = 150$ nm of the DQD and the angle $\phi = 0$ of the magnetic field in the H-LD case are always fixed.

As anticipated, a strong SOI is needed for implementing the H-LD coupling, which is why the calculated $C_{\text{H-LD}}$ in Tables I–III are largest for InAs. In order to enhance the relatively weak H-LD couplings in Si and $\rm Si_{0.9}Ge_{0.1}$, one can add a micromagnet [68–70] to the setup, because the magnetic field gradient caused by a micromagnet can result in a very strong effective SOI. Considering the transformation discussed in Sec. 2.3 and Appendix 2.B, one obtains [71–73]

$$\left[S_1, \frac{g\mu_B}{2}\boldsymbol{B}\cdot\boldsymbol{\sigma}\right] = \frac{g\mu_B B}{\lambda_{\rm SO}}\left(x\cos\phi + y\sin\phi\right)\sigma_z, \tag{2.33}$$

where S_1 is the antihermitian operator of Eq. (2.29) and $\boldsymbol{B}\cdot\boldsymbol{\sigma} = B(\sigma_x\cos\phi + \sigma_y\sin\phi)$ due to the in-plane magnetic field. In particular, when we choose $\phi = 0$ as in our calculations for $C_{\text{H-LD}}$ in Tables I–III, the transformed Zeeman term is simply $g\mu_B B x\sigma_z/\lambda_{\rm SO}$, which corresponds to the

effect of an out-of-plane magnetic field that increases linearly with the coordinate x. Assuming that the micromagnet provides such a magnetic field $b_{\mathrm{MM}}x$ along the z axis, with b_{MM} as the gradient, the total (effective) gradient b_{tot} is therefore [70]

$$b_{\mathrm{tot}} = b_{\mathrm{MM}} + \frac{2B}{\lambda_{\mathrm{SO}}}. \tag{2.34}$$

Consequently, even if a material does not feature Rashba or Dresselhaus SOI at all, a spin-orbit length of the order of $2B/b_{\mathrm{MM}}$ can be induced by a micromagnet (the estimate presented here applies when $|\lambda_{\mathrm{SO}}| \gg \lambda_0$). Experimental setups with $b_{\mathrm{MM}} \sim 1\ \mathrm{T}/\mu\mathrm{m}$ are already well feasible [70], which results in an effective spin-orbit length $\lambda_{\mathrm{SO}} \sim 2 \times 10^{-6}$ m when we keep our other parameters for the Si and $\mathrm{Si_{0.9}Ge_{0.1}}$ setups unchanged. In both Si and $\mathrm{Si_{0.9}Ge_{0.1}}$, we find that the considered gradient from the micromagnet increases the H-LD couplings by an order of magnitude. For instance, using the setup with $d = 10$ nm and micromagnets to enhance the SOI, one can reach $C_{\text{H-LD}} \sim 0.5\ \mu$eV for Si 2DEGs.

For a comparison of the H-H and H-ST couplings in Tables I–III, it is important to keep in mind that the materials differ from each other only in the relative permittivities ϵ_r and effective masses m^* in the context of this calculation. As we chose different values of ω for the different materials, such that the confinement length λ_0 is approximately constant, we find that the listed values of $C_{\text{H-H}}$ and $C_{\text{H-ST}}$ are quite similar, because it is evident from Sec. 2.2 that the couplings $C_{\text{H-H}}$ and $C_{\text{H-ST}}$ are independent of m^* when λ_0 is fixed. Thus, the small differences that remain in the H-H and H-ST cases between the couplings obtained for the various 2DEGs are solely caused by the small variations in λ_0 and the relative permittivity.

In our analysis of the charge distributions in the states of single and double quantum dots, we assumed that all wave functions of excited states have an excited orbital part. In Si, we therefore assume that the orbital level spacing $\hbar\omega = 0.1$ meV is smaller than the valley splitting, which is reasonable because reported valley splittings are of the order of 0.1–1 meV [29, 74–76]. For instance, Ref. [76] reports an electrically tunable valley splitting in the range of 0.3–0.8 meV for a quantum dot in $\mathrm{Si/SiO_2}$. Consequently, forming Si quantum dots with sufficiently large valley splittings is clearly possible (analogous for $\mathrm{Si_{0.9}Ge_{0.1}}$).

At the end of this section, we would like to summarize some important dependences of the qubit-qubit couplings on the sample parameters. For the H-H coupling, we can conclude from Eqs. (2.1)–(2.3) that

$C_{\text{H-H}} \sim \frac{1}{d^2}, \frac{1}{R}$, and the same applies of course to the H-ST coupling $C_{\text{H-ST}}$. Moreover, Eq. (2.32) reveals that $C_{\text{H-LD}} \sim B, \alpha, \omega^{-2}$ for the H-LD coupling.

Finally, we wish to emphasize that additional electric gates, which are used to control and manipulate the qubits in an experimental setup, were not yet included in our calculations. As shown in Ref. [49], the influence of these surrounding gates can increase the qubit-qubit couplings by another two orders of magnitude, which makes the hybrid qubit a highly promising platform for quantum computation.

Coupling C [μeV]	InAs	GaAs	$Si_{0.9}Ge_{0.1}$	Si
H-H	2.8×10^{-4}	2.6×10^{-4}	2.2×10^{-4}	4.7×10^{-4}
H-ST	1.3×10^{-2}	1.4×10^{-2}	1.3×10^{-2}	1.9×10^{-2}
H-LD	3.5×10^{-2}	3.0×10^{-3}	2.8×10^{-4}	3.3×10^{-4}

Table 2.1: Calculated strengths of the coupling between the three different types of qubits [spin-$1/2$ (LD), singlet-triplet (ST), and hybrid (H) qubit] in DQDs for $d = 100$ nm, $\alpha_q = 0.19$, $R = a_0 = 400$ nm (see Fig. 2.2) for four different semiconducting materials commonly used for the realization of DQDs. We note that in the H-LD case, the two-qubit gate is assumed to be performed in the $|0\rangle, |E\rangle$ basis of the hybrid qubit. In all these calculations we used the continuous charge densities.

Coupling C [μeV]	InAs	GaAs	$Si_{0.9}Ge_{0.1}$	Si
H-H	2.7×10^{-3}	2.6×10^{-3}	2.2×10^{-3}	4.5×10^{-3}
H-ST	6.5×10^{-2}	7.0×10^{-2}	6.5×10^{-2}	9.5×10^{-2}
H-LD	1.3×10^{-1}	1.1×10^{-2}	1.0×10^{-3}	1.2×10^{-3}

Table 2.2: Same as in Table I for $d = 57$ nm, $\alpha_q = 0.13$ and $R = a_0 = 228$ nm.

2.5 Conclusions

We have studied an experimentally realizable setup which allows different types of qubits in DQDs to be coupled over long distances. In par-

Coupling C [μeV]	InAs	GaAs	$Si_{0.9}Ge_{0.1}$	Si
H-H	3.3×10^{-1}	3.7×10^{-1}	3.7×10^{-1}	4.4×10^{-1}
H-ST	1.3	1.5	1.6	1.5
H-LD	5.6	4.7×10^{-1}	4.5×10^{-2}	5.2×10^{-2}

Table 2.3: Same as in Table I for $d = 10$ nm, $\alpha_q = 0.03$ and $R = a_0 = 40$ nm. In this setup, as $\lambda = 250$ nm the point charge approximation would be very imprecise and should not be expected to be comparable with our results obtained with the continuous densities.

ticular, we have shown that using a metallic floating gate, it is possible to capacitively couple the hybrid qubit to a single spin 1/2, to a singlet-triplet qubit, or to another hybrid qubit. First we employed a simple approximation, where the charge density within the quantum dot is treated as a point charge distribution, and calculated the couplings between two hybrid qubits as well as between the ST and the hybrid qubit. Furthermore, we have verified the validity of the point charge approximation by numerically integrating over the continuous charge distribution within each quantum dot. Next, we have calculated perturbatively the coupling between the LD and the hybrid qubit, assuming that the latter is based on the states $|0\rangle$ and $|E\rangle$. In order to investigate the influence of the quantum dot material and the setup geometry, we have calculated the couplings for the four semiconducting materials GaAs, InAs, Si, $Si_{0.9}Ge_{0.1}$, and the three different setups of Tables I–III.

As anticipated, the strongest H-LD coupling is obtained with InAs, which features the strongest SOI. Nevertheless, as explained in Sec. 2.4, micromagnets enable a strong, effective SOI (and therefore strong H-LD couplings) even in materials where the intrinsic SOI is weak, such as Si or $Si_{0.9}Ge_{0.1}$.

For setups with a small distance $d = 10$ nm between the 2DEG and the floating gate, our calculated H-LD, H-ST, and H-H couplings are of the order of one microelectronvolt (see Table III), which leads to very fast two-qubit gates with subnanosecond operation times. In fact, such short time scales may already be possible with present-day samples (see Table II, $d = 57$ nm), assuming that the qubit-qubit couplings increase by two orders of magnitude, as simulated in Ref. [49], when all elements of the sample, especially all the electric gates, are included in the calculation.

In conclusion, we showed that hybrid qubits can be very strongly coupled over long distances via floating metallic gates, enabling long-range two-qubit gates with short operation times and all-electrical control. This applies to all of the studied materials, including Si and $\mathrm{Si_{0.9}Ge_{0.1}}$. We note that Ge and Si can be grown nuclear-spin-free and are therefore highly useful for implementing spin qubits with long dephasing times [51]. Our results prove that hybrid qubits are a promising platform for quantum information processing and quantum computation with spins in quantum dots.

2.A Derivation of the electron-electron coupling mediated by the floating gate

In this appendix we explain Eqs. (2.1)–(2.3) of the main text in more detail and provide an intuitive picture for the derivation of the electrostatic electron-electron interaction described by Eq. (2.3).

We consider a thin conducting disc of radius R and assume for now that it is grounded. When an electron is located nearby, the charge [56]

$$Q_{\mathrm{ind}}(\boldsymbol{r}) = \frac{2e}{\pi}\arcsin(R/\xi_{\boldsymbol{r}}) \tag{2.35}$$

is induced in the disc, where e is the elementary positive charge. Defining the center of the disc as the origin of the coordinate system, the ellipsoidal coordinate $\xi_{\boldsymbol{r}} > R$ is related to the position $\boldsymbol{r} = (x, y, z)$ of the electron via

$$\begin{aligned} 2\xi_{\boldsymbol{r}}^2 &= R^2 + x^2 + y^2 + z^2 \\ &\quad + \sqrt{\left(R^2 + x^2 + y^2 + z^2\right)^2 - 4R^2(x^2 + y^2)}, \end{aligned} \tag{2.36}$$

which corresponds to the solution of

$$\frac{x^2 + y^2}{\xi_{\boldsymbol{r}}^2} + \frac{z^2}{\xi_{\boldsymbol{r}}^2 - R^2} = 1 \tag{2.37}$$

that satisfies $\xi_{\boldsymbol{r}} > R$ [77]. The Cartesian coordinate system was chosen here such that the disc lies in the x-y plane. It is important to note that Eq. (2.35) for the induced charge does not change when we allow the system to be immersed in a dielectric medium with relative permittivity ϵ_r. This might initially be surprising, but it becomes easily comprehensible when one keeps in mind that the electrostatic potential due to the

electron and the induced charge Q_{ind} must compensate at the grounded disc. Keeping Q_{ind} fixed, the potential of both the electron and the disc are inversely proportional to ϵ_r (which is also seen, for instance, in the capacitance $8\epsilon_r\epsilon_0 R$ of a disc in a dielectric), and so the solution for Q_{ind} must indeed be independent of the relative permittivity. In our setup (Fig. 2.2), where vacuum above the floating gates and different layers of materials may be involved, small corrections to Eq. (2.35) can be expected which, however, will only have minor quantitative effects on our results. A detailed derivation of Eq. (2.35) is provided in Ref. [56], using the aforementioned assumption that the disc is grounded. In fact, even though the attached wire and the second disc of our floating gate correspond to a finite reservoir, the assumption of a grounded disc is not satisfied because the floating gate is isolated and so the total charge in the gate must be conserved. Nevertheless, as explained in the following, Eq. (2.35) can be exploited to calculate the steady-state charge distribution of the floating gate.

Given our gate geometry of Fig. 2.2, we now assume that an electron is brought close to one of the discs, referred to as disc 1. After a very short (subpicosecond) time [49], much shorter than the typical duration of a quantum operation on a qubit, the charge distribution in the metallic gate will have reached a steady state which can be described by the following simple requirements,

$$\frac{Q_{d1}}{C_d} - \frac{Q_{\mathrm{ind},1}}{C_d} = \frac{Q_w}{C_w} = \frac{Q_{d2}}{C_d}, \tag{2.38}$$

$$Q_{d1} + Q_w + Q_{d2} = 0. \tag{2.39}$$

With Eq. (2.38), we exploit that the floating gate is conducting, and so the potential at disc 1, the connecting wire, and disc 2 must be the same. Equation (2.39) arises from charge conservation in the floating gate. The introduced quantities Q_{d1}, Q_w, and Q_{d2} are the charges in disc 1, the wire, and disc 2, respectively. The capacitance of the wire is C_w and, assuming a symmetric gate geometry, each of the two discs has the capacitance C_d. The term $-Q_{\mathrm{ind},1}/C_d$ on the left-hand side of Eq. (2.38) accounts for the additional potential at disc 1 which results from the external electron. If $Q_{d1} = Q_{\mathrm{ind},1}$, this term is exactly compensated, and so $Q_{\mathrm{ind},1}$ can be interpreted as the charge that would be induced in disc 1 and that would remain there if the disc were grounded [see also Eq. (2.35)]. Solving the system of three equations contained in Eqs. (2.38) and (2.39) yields the

charge distribution in the steady state,

$$Q_{d1} = Q_{\mathrm{ind},1}\frac{C_w + C_d}{C_w + 2C_d}, \tag{2.40}$$

$$Q_w = -Q_{\mathrm{ind},1}\frac{C_w}{C_w + 2C_d}, \tag{2.41}$$

$$Q_{d2} = -Q_{\mathrm{ind},1}\frac{C_d}{C_w + 2C_d}. \tag{2.42}$$

In particular, defining

$$\alpha_q = \frac{C_d}{C_w + 2C_d}, \tag{2.43}$$

we see from Eq. (2.42) that the electron near disc 1 results in a charge $Q_{d2} = -\alpha_q Q_{\mathrm{ind},1}$ in disc 2.

Next, we analyze the electric potential around the second disc, which is charged by Q_{d2}. When a thin conducting disc with radius R and charge Q is surrounded by a dielectric with relative permittivity ϵ_r, the potential at a position $\boldsymbol{r} = (x, y, z)$ with $\xi_{\boldsymbol{r}} > R$ is

$$\Phi(\boldsymbol{r}) = \frac{Q}{4\pi\epsilon_r\epsilon_0 R}\arcsin(R/\xi_{\boldsymbol{r}}). \tag{2.44}$$

Again, the ellipsoidal coordinate $\xi_{\boldsymbol{r}}$ is given by Eq. (2.36) if the disc lies in the x-y plane of the chosen Cartesian coordinate system and if the center of the disc and the origin coincide. The result in Eq. (2.44) is identical with those provided, e.g., in Refs. [56,78], keeping in mind some properties of inverse trigonometric functions such as

$$\arcsin(R/\xi_{\boldsymbol{r}}) = \arctan\left(R/\sqrt{\xi_{\boldsymbol{r}}^2 - R^2}\right) \tag{2.45}$$

and

$$\arcsin(R/\xi_{\boldsymbol{r}}) = R\int_{\xi_{\boldsymbol{r}}}^{\infty}\frac{d\xi}{\xi\sqrt{\xi^2 - R^2}} \tag{2.46}$$

for $\xi_{\boldsymbol{r}} > R$. In our setup, the potential within the material below disc 2 is therefore well described by

$$\Phi(\boldsymbol{r}_2) = \frac{Q_{d2}}{4\pi\epsilon_r\epsilon_0 R}\arcsin(R/\xi_{\boldsymbol{r}_2}), \tag{2.47}$$

where the subscript added to $\boldsymbol{r}_2$ and $\xi_{\boldsymbol{r}_2}$ refers to the second disc and where ϵ_r may be replaced by an effective value if, e.g., the floating gate

is located at the sample surface (partially in vacuum) or if the sample consists of multiple layers.

Finally, we can combine the previous equations and calculate the electron-electron coupling mediated by the floating gate. Given our result for $\Phi(\boldsymbol{r}_2)$, Eq. (2.47), the associated potential energy v of an electron below disc 2 is simply $-e\Phi(\boldsymbol{r}_2)$. Referring to the position of the electron below disc 1 as $\boldsymbol{r}_1$, the combination of Eqs. (2.35), (2.42), (2.43), and (2.47) yields

$$\begin{aligned} v(\boldsymbol{r}_1,\boldsymbol{r}_2) &= \frac{e\alpha_q Q_{\rm ind}(\boldsymbol{r}_1)}{4\pi\epsilon_r\epsilon_0 R}\arcsin(R/\xi_{\boldsymbol{r}_2}) \\ &= \frac{\alpha_q}{8\epsilon_r\epsilon_0 R}Q_{\rm ind}(\boldsymbol{r}_1)Q_{\rm ind}(\boldsymbol{r}_2), \end{aligned} \tag{2.48}$$

which is the result shown in Eq. (2.3) of the main text. We note that the same result is obtained when one starts the derivation at disc 2 instead of disc 1, which is also evident from the symmetric form of the final expression. As a last remark, we mention that this coupling may be interpreted as

$$v(\boldsymbol{r}_1,\boldsymbol{r}_2) \approx \frac{Q_{\rm ind}(\boldsymbol{r}_1)Q_{\rm ind}(\boldsymbol{r}_2)}{C_w + 2C_d} \tag{2.49}$$

with the approximation $C_d \approx 8\epsilon_r\epsilon_0 R$, which simply corresponds to the product of the induced charges [Eq. (2.35)] divided by the total capacitance of the floating gate.

2.B Schrieffer-Wolff transformation

In this appendix we provide the details of the SW transformation that was performed in Sec. 2.3 of the main text. We note that this transformation is often exploited in the literature [49, 61, 71–73].

Given the Hamiltonian in Eq. (2.15) and the regime $1 \gg \frac{|E_Z|}{\hbar\omega} \gg \frac{\lambda_0}{|\lambda_{\rm SO}|}$, we consider two consecutive unitary transformations in order to remove the SOI perturbatively,

$$H'_{\rm LD} = e^T e^S H_{\rm LD} e^{-S} e^{-T}, \tag{2.50}$$

$$S = S_1 + \ldots, \tag{2.51}$$

$$T = T_1 + \ldots, \tag{2.52}$$

where "..." stands for additional terms of higher order. We choose the form of S_1 such that the strongest term of the SOI is eliminated,

$$[S_1, H_0] = -H_{\mathrm{SOI}}, \tag{2.53}$$

$$S_1 = \frac{i}{\lambda_{\mathrm{SO}}}(x\sigma_y - y\sigma_x). \tag{2.54}$$

Since

$$[S_1, H_Z] = H_{\mathrm{SOI}}^Z = \frac{E_Z}{\lambda_{\mathrm{SO}}}\left(x\cos\phi + y\sin\phi\right)\sigma_z,$$

we have to apply the second transformation such that H_{SOI}^Z is removed,

$$[T_1, H_0] = -H_{\mathrm{SOI}}^Z, \tag{2.55}$$

$$T_1 = \frac{E_Z\lambda_0^2}{i\hbar^2\omega\lambda_{\mathrm{SO}}}\left(p_x\cos\phi + p_y\sin\phi\right)\sigma_z. \tag{2.56}$$

Moreover, as the eigenstates of H'_{LD} correspond essentially to the eigenstates of $H_0 + H_Z$ and because we consider an in-plane magnetic field $\boldsymbol{B} = B\left(\boldsymbol{e}_x\cos\phi + \boldsymbol{e}_y\sin\phi\right)$, with $\boldsymbol{e}_i$ as unit vectors for the respective directions, we introduce new basis vectors $\boldsymbol{e}_{z'} = \boldsymbol{e}_x\cos\phi + \boldsymbol{e}_y\sin\phi$, $\boldsymbol{e}_{y'} = \boldsymbol{e}_z$, and $\boldsymbol{e}_{x'} = \boldsymbol{e}_y\cos\phi - \boldsymbol{e}_x\sin\phi$. Consequently,

$$\sigma_x = \sigma_{z'}\cos\phi - \sigma_{x'}\sin\phi, \tag{2.57}$$

$$\sigma_y = \sigma_{x'}\cos\phi + \sigma_{z'}\sin\phi, \tag{2.58}$$

$$\sigma_z = \sigma_{y'}, \tag{2.59}$$

and

$$H_Z = \frac{E_Z}{2}\sigma_{z'}. \tag{2.60}$$

2.C Expansion of the interaction potential

When we expand the electrostatic potential in Sec. 2.3 around the positions of the quantum dots, we follow the approach discussed in Appendix B of Ref. [49]. In the following, we focus on the expansion of the term $v(\boldsymbol{r_e}, \boldsymbol{r_1})$, as the other terms $v(\boldsymbol{r_e}, \boldsymbol{r_2})$ and $v(\boldsymbol{r_e}, \boldsymbol{r_3})$ are expanded analogously.

We assume that the quantum dot that hosts the LD qubit is located below the edge of one of the metallic discs. Referring to the coordinate system introduced in Sec. 2.2 (2DEG in x-y plane, origin $0 = x = y$ below

the center of the nearby disc), we thus assume that the confining potential of the quantum dot is minimal at the coordinates $x = a_0 = R$ and $y = 0$. Analogously, we consider the DQD with the hybrid qubit to be located below the edge of the other metallic disc. In our model, the coordinates of the dot that contains two electrons when the hybrid qubit is in the state $|0\rangle$ are $x = a_0 = R$ and $y = 0$. The coordinates of the second dot of the DQD are $x = a_0 + l$ and $y = 0$. Thus, keeping in mind that the origins of the coordinate systems for the LD and the hybrid qubit are related to the respective metallic discs, we find that a minimum of the confining potential occurs at the position $\boldsymbol{r}_{\min} = (a_0, 0) = (R, 0)$ for both qubits.

As we are interested in the qubit-qubit coupling that results from $v(\boldsymbol{r_e}, \boldsymbol{r_1})$, we are looking for terms of type $x_e x_1$, $x_e y_1$, $y_e x_1$, or $y_e y_1$ in the expansion. All the other terms up to the second power in coordinates cannot lead to a qubit-qubit interaction. Moreover, as the quantum dots are displaced by a_0 along the x axis only, we find

$$\left(\frac{\partial Q_{\text{ind}}}{\partial y}\right)\bigg|_{y=0} = 0. \tag{2.61}$$

Thus, the expansion up to the second power in coordinates yields

$$v(\boldsymbol{r_e}, \boldsymbol{r_1}) \approx \ldots + \eta x_e x_1, \tag{2.62}$$

where "…" stands for all the constant or frequency-rescaling terms that do not affect the qubit-qubit coupling and

$$\eta = \frac{\alpha_q}{8\epsilon_r \epsilon_0 R} \left(\frac{\partial Q_{\text{ind}}(\boldsymbol{r_e})}{\partial x_e}\right)\bigg|_{\boldsymbol{r}_{\min}} \left(\frac{\partial Q_{\text{ind}}(\boldsymbol{r_1})}{\partial x_1}\right)\bigg|_{\boldsymbol{r}_{\min}}. \tag{2.63}$$

Thus, due to the assumed symmetry in the setup, the constant η can be written in the short form

$$\eta = \frac{\alpha_q}{8\epsilon_r \epsilon_0 R} \left(\frac{\partial Q_{\text{ind}}}{\partial x}\right)^2\bigg|_{\boldsymbol{r}_{\min}}. \tag{2.64}$$

After such an expansion of all three terms $v(\boldsymbol{r_e}, \boldsymbol{r_1})$, $v(\boldsymbol{r_e}, \boldsymbol{r_2})$, and $v(\boldsymbol{r_e}, \boldsymbol{r_3})$ of the interaction potential, we obtain Eqs. (2.20) and (2.21) of the main text.

CHAPTER 3

Lateral Quantum Dot in a Strong In-plane Magentic Field

Adapted from:
Peter Stano, Chen-Hsuan Hsu, Marcel Serina, Leon C. Camenzind, Dominik M. Zumbühl, and Daniel Loss
"Gate-defined quantum dot in a strong in-plane magnetic field: spin-orbit and g-factor effects",
arXiv:1808.03963

We analyze orbital effects of an in-plane magnetic field on the spin structure of states of a gated quantum dot based in a two-dimensional electron gas. Starting with a $k \cdot p$ Hamiltonian, we perturbatively calculate these effects for the conduction band of GaAs, up to the third power of the magnetic field. We quantify several corrections to the g-tensor and reveal their relative importance. We find that for typical parameters, the Rashba spin-orbit term and the isotropic term, $H_{43} \propto \mathbf{P}^2\mathbf{B} \cdot \boldsymbol{\sigma}$, give the largest contributions in magnitude. The in-plane anisotropy of the g-factor is, on the other hand, dominated by the Dresselhaus spin-orbit term. At zero magnetic field, the total correction to the g-factor is typically 5-10% of its bulk value. In strong in-plane magnetic fields the corrections are modified appreciably.

3.1 Introduction

Spin qubits in gated quantum dots [6, 7, 26] based in two dimensional electron gas (2DEG) are now seeing a resurge in interest due to a recent progress in GaAs [79–84] and, especially, in potentially nuclear-spin-free materials like Si, [43, 85–91] Ge, [92, 93] and C. [94] Many of the experiments are done applying relatively strong in-plane magnetic fields, in the order of Teslas. It is a well established fact that such in-plane magnetic fields have sizable effects in 2DEGs. [95] It motivated us in Ref. 96 to analyze the effects of the in-plane magnetic fields on the orbital structure of the quantum dot states. There we laid down the theory for using such effects as a new spectroscopic tool of quantum dots. The idea was conceived in Ref. 97, which demonstrated that the shape of quantum mechanical orbitals of a quantum dot can be inferred in this way. The information on the quantum dot shape thus acquired was essential for the experimental quantification of the spin-orbit couplings in Ref. 98, further demonstrating the power of this tool.

In this article, we extend the investigations of Ref. 96 to the spin structure of a quantum dot. The spin-dependent corrections due to the orbital effects of the in-plane field appear, first, as corrections to the spin-orbit interactions, such as Rashba and Dresselhaus terms in GaAs. Importantly, in the presence of magnetic field additional spin-orbit terms arise, which are present even in bulk- and interface- inversion symmetric structures. These, as well as the magnetic-field induced corrections to the inversion-asymmetry originated ones, are not time reversal symmetric. They can therefore directly—in the lowest order—change the energy splitting of a pair of time reversed states (spin 'up' and 'down' corresponding to the same orbital). We expect that such energy effects are their most important consequence, and therefore mainly restrict ourselves to evaluating the corresponding renormalization of the g-factor.

We derive a dozen of different terms for the g-factor corrections, Eqs. (3.43)–(3.50), constituting our main results. They differ in the dependence on the 2DEG width (increase or decrease), magnetic field magnitude (constant, or magnetic-field dependent), and direction (isotropic, anisotropic and relating to the crystal axes, or anisotropic and relating to the quantum dot axes), heterostructure interface electric field (dependent, or largely independent on it), and symmetry of the heterostructure confinement (present only in asymmetric 2DEGs or present also in symmetric quantum wells).

There is vast literature concerning g-factor theory and experiments.

Instead of trying for its overview, we only refer to works which have direct connection to our results. The g-factor corrections that we calculate here are solely bandstructure (or single particle) effects. They correspond to experiments with GaAs occupied by a single or a few particles. [99–101] In another words, our theory does not cover the g-factor changes arising from the electron–electron interaction-induced exchange, [102, 103] which is also modulated by magnetic field, for example, through the induced renormalization of the electron mass. [104] Second, we also do not analyze the effects of strain, [105, 106] assuming that it is negligible in the lattice matched AlGaAs/GaAs heterostructres. Finally, we focus on gated dots, where the effects are perturbative, unlike in self-assembled dots, where they are of order one. [107, 108] Among recent works, Ref. 109 is very close to what we do here, and Ref. 110 is also similar in spirit.

Our results can be exploited in several ways. First, they should be taken as the theory accompanying the current experiments, which have in GaAs dots reached resolution required to extract effects of such small magnitude. [111] Fitting data from such experiments, one could aim at extracting the $k \cdot p$ parameters, which are still under vivid debate even in the best known semiconductors. [112] From the point of view of spin qubits, the inhomogeneities in the g-factor are a primary agent for, on one hand, spin manipulation and, on the other, coupling to the charge noise.

The article is structured as follows. In Section II we present the approach. It is a perturbative calculation introduced in Ref. 96. Here, we extend it by spin-dependent terms arising up to the fourth order in a $k \cdot p$ theory for the Γ_6 conduction band of a zinc-blende crystal with T_d symmetry. Section III exemplifies how the spin-dependent effects arise due to the in-plane field orbital effects, and motivates approximations that we adopt for the rest of the calculations. Section IV lists and analyses the diagonal corrections to the g-tensor for a purely in-plane magnetic field. We delegate calculation details and additional material to appendices. Appendix 3.A lists the off-diagonal components of the g-tensor. Appendix 3.B contains detailed derivations of all the g-tensor corrections using the third order perturbation theory. Appendix 3.C lists dimensionless constants which enter the results. Appendix 3.D discusses the g-factor corrections for a symmetric quantum well. Appendix 3.E shows an example for the g-factor corrections quadratic in the magnetic field. Appendix 3.F estimates the leading correction of higher order in spin-orbit constants, showing that they are indeed negligible compared to the

leading order ones that we discuss in the main text.

3.2 Definitions and methods

We now introduce the method. It is a straightforward extension of the approach explained in detail in Ref. 96, so we only recapitulate it shortly. It starts with a three dimensional Hamiltonian of the heterostructure,

$$H = T(\mathbf{P}) + V(\mathbf{R}) + H_{\mathrm{Z}}, \tag{3.1}$$

which comprises the kinetic, potential, and Zeeman terms. The kinetic energy operator T is a function of the kinetic momentum

$$\mathbf{P} = -i\hbar(\partial_x, \partial_y, \partial_z) + e\mathbf{A}, \tag{3.2}$$

where e is the proton charge, and the vector potential $\mathbf{A}$ is due to the magnetic field $\mathbf{B} = (B_x, B_y, B_z)$. The confinement potential $V(\mathbf{R})$, is due to gates and material composition, as specified below.

We consider a structure grown along a crystallographic axis, denoted by $\hat{\mathbf{z}} \equiv [001]$, which we in further call the out-of-plane axis. The remaining two crystallographic axes are denoted by $\hat{\mathbf{x}} \equiv [100]$ and $\hat{\mathbf{y}} \equiv [010]$, and are called in-plane. To simplify some formulas below, we additionally denote the in-plane components of the magnetic field as $\mathbf{b} \equiv (B_x, B_y)$ and denote the angle that $\mathbf{b}$ makes with $\hat{\mathbf{x}}$ as ϕ. With this notation, we set the unperturbed part of the three dimensional Hamiltonian as

$$H_0 = h_z + h_{2D}. \tag{3.3}$$

It defines the basis for the perturbative calculations below. The unperturbed part is chosen separable in the in-plane and out-of-plane coordinates. Next, we describe these two parts in further detail.

Unperturbed part defining the basis

The unperturbed Hamiltonian for the heterostructure growth direction, along the unit vector $\hat{\mathbf{z}}$, is[1]

$$h_z = -\partial_z \frac{\hbar^2}{2m(z)} \partial_z + \Theta(z) e E_{\mathrm{ext}} z + \Theta(-z) V_0, \tag{3.4}$$

[1]We stick here to the triangular heterostructure confinement in Eq. (3.4) and do not discuss in the main text, for the sake of brevity, other confinement types considered in Ref. 96. We give results for a symmetric confinement in App. 3.D.

where $\Theta(z)$ is the Heaviside step function, V_0 is the offset of the conduction bands of the constituent materials (we specify to $Al_xGa_{1-x}As$, referred to as material A, and GaAs, referred to as material B), $E_{\rm ext}$ is the interface electric field, and the position-dependent effective mass is

$$m(z) = \Theta(-z)m_A + \Theta(z)m_B. \tag{3.5}$$

The spectrum of h_z defines the subbands, denoted by $|\alpha\rangle$ with the corresponding energies E_α. We use Greek indexes for subbands, with the ground state belonging to subband $\alpha = 1$, while $\alpha = 2$ is the lowest excited subband, and so on.

Since the position dependence of the mass does not lead to spin-dependent effects, we approximate it by a constant within each subband, being $\langle m(z)\rangle\,\alpha$. The overline is defined as the average within the subband,

$$\langle O\rangle\,\alpha \equiv \langle\alpha|O|\alpha\rangle, \qquad \langle O\rangle\,\alpha\beta \equiv \langle\alpha|O|\beta\rangle, \tag{3.6}$$

and we also introduced the latter notation for further convenience. For the lowest subband, we set $\langle m(z)\rangle\,\alpha \approx m_B \equiv m$. In another words, even though we take the effects of mass inhomogeneity into account when constructing the basis, we do not include it among the considered perturbations.[2] With that, we define the nominal width l_z of the 2DEG by

$$eE_{\rm ext} \equiv \hbar^2/2ml_z^3, \tag{3.7}$$

that is, l_z is a quantity with the dimension of the length defined by the surface electric field and the effective mass.

The in-plane part of H_0, which defines the quantum dot, is taken with an anisotropic harmonic confinement

$$h_{2D} = \frac{\mathbf{p}^2}{2m} + \frac{\hbar^2}{2m}\left(\frac{x_d^2}{l_x^4} + \frac{y_d^2}{l_y^4}\right). \tag{3.8}$$

Here, the confinement potential is expressed in the dot coordinates defined by unit vectors $\hat{\mathbf{x}}_d$ and $\hat{\mathbf{y}}_d$, which are rotated with respect to the crystallographic axes $\hat{\mathbf{x}}$ and $\hat{\mathbf{y}}$ by an angle δ. The in-plane momentum contains the orbital effects due to the out-of-plane component of the magnetic field B_z,

$$\mathbf{p} = -i\hbar(\partial_x, \partial_y) + \frac{eB_z}{2}(-y, x). \tag{3.9}$$

[2]The corrections resulting from such terms are expected to be much smaller than the terms denoted g_z (see below), which are of similar origin and which are subdominant.

The spectrum of h_{2D} is equivalent to two independent linear harmonic oscillators with excitation energies E_x and E_y. For $B_z = 0$ the two energies are given by $E_{x/y} = \hbar^2/ml_{x/y}^2$, while the symmetric case $l_x = l_y$ corresponds to the well known Fock-Darwin spectrum. The general case of $B_z \neq 0$ and $l_x \neq l_y$ can be also solved straightforwardly. [113–115] We use Roman indexes for the eigenstates of h_{2D}, called in-plane (orbital) states. We denote their wave functions by $|i\rangle$ and the corresponding energies by E_i. The two harmonic oscillators quantum numbers corresponding to this state are denoted as $n_x^{(i)}$ and $n_y^{(i)}$.

The basis functions in the three dimensional space are defined as tensor product of the out-of-plane and in-plane terms, $|\alpha i\rangle \equiv |\alpha\rangle \otimes |i\rangle$. The corresponding energies are $E_{\alpha i} \equiv E_\alpha + E_i$. For further convenience, we define the aspect ratio η, as the ratio of the in-plane and subband energy spacings, $\eta = \min(E_x, E_y)/E_z$. For dots based on 2DEG, η is a small parameter. The geometry is summarized in Fig. 3.1.

Unperturbed Zeeman energy

At finite magnetic fields, the leading spin-dependent interaction in Eq. (3.1) is the Zeeman term

$$H_{\mathrm{Z}} = \frac{g(z)\mu_B}{2}\mathbf{B}\cdot\boldsymbol{\sigma}, \tag{3.10}$$

where the vector of Pauli matrices $\boldsymbol{\sigma} = (\sigma_x, \sigma_y, \sigma_z)$ is the electron spin operator, μ_B is the Bohr magneton, and the g-factor

$$g(z) = \Theta(-z)g_A + \Theta(z)g_B, \tag{3.11}$$

is z-coordinate dependent, similarly to the effective mass. Taking the expectation of Eq. (3.10) in a chosen subband, the spin structure of the basis state $|\alpha i\rangle$ is described by

$$H_Z^{(\alpha)} = \frac{\langle g(z)\rangle\, \alpha\mu_B}{2}\mathbf{B}\cdot\boldsymbol{\sigma}. \tag{3.12}$$

In Fig. 3.2, we plot the g-factor averaged in the lowest subband as a function of the 2DEG width. Decreasing the width, the g-factor value departs from the bulk GaAs value towards the $Al_xGa_{1-x}As$ value, due to the penetration of the wave function into the barrier material. This effect is well known [116] and allows for an electrically tunable g-factor through designed material composition. [117, 118]

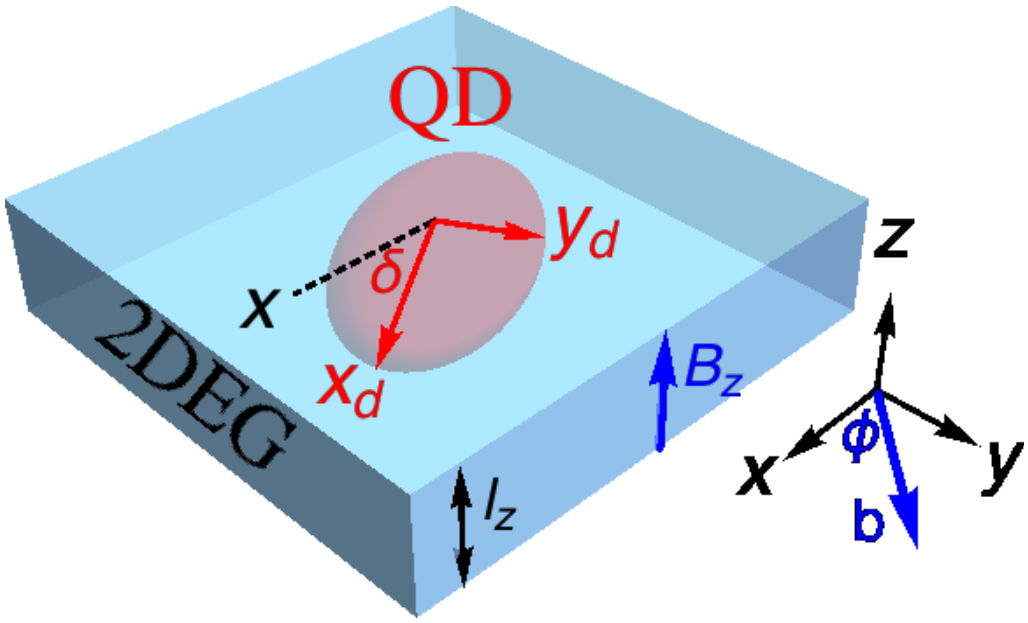

Figure 3.1: The setup schematic. The quantum dot (pink ellipsoid) is created by gates (not shown) in the two-dimensional electron gas (2DEG). The latter is a quasi-two-dimensional plane perpendicular to $\hat{\mathbf{z}} \equiv [100]$ axis and has a nominal width l_z. The axes of the quantum dot potential, $\hat{\mathbf{x}}_d$ and $\hat{\mathbf{y}}_{d'}$ are rotated by an angle δ with respect to the crystallographic axes $\hat{\mathbf{x}} \equiv [100]$ and $\hat{\mathbf{y}} \equiv [010]$. The magnetic field vector $\mathbf{B}$ has the out-of-plane component B_z and the in-plane component $\mathbf{b}$. The parameter ϕ denotes the angle of the $\mathbf{b}$ with the $\hat{\mathbf{x}}$ axis.

At this level of description, all states in a given subband have identical and isotropic g-factor. However, unlike for the mass dependence, we include difference between the exact and the averaged interaction,

$$H_z = H_Z - H_Z^{(\alpha)}, \tag{3.13}$$

among the perturbations considered below.

Spin-independent perturbation

The perturbation $H - H_0$ comprises the spin-independent and spin-dependent part. The first consists of the following terms

$$H'_B = \frac{e}{m}\mathbf{a}_{||} \cdot \mathbf{p} + \frac{e^2}{2m}\mathbf{a}_{||}^2 \equiv H'_1 + H'_2, \tag{3.14}$$

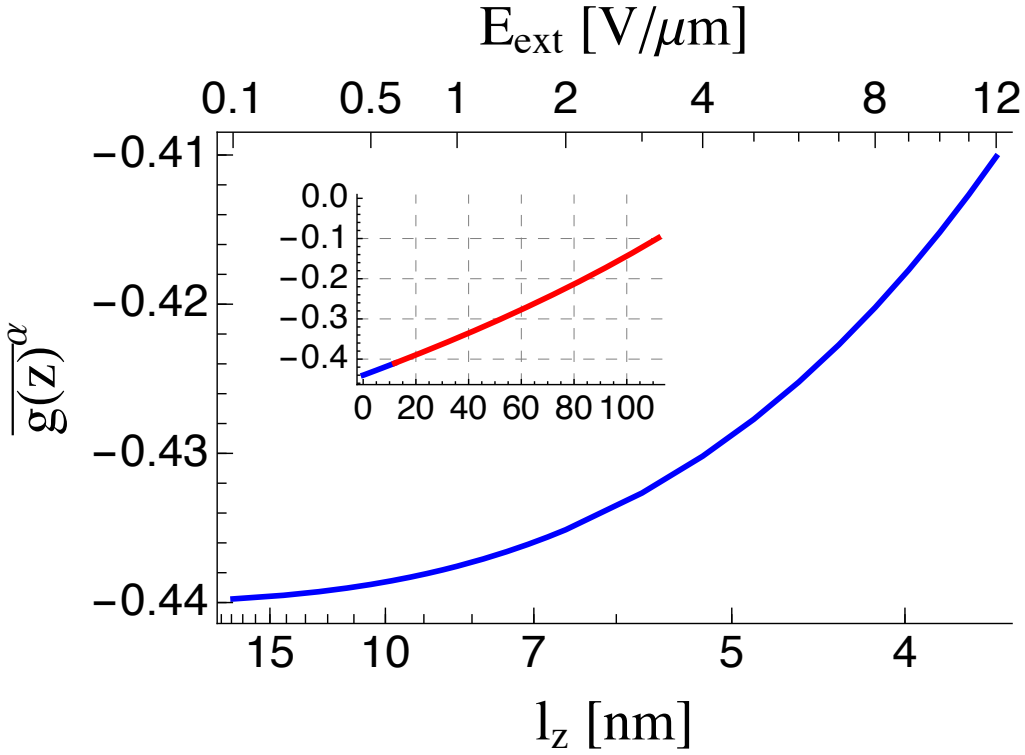

Figure 3.2: The lowest order approximation to the g-factor, showing the value of $\langle g(z)\rangle\,\alpha$ for the lowest subband, $\alpha = 1$. The lower and upper x-axis shows, respectively, the nominal width of the 2DEG, and the interface electric field. They are related by $eE_{\rm ext} = \hbar^2/2ml_z^3$. Inset: $\langle g(z)\rangle\,\alpha$ plotted for a larger range of the interface electric field $E_{\rm ext}$ (the inset x axis, given in V/μm). We show the electric field range for which at least one subband [a localized eigenstate of Eq. (3.4)] exists. The blue curve in the inset is the same as the blue curve of the main panel. We calculate the term numerically, solving for eigenstates of the triangular confinement potential with a finite conduction band offset $\delta E_c = E_c^{\rm A} - E_c^{\rm B} = 300$ meV. We also use $m_{\rm A} = 0.092\,m_e$, and $m_{\rm B} = 0.067\,m_e$ with m_e the free electron mass.

which appear due to the vector potential corresponding to the in-plane magnetic field

$$\mathbf{a}_{||} = (z - z_0)(B_y, -B_x). \tag{3.15}$$

In Ref. 96, we have shown what are the effects of this perturbation on the orbital structure of the quantum dot, that is, how the states $|\alpha i\rangle$ change. We found that the changes scale with the flux due to the in-plane field

$$\Phi = \frac{e}{\hbar}\sqrt{B_x^2 + B_y^2}\,\lambda_z^2, \tag{3.16}$$

serving as the small parameter of the perturbation theory. The flux depends on the effective 2DEG width, [95]

$$\lambda_z^4 = 2\sum_{\beta\neq\alpha}\frac{\hbar^2}{m}\frac{|z_{\alpha\beta}|^2}{E_\beta - E_\alpha}, \tag{3.17}$$

the behavior of which was analyzed in detail in Ref. 96.

Spin-dependent perturbations

In this article we are concerned with the effects of the in-plane magnetic field on the spin, rather than orbital, structure of the states. Such an analysis requires to expand the model by further spin-dependent interactions. To this end, we adopt the Ogg-McCombe Hamiltonian, [119,120] which can be derived by the method of invariants. Namely, it comprises terms allowed by the T_d symmetry group for the Γ_6 conduction band around its minimum at the wavevector $k = 0$, up to the fourth order in the components of the kinetic momentum operator $\mathbf{P}$. [121] We use the coefficients of the invariant expansion terms that were obtained in the fourth order perturbation of the $k \cdot p$ theory including 14 bands [23] (counting also degeneracies and spin; if each at $k = 0$ degenerate subspace is counted as one 'level', it is also called the 5L model [122]). This perturbative approach has been previously shown adequate in describing the conduction band g-factor in quantitative agreement with experiments. [123, 124] We now list the spin dependent terms of the Ogg-McCombe Hamiltonian.

We first take the 'standard' spin-orbit interactions. They comprise two terms, the bulk (Dresselhaus) term and the interface (Rashba) term. The former is

$$\begin{aligned} H_{\mathrm{D}} = \frac{\gamma_c}{2\hbar^3}\Big(&\sigma_x\left\{P_x, P_y^2 - P_z^2\right\} + \sigma_y\left\{P_y, P_z^2 - P_x^2\right\} \\ &+ \sigma_z\left\{P_z, P_x^2 - P_y^2\right\}\Big), \end{aligned} \tag{3.18}$$

where γ_c is a material constant, and the curly brackets denote the anti-commutator. The latter is

$$H_{\mathrm{R}} = \frac{\alpha_R(z)}{\hbar} \left(\sigma_y P_x - \sigma_x P_y\right), \tag{3.19}$$

where the pre-factor is well approximated by [125]

$$\alpha_R(z) = \alpha_0 e E_{\mathrm{ext}} + \beta_{BA}\delta(z), \tag{3.20}$$

with α_0, and β_{BA} being material constants, expressed through the band-structure parameters by formulas given in Ref. 96 [see Eqs. (C2) and (C6) therein].

The above spin-orbit terms are the leading spin-dependent corrections present at zero magnetic field. At finite magnetic fields, additional terms appear. As they do not have established names, we use the notation from Ref. 23. The first term is isotropic in both spin and momentum separately,

$$H_{43} = \frac{e\gamma_{43}}{\hbar^3}\mathbf{P}^2(\mathbf{B}\cdot\boldsymbol{\sigma}). \tag{3.21}$$

The next two terms are anisotropic,

$$\begin{aligned} H_{44} = \frac{e\gamma_{44}}{2\hbar^3}\Big[&\left(\{P_x, P_y\}\, B_y + \{P_x, P_z\}\, B_z\right)\sigma_x \\ &+ \left(\{P_y, P_z\}\, B_z + \{P_y, P_x\}\, B_x\right)\sigma_y \\ &+ \left(\{P_z, P_x\}\, B_x + \{P_z, P_y\}\, B_y\right)\sigma_z\Big], \end{aligned} \tag{3.22}$$

and

$$H_{45} = \frac{e\gamma_{45}}{\hbar^3}\Big(P_x^2 B_x\sigma_x + P_y^2 B_y\sigma_y + P_z^2 B_z\sigma_z\Big). \tag{3.23}$$

In the above, γ_{43}, γ_{44}, and γ_{45} are material dependent constants which are expressed through the bandstructure parameters in Refs. 23,126. The terms in Eqs. (3.21)–(3.23) have been essential to understand the dependence of the g-factor on the 2DEG width quantitatively, as well as to explain the anisotropy of the g-factor for magnetic fields in plane compared to magnetic fields out of plane. [123,124,127–129] Whereas for the first effect, H_{43} is the most important addition to the wave-function penetration effect shown in Fig. 3.2, H_{45} explains the in-plane versus the out-of-plane anisotropy upon noting that the heterostructure confinement makes the expectation value of the momentum operator components strongly different, $\langle P_z^2\rangle \gg \langle P_{x,y}^2\rangle$. The related light and heavy hole splitting by the

confinement can be seen as the physical origin of this type of conduction g-factor anisotropy. [124, 130]

In presence of both the electric and magnetic fields, an additional term arises, [131] which is not contained in the original Ogg-McCombe Hamiltonian. With an out-of-plane electric field and an in-plane magnetic field (the case to which we restrict ourselves below), this term is

$$H_{47} = \frac{e^2\gamma_{47}E(z)}{\hbar}(B_y\sigma_x + B_x\sigma_y), \tag{3.24}$$

where we use

$$E(z) = E_{\text{ext}} + \frac{\beta_{BA}}{e\alpha_0}\delta(z), \tag{3.25}$$

for the position dependent electric field, in analogy with Eq. (3.20).

We use the following material parameters for $A = \text{Al}_x\text{Ga}_{1-x}\text{As}$ with $x = 0.3$ and $B =$ GaAs. The effective masses [132] $m_A = 0.092m_e$, $m_B = 0.067m_e$, the g-factors $g_A = 0.46$, $g_B = -0.44$, [127] the spin-orbit strengths $\gamma_c = -10.6$ eVÅ^3, [133] $\alpha_0 = -5.15$ Å^2, [65] $\beta_{BA} = -1.22$ eVÅ^2. [125] For the remaining coefficients we take[3] $\gamma_{43} = 493$ eVÅ^4, $\gamma_{44} = -433$ eVÅ^4, $\gamma_{45} = 58$ eVÅ^4, [126] and $\gamma_{47} = -5.2$ Å^3. [109]

Let us make the following comments for completeness. First, we do not include terms quartic in momenta in the Ogg-McCombe Hamiltonian (anharmonic and warping terms) as they do not directly couple to spin. They would change the basis (both the subbands and the in-plane orbital states), which would lead to minor renormalization of the numerical factors (c and η below). Second, we do not consider the z-dependence of the $k \cdot p$ coefficients γ and take them as constants. On the one hand, these parameters do have different values in different materials, so that the penetration of the wave function into material A will renormalize them similarly to the g-factor and the effective mass. However, since the material values of these parameters have large uncertainties, their renormalization is of little practical consequence. Of interest here would be effects coming solely from their spatial dependence, which would be described by terms analogous to H_z in Eq. (3.13). As we find below, the

[3] There seems to be an inconsistency or a typo in Refs. 23, 126, 134. Namely, transforming a_{43}, a_{44}, and a_{45} in Table 2 of Ref. 126 into their dimensionful form, we get $\gamma_{43/4/5}$ as given here, in line with Ref. 109. However, using Table 3 of Ref. 23 directly with the band parameters in Ref. 134 we get $\gamma_{43} = 1080$ eVÅ^4, $\gamma_{44} = -676.9$ eVÅ^4, and $\gamma_{45} = 78.01$ eVÅ^4. We do not pursue the difference further, being of the order of one, which is not relevant for our purposes, and take the set with smaller values overall, as a conservative choice.

latter is negligible (it generates terms g_z in Fig. 3.5), which a posteriori justifies taking γ's as constant. Third, the one spin-orbit constant which we do not take constant in space is the Rashba coefficient. It is because it contains an explicit "interface" contribution, the δ-function term in Eq. (3.20). In principle, more interface contributions arise, corresponding to higher-order terms (in the electric field and in the momentum components) in the $k \cdot p$ theory. For example, Ref. 135 evaluates an additional interface term, similar in form to the Dresselhaus term. Nevertheless, the authors of that work find that unless the quantum well is very narrow, in GaAs the interface-Dresselhaus term is much smaller than the bulk-Dresselhaus term, justifying our choice again.[4]

The zeroth order spin-orbit interactions

Since our calculations rely on the expansion in the powers of the in-plane magnetic field, it is useful to introduce notation which explicitly reflects it. Namely, for the bulk Dresselhaus Hamiltonian, we denote as $H_{\mathrm{d,n}}$ the term proportional to $(b)^n$. It can be calculated using the following recursive formula,

$$H_{\mathrm{d,n}} = H_{\mathrm{D}}(\mathbf{b}=0), \qquad \text{if} \quad n=0, \tag{3.26a}$$

$$H_{\mathrm{d,n}} = \tfrac{1}{n}\big[\tfrac{e}{i\hbar}\mathbf{a}_{||}\cdot\mathbf{r}, H_{\mathrm{d,n-1}}\big], \qquad \text{if} \quad n>0. \tag{3.26b}$$

The highest non-zero term is with $n=3$. For the Rashba term, the same formulas can be used, though the terms beyond the linear one, $n=1$, are zero. The formula can be used also for the momentum dependent part of $H_{43,44,45}$, but we will not use such expressions explicitly. Rather, our main goal here is to connect to the standard notation for the spin-orbit terms without the orbital effects of the in-plane magnetic field. Namely, the lowest order spin-orbit interaction for subband α is obtained by taking the subband average of the **b**-independent terms,

$$H_{\mathrm{d}}^{(\alpha)} \equiv \langle H_{\mathrm{d,0}}\rangle\,\alpha, \quad H_{\mathrm{r}}^{(\alpha)} \equiv \langle H_{\mathrm{r,0}}\rangle\,\alpha. \tag{3.27}$$

[4]The interface terms are important in silicon conduction band, [136] where the bulk spin-orbit coupling is very weak. See the introduction of Ref. 135 for an overview of the relevant literature on the interface spin-orbit terms.

In this way, we get the standard expressions of the linear-in-momenta, and the cubic-in-momenta terms,

$$\begin{aligned} H_{\rm d}^{(\alpha)} =& \frac{\gamma_c}{\hbar^3}\langle p_z^2\rangle\,\alpha\Big(-\sigma_x p_x+\sigma_y p_y\Big) \\ &+\frac{\gamma_c}{2\hbar^3}\Big(\sigma_x\left\{p_x,p_y^2\right\}-\sigma_y\left\{p_y,p_x^2\right\}\Big), \end{aligned} \tag{3.28}$$

for the Dresselhaus term, and the linear-in-momenta terms,

$$H_{\rm r}^{(\alpha)}=\frac{\langle\alpha_R(z)\rangle\,\alpha}{\hbar}\Big(\sigma_y p_x-\sigma_x p_y\Big), \tag{3.29}$$

for the Rashba term.

3.3 The perturbation theory

We now explain our perturbation calculation. We aim at deriving spin-related corrections to the effective two-dimensional Hamiltonian for a given subband α, reflecting the influence of the orbital effects of the in-plane magnetic field. To this end, we treat H_0, Eq. (3.3), as the unperturbed part, and the rest as the perturbation,

$$H'=H'_B+H'_S. \tag{3.30}$$

It comprises the spin independent part, Eq. (3.14), and

$$H'_S=H_{\rm D}+H_{\rm R}+H_{\rm Z}+H_{43}+H_{44}+H_{45}+H_{47}, \tag{3.31}$$

the spin dependent terms.

Our results below list corrections which are linear in H'_S, and up to the third order in the in-plane magnetic field **b**. However, to explain the essence of the approach, let us first consider a simplified case. Namely, up to the second order in the perturbation H', the matrix elements of the effective Hamiltonian for the α-th subband are given by [22]

$$\begin{aligned} H_{ij}^{(\alpha)} =& \langle\alpha i|H'|\alpha j\rangle+\frac{1}{2}{\sum_{\beta k}}'\langle\alpha i|H'|\beta k\rangle \\ &\times\langle\beta k|H'|\alpha j\rangle\left(\frac{1}{E_{\alpha i}-E_{\beta k}}+\frac{1}{E_{\alpha j}-E_{\beta k}}\right). \end{aligned} \tag{3.32}$$

The summation is over all β and k except two pairs, $(\beta k)\neq(\alpha i)$, and $(\beta k)\neq(\alpha j)$. The formula is generalized to higher order and adjusted for our case in Appendix 3.B. For now, we look at terms arising in the simplified case described by the previous equation.

Two examples of the effective spin-orbit interaction

We now proceed with the evaluation of the effect on the spin beyond the lowest order term given in Eq. (3.12). We first present two examples, with which we motivate simplifications that we adopt in further steps to keep the results tractable. In both of these examples, we calculate the correction proportional to the first order of $H_{\mathrm{d},1}$, so that it is linear in γ_c, and linear in b. Let us first consider the $\beta = \alpha$ terms in Eq. (3.32) (we called such terms intra-subband in Ref. 96). We get

$$\begin{aligned} H_{\mathrm{d},1}^{(\alpha)}(\mathrm{intra}) &= \langle H_{\mathrm{d},1}\rangle\,\alpha - [\frac{e}{i\hbar}\left\langle \mathbf{a}_{||}\right\rangle \alpha\cdot\mathbf{r}, \langle H_{\mathrm{d},0}\rangle\,\alpha] \\ &= -\frac{e\gamma_c}{2\hbar^3}\left(B_x\sigma_y + B_y\sigma_x\right) \\ &\times \left(\langle\{z-z_0, p_z^2\}\rangle\,\alpha - \{\langle z-z_0\rangle\,\alpha, \langle p_z^2\rangle\,\alpha\}\right). \end{aligned} \tag{3.33}$$

This is the g-tensor correction derived in Ref. 137. We make two simplifications based on this expression. First, we specify to the gauge $z_0 = \langle z\rangle\,\alpha$ and denote $\Delta z = z - \langle z\rangle\,\alpha$. This choice makes the commutator term in Eq. (3.33) zero, as well as analogous commutators in higher order terms, since their role is only to assure the gauge invariance of the result.[5] Second, we regroup the Pauli matrices into the following combinations,

$$B_x\sigma_y + B_y\sigma_x = \sin(2\phi)\boldsymbol{\sigma}\cdot\mathbf{b} - \cos(2\phi)\boldsymbol{\sigma}\cdot(\mathbf{b}\times\hat{\mathbf{z}})\,. \tag{3.34}$$

The effective magnetic field defined by the second term is perpendicular to the effective magnetic field corresponding to the unperturbed Zeeman term, Eq. (3.12). As long as all the corrections are small (with respect to the unperturbed Zeeman energy), which is the case here, this off-diagonal term will only perturb the energy in the second order in its magnitude, which is beyond the perturbation order that we work in. The only consequence of the second term is a slight deflection (typically by less than 1°) of the quantization axis of the eigenstate spinor, an effect not of interest here.[6] We therefore neglect below such off-diagonal terms.

[5] The choice $z_0 = \langle z\rangle\,\alpha$ makes the subband-averaged vector potential zero, $\left\langle \mathbf{a}_{||}\right\rangle \alpha = 0$. Should the general expressions be of interest, it is simplest to generate them by Taylor expanding the following identity $H\left(\mathbf{p} + e\left\langle \mathbf{a}_{||}\right\rangle \alpha\right) = U^\dagger H(\mathbf{p})U$, with $U = \exp\left(\frac{i}{\hbar}e\left\langle \mathbf{a}_{||}\right\rangle \alpha\cdot\mathbf{r}\right)$. We note in passing that our gauge choice is different from the one adopted in, for example, Refs. 138, 139.

[6] The off-diagonal terms would be relevant for the electric-dipole spin-resonance, if the field generating them is driven. We leave the analysis of electric manipulations for future work.

Equation (3.33) is then reduced to a contribution to the g-factor

$$g_{\mathrm{d},0}^{(\alpha)}(\mathrm{intra}) = -\frac{\lambda_d}{\lambda_z} c_1^{(\alpha)} \sin(2\phi). \tag{3.35}$$

We parametrized the Dresselhaus constant by a length

$$\lambda_d = \frac{4\gamma_c m_e}{\hbar^2}, \tag{3.36}$$

with m_e the electron mass in vacuum, and

$$c_1^{(\alpha)} = \frac{\lambda_z}{2\hbar^2} \langle \{\Delta z, p_z^2\} \rangle \, \alpha, \tag{3.37}$$

is a dimensionless factor. Both are plotted in Fig. 3.4, and will be discussed below together with other terms of similar nature arising from other contributions.

Let us now take the $\beta \neq \alpha$ terms in Eq. (3.32), called also intersubband, corresponding again to the correction proportional to $H_{\mathrm{d},1}$. We get

$$\begin{aligned} H_{\mathrm{d},1}^{(\alpha)}(\mathrm{inter}) = \frac{e\gamma_c}{m\hbar^3} \sum_{\beta\neq\alpha} \frac{1}{E_\alpha - E_\beta} z_{\alpha\beta} \langle p_z^2 \rangle \, \beta\alpha \\ \times \left\{ (B_y p_x - B_x p_y), (-\sigma_x p_x + \sigma_y p_y) \right\}. \end{aligned} \tag{3.38}$$

Unlike in Eq. (3.33), the effective Hamiltonian now contains both spin and in-plane momentum operators, and is thus an effective spin-orbit interaction. It inherits the angular anisotropies from the original spin-orbit interactions, as well as the reference to the direction of the magnetic field. One should therefore expect anisotropies in, for example, the corresponding spin relaxation rates, [140] or the electric-dipole spin resonance amplitudes, [141] which are different to the anisotropies corresponding to the zeroth order spin-orbit fields. Even though the detailed analysis is beyond the scope here, we expect that this effect is minor. Namely, the most important attribute of these higher order 'spin-orbit' interactions is that, being generated by a magnetic field, they are not time-reversal symmetric. Unlike the zeroth order ones, they can therefore contribute to the g-factor in the lowest order, as we have seen already for Eq. (3.33). We therefore restrict ourselves to evaluating only this leading-order correction to the energy, by taking the expectation value in the unperturbed

orbital eigenstate i of the subband α. Equation (3.38) then reduces to a g-factor correction [taking again only the diagonal part, similar to the first term in Eq.(3.34)]

$$g_{\mathrm{d},0}^{(\alpha,i)}(\mathrm{inter}) = \frac{\lambda_d}{\lambda_z} c_2^{(\alpha)} \left(-\eta_+^{(i)} \sin(2\phi) + \eta_-^{(i)} \sin(2\delta) \right), \tag{3.39}$$

with c_2 another dimensionless constant (all these constants are listed in Appendix 3.C). The presence of the momentum operators in Eq. (3.38) makes this correction, unlike the one in Eq. (3.35), dependent on the in-plane size and orientation of the dot, through

$$\eta_\pm^{(i)} = \frac{\lambda_z^2}{2\hbar^2} \langle i | (\mathbf{p} \cdot \hat{\mathbf{x}}_d)^2 \pm (\mathbf{p} \cdot \hat{\mathbf{y}}_d)^2 | i \rangle. \tag{3.40}$$

Quite naturally, the part which does not refer to the dot orientation [the first term in the bracket in Eq. (3.39)] is proportional to the quantity characterizing the average size, η_+, while the part which refers to the dot orientation [the second term in the bracket in Eq. (3.39)] is proportional to the orbital asymmetry, η_-, of state i. For illustration, assuming zero out-of-plane magnetic field, and neglecting here the small effects of the effective mass renormalization, [96] these two parameters become

$$\eta_\pm^{(i)} = \frac{\lambda_z^2}{2l_x^2} \left(n_x^{(i)} + \frac{1}{2} \right) \pm \frac{\lambda_z^2}{2l_y^2} \left(n_y^{(i)} + \frac{1}{2} \right), \tag{3.41}$$

where the quantum numbers correspond to the state i, as defined below Eq. (3.9). Specifying further to the ground state, we got

$$\eta_\pm^{(\mathrm{ground})} = \lambda_z^2 (l_x^{-2} \pm l_y^{-2})/4. \tag{3.42}$$

For a dot which is circularly symmetric in the 2DEG plane, the basis can be always chosen such that $\eta_-^{(i)} = 0$ for all i. For a general dot, these two factors fulfill $\eta_- \lesssim \eta_+ \propto \eta$, so that they are small, of the order of the aspect ratio.

What is calculated: corrections to the g-factor

Based on the two presented examples, we now set our goals for the calculations, organization of the results, and their analysis. We aim at the

corrections to the g-factor[7] for a chosen subband α and orbital state i, obtained as the expectation value of the effective spin-orbit interaction generated by the in-plane field in this specific state. We restrict ourselves to the lowest order in H'_S, or, loosely denominating the prefactors in various terms of H'_S with a common name, in spin-orbit couplings. We choose the simplest gauge, $z_0 = \langle z \rangle \alpha$, and assume zero out-of-plane magnetic field for simplicity. Finally, we calculate the corrections up to the third order in the in-plane field, which is the highest order of the magnetic field appearing in H'_S, Eq. (3.31). Note that it requires to include also the third order perturbation terms, going beyond Eq. (3.32), as explained in Appendix 3.B.

Proceeding in this way, we are therefore neglecting terms being higher order in spin-orbit couplings (we estimate the largest such in Appendix 3.F and show that they are very small), terms of higher than the third order in the magnetic field, and terms admixing different in-plane orbitals. We calculate also the off-diagonal g-tensor components, but give them only in Appendix 3.A. In the derivations, we neglect the in-plane with respect to the subband excitation energies, which brings in the derived formulas an error of the order of η, the aspect ratio.

In the derived expressions, we are interested in several aspects. The most important question is, how large corrections to the g-factor should one expect upon applying an in-plane field. However, the simple magnitude comparison is not all, as the arising terms differ qualitatively in the dependence on: the magnetic field magnitude (either constant or growing quadratically with the in-plane field), the 2DEG width (both increase and decrease with λ_z are possible), the heterostructure symmetry (several terms do not arise in a symmetric quantum well), and the magnetic field orientation (the terms are either isotropic, or anisotropic but independent on the dot orientation, or dependent on it).

3.4 Results for g-factor corrections

We now list the obtained results. We first list the individual corrections, originating in the respective terms of the spin-orbit Hamiltonian. After that, we comment on the components of the corrections, which shed light

[7]The g-factor will be a function of the magnetic field and we understand it here as the ratio of the Zeeman energy and the magnetic field. Its value at $B = 0$ is to be understood as measured in the limit $B \to 0$, rather than directly at $B = 0$.

on the overall scales and tendencies. Finally, we present the total g-factor correction, a sum of all contributions.

Individual corrections

Here, we list the individual terms. The left hand side of each equation gives the g-factor correction $g_{x,n}$ where x denotes the origin of the term, with $x = \mathrm{d}$ for the Dresselhaus term, $x = \mathrm{r}$ for the Rashba term, $x = 43 - 47$ for the corresponding H_x, and $x = \mathrm{z}$ for H_z. The integer n denotes the power of the magnetic field on the right hand side. To simplify the notation, we omit the subband index α and orbital state index i. On the right hand side, the subband dependence enters through the dimensionless factors c, such as the one in Eq. (3.37), and the orbital-state dependence enters through the factors $\eta_{\pm}^{(i)}$, defined in Eq. (3.40).

The contributions from the Dresselhaus interaction are

$$g_{\mathrm{d},0} = \frac{\lambda_d}{\lambda_z}\Big((-c_1 - c_2\eta_+)\sin(2\phi) + c_2\eta_-\sin(2\delta)\Big), \tag{3.43a}$$

$$\begin{aligned} g_{\mathrm{d},2} = \frac{\lambda_d}{\lambda_z}\Phi^2\Big(&[c_3 - c_5 + (3c_4 - c_6 + c_{14})\eta_+]\sin(2\phi) \\ &-(3c_4 + c_{14})\eta_-\sin(2\delta) \\ &-c_4\eta_-\cos(2\phi)\sin(2\phi - 2\delta) \\ &+c_6\eta_-\sin(2\phi)\cos(2\phi - 2\delta) \\ &+c_1c_{16}\sin(2\phi)[\eta_+ - \eta_-\cos(2\phi - 2\delta)]\Big). \end{aligned} \tag{3.43b}$$

The contributions from the Rashba interaction are

$$g_{\mathrm{r},0} = -\xi_r\Big(c_{10} - 4c_{11}[\eta_+ - \eta_-\cos(2\phi - 2\delta)]\Big), \tag{3.44a}$$

$$\begin{aligned} g_{\mathrm{r},2} = &\frac{\lambda_z}{\lambda_r}\Phi^2\Big(c_4 + c_7[\eta_+ - \eta_-\cos(2\phi - 2\delta)]\Big) \\ &-\xi_r\Phi^2\Big(c_{12} + (3c_{13} + c_{15} - c_{10}c_{16}) \\ &\qquad\times[\eta_+ - \eta_-\cos(2\phi - 2\delta)]\Big). \end{aligned} \tag{3.44b}$$

The contributions from H_{43} are

$$g_{43,0} = \frac{\lambda_{43}^2}{\lambda_z^2}\Big(c_{17} + 2\eta_+\Big), \tag{3.45a}$$

$$g_{43,2} = \frac{\lambda_{43}^2}{\lambda_z^2}\Phi^2\Big(c_{18} + c_{20} + (4c_{19} + 3c_{21} - c_{17}c_{16}) \times[\eta_+ - \eta_- \cos(2\phi - 2\delta)]\Big). \tag{3.45b}$$

The contributions from H_{44} are

$$g_{44,0} = \frac{\lambda_{44}^2}{\lambda_z^2}\eta_- \sin(2\phi)\sin(2\delta), \tag{3.46a}$$

$$g_{44,2} = -\frac{\lambda_{44}^2}{\lambda_z^2}\Phi^2\Big(\frac{c_{18}}{4}[1 - \cos(4\phi)] + 2c_{19}\sin(2\phi) \times[\eta_+ \sin(2\phi) - \eta_- \sin(2\delta)]\Big). \tag{3.46b}$$

The contributions from H_{45} are

$$g_{45,0} = \frac{\lambda_{45}^2}{\lambda_z^2}[\eta_+ - \eta_- \cos(2\phi)\cos(2\delta)], \tag{3.47a}$$

$$g_{45,2} = \frac{\lambda_{45}^2}{\lambda_z^2}\Phi^2\Big(\frac{c_{18}}{4}[1 - \cos(4\phi)] + 2c_{19}\sin(2\phi) \times[\eta_+ \sin(2\phi) - \eta_- \sin(2\delta)]\Big). \tag{3.47b}$$

The contributions from H_{47} are

$$g_{47,0} = \Big(\frac{\lambda_{47}^3}{l_z^3} - \frac{\lambda'_{47}}{\lambda_z}c_{22}\Big)\sin(2\phi), \tag{3.48a}$$

$$g_{47,2} = -\frac{\lambda'_{47}}{\lambda_z}\Phi^2\sin(2\phi)\Big(c_{23} + (3c_{24} - c_{22}c_{16}) \times[\eta_+ - \eta_- \cos(2\phi - 2\delta)]\Big). \tag{3.48b}$$

Finally, the bulk g-factor inhomogeneity gives

$$g_{\mathrm{z},0} = 0, \tag{3.49a}$$

$$g_{\mathrm{z},2} = \Phi^2\Big(c_8 + c_9[\eta_+ - \eta_- \cos(2\phi - 2\delta)]\Big). \tag{3.49b}$$

For completeness, we also define the "penetration" correction,

$$g_{\mathrm{p}} = \langle g(z)\rangle\,\alpha = 1 - g_B, \tag{3.50}$$

for the deviation of the lowest-subband-averaged g-factor from the bulk value in material B (GaAs) due to the leakage of the wavefunction into material A. Rather than giving a formula, we calculate it numerically. It was already explained in Sec. 3.2 and plotted in Fig. 3.2: it is neither magnetic-field magnitude nor direction dependent.

Corrections' components

Let us first make some general comments on the above formulas. They split a g-factor correction to several dimensionless constituents, namely the strength, the magnetic field dependence, the numerical factors c and η, and the angular dependence. The strengths can be expressed as a certain power of the ratio of a length characteristic for each interaction, and, essentially, the 2DEG width.[8] The lengths are summarized in Tab. 3.1, and the corresponding strengths are plotted in Fig. 3.3. Concerning the magnetic field dependence, we obtained terms which are either constant, or grow quadratically with the in-plane flux. There are no terms linear in the magnetic field.[9] The constants c are not expected to display any systematic dependence, given the differences in their origins (see Appendix 3.C for explicit expressions). They are plotted on Fig. 3.4. The factors η give useful information about relative scales: for a nearly symmetrical dot, one can assume the hierarchy $1 \gg \eta_+ \gg |\eta_-|$. Finally, let us note the angular anisotropy. The terms which have cylindrical symmetry in the bulk, that is $x = \mathrm{r}, 43$, and z, result in corrections which are either isotropic, or anisotropic only due to the shape of the quantum dot. The latter terms depend on the relative orientation of the magnetic field with respect to the dot potential soft axis, through a common factor

$$\eta_+ - \eta_- \cos(2\phi - 2\delta). \tag{3.51}$$

[8] There is one exception: ξ_r is already dimensionless, so it is not useful to recast it as a length scale. Also, the scale dividing λ_{47} is l_z rather than λ_z. However, for the triangular confinement the difference between the latter two is completely negligible (see Tab. I in Ref. 96).

[9] Such linear-in-B terms were reported in theory [139, 142] and experiments. [100, 143–145] In all cases where the origin can be identified, it corresponds to the limit of Landau levels, meaning that the orbital effects of the magnetic field dominate the electrostatic confinement (either within the 2DEG plane, [142] or even perpendicular to it [139]). Such a limit corresponds to the magnetic field having beyond-perturbative influence on the excitation energies (whether in-plane or subband ones); that is, some of the excitation energies become linear in the field, $E_{\alpha i} - E_{\beta j} \sim |B|$. To put it in another way, there are no linear-in-B terms in the g-factor as long as the basis in which the pertubative calculation is done is time-reversal symmetric, which is the case here.

origin	definition	unit	d-full	scale	d-less	$\lvert\lambda\rvert$[Å]
Dress.	$4\gamma_c m_e/\hbar^2$	length^1	λ_d	λ_z	ξ_d	5.5
Rashba	$4\alpha_0 e E_{\text{ext}} m_e/\hbar^2$	length^{-1}	λ_r^{-1}	λ_z^{-1}	$\xi_{r'}$	1730
Rashba	$4\beta_{BA} m_e/\hbar^2$	length^0	ξ_r	1	ξ_r	-
43	$4\gamma_{43} m_e/\hbar^2$	length^2	λ_{43}^2	λ_z^2	ξ_3	16
44	$4\gamma_{44} m_e/\hbar^2$	length^2	λ_{44}^2	λ_z^2	ξ_4	15
45	$4\gamma_{45} m_e/\hbar^2$	length^2	λ_{45}^2	λ_z^2	ξ_5	5.5
47	$2\gamma_{47} m_e/m_B$	length^3	λ_{47}^3	l_z^3	ξ_7	5.3
47	$\xi_r\gamma_{47}/\alpha_0$	length^1	λ'_{47}	λ_z	$\xi_{7'}$	0.65

Table 3.1: Material constants parameterizing the g-factor corrections. Every λ has the dimension of length, every ξ is dimensionless. Column 1 gives the terms origin, column 2 its definition using $k \cdot p$ parameters and column 3 the unit of the expression in column 2. The units show that each of the dimensionfull parameters given in column 2 can be expressed as a length raised to some integer power. Such lengths are defined in column 4. They enter the g-factor corrections in a dimensionless form denoted by column 6, which is equal to the dimensionfull expression divided by the scale given in column 5. Finally, the last column gives the absolute value of the scale λ introduced in column 4. We exemplify these definitions taking the term "43": $\xi_3 = \lambda_{43}^2/\lambda_z^2 = 4\gamma_{43} m_e/\hbar^2\lambda_z^2$, and $|\lambda_{43}| \approx 16$Å. The length λ_r (row 2) depends on the interface electric field and the value $\lambda_r = 173$ nm is for $E_{\text{ext}} = 2.14$ V/μm. Finally, the parameter ξ_r (row 3) is dimensionless without introducing any scale and therefore 1 is used for the latter.

The remaining terms, which do not have cylindrical symmetry in the bulk, contain different factors. They relate separately to the crystallographic axes, or the quantum dot axes. We expect that these properties remain valid in higher orders of the perturbation theory.

Corrections' hierarchy

We now turn to quantitative analysis. First, from Table 3.1 and, more directly, from Fig. 3.3 , one can see that the correction strengths generally grow upon narrowing the 2DEG (the only exception is ξ_r which remains constant), but with different slopes. On the other hand, the magnetic flux also diminishes as the 2DEG is made narrower. Finally, the dependence

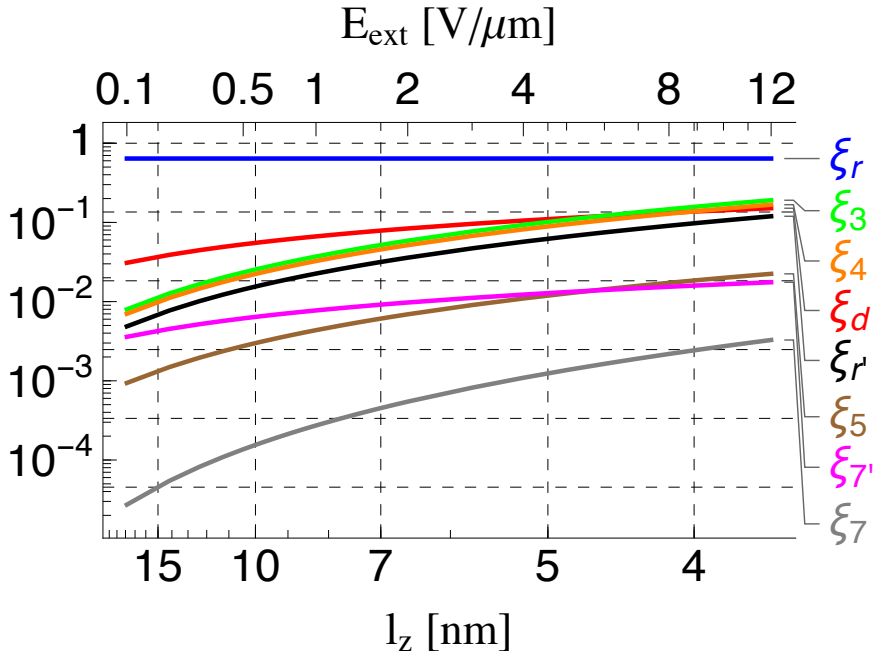

Figure 3.3: The scale parameters, defined in Tab. 3.1, as a function of the 2DEG width.

gets further involved due to a non-systematic behavior, and a wide scale variation, of the dimensionless constants c, see Fig. 3.4. Therefore, to nail down the importance hierarchy of the terms, it is easiest to look directly at the full terms, plotted in Fig. 3.5.

Figure 3.5(a)-(d) reveals the relative importance of the terms for a wide range of magnetic fields and 2DEG widths. We conclude that, concerning the g-factor corrections for the considered range of the interface fields, it is enough to include the Rashba, Dresselhaus, and H_{43} terms. For very narrow 2DEG, the effect of the wave-function penetration into the barrier might be sizable, but it does not have to be considered beyond the averaging performed in Eq. (3.12) and reflected in Fig. 3.2. Similarly, the influence of H_{45}, H_{47}, and, perhaps with an exception of very wide 2DEGs and high magnetic fields, also H_{44}, is negligible. Focusing on the relevant terms [close-ups are shown in Fig. 3.5(b) and (d)], Rashba and H_{43} dominate the Dresselhaus term the narrower the 2DEG becomes. Their magnetic field dependence is rather weak if the flux is small, $\Phi \ll 1$, as expected. Once the flux becomes of order one, the

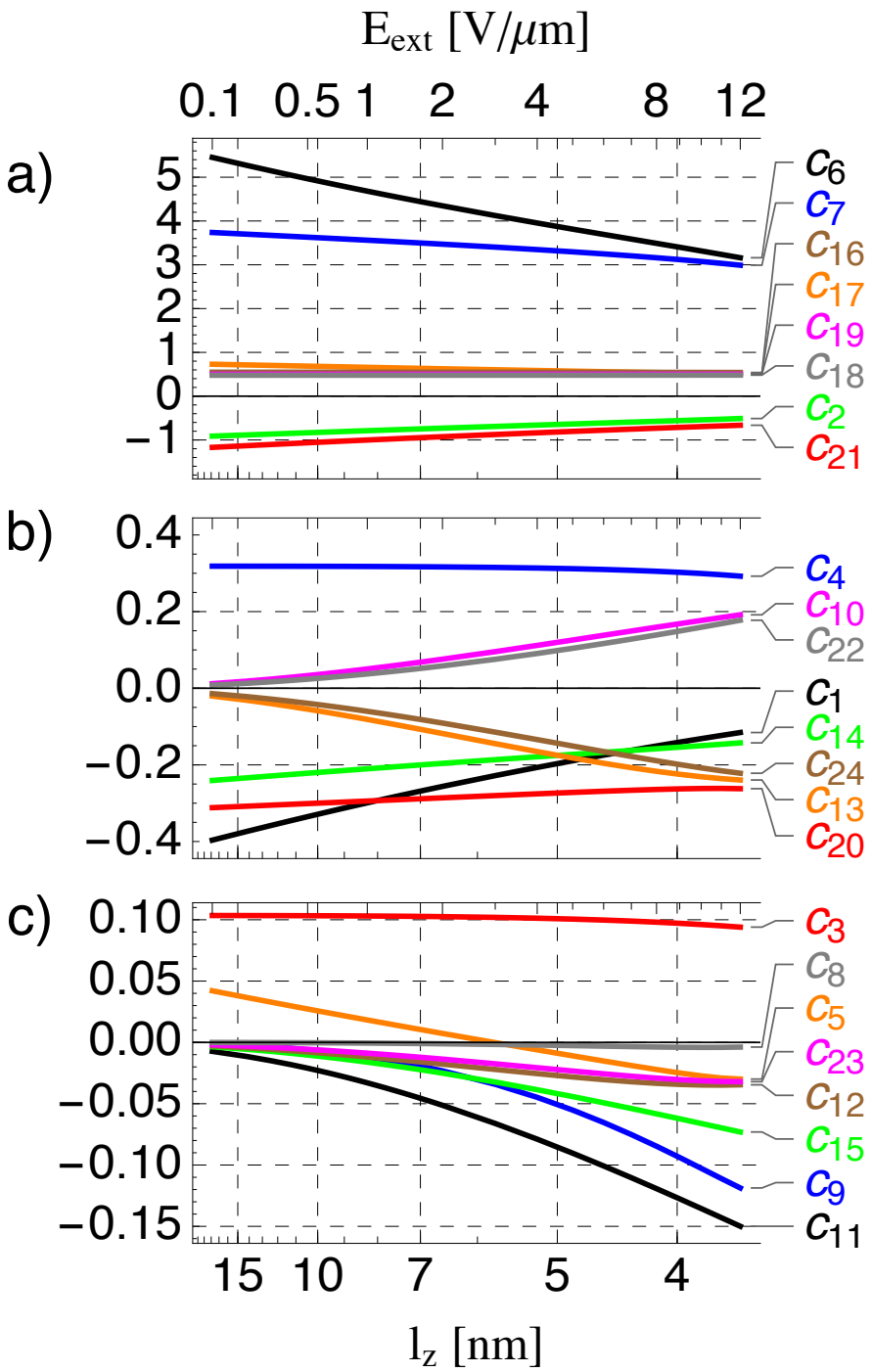

Figure 3.4: The dimensionless constants c_n in the lowest subband $\alpha = 1$. We find that for c's, the most natural parameter is the nominal width l_z, which is the parameter used for the lower x axis. The corresponding interface electric field is the upper x axis. The two are related by Eq. (3.7).

magnetic-field dependence is more pronounced, and the interference of the field-independent and the field-dependent terms can lead to sign reversals, exemplified as sharp dips visible on Fig. 3.5(a).

The angular dependence is shown on Fig. 3.5(e)-(f). The variation is dominated by the Dresselhaus term—even though this term is not largest in magnitude—with extrema related to the crystallographic axes (along [110] and $[1\bar{1}0]$). The same behavior was established for 2DEG in theory [137] and experiments. [145–147] The variation of the other two terms are much smaller, roughly by the factor η_-, with extrema related to the dot potential axes. As a result, the g-factor of a quantum dot should show a sizable directional dependence, with a minimum along $[1\bar{1}0]$ (assuming the sign of γ_c is negative).[10] In panel (e), the magnitude of the predicted directional variation is more than 10% of the full g-factor value. Since the overall angular variation mainly arises from the bulk-Dresselhaus term, its relative importance increases with the 2DEG width. Indeed, in Fig. 3.5(f) the angular dependence for a wider 2DEG indicates that the directional variation becomes comparable to the corrections due to the Rashba and H_{43} terms.

Next, we note the overall sign, looking at Fig. 3.5(e). Assuming that both $-\alpha_0$ and γ_{43} are indeed positive, both related corrections are positive, and diminish the magnitude of the negative g-factor in bulk GaAs. This is indeed the typical case seen in experiments. For the values assumed in panel (e), which correspond roughly to the interface parameters deduced from the experiment in Ref. 97, we would get the average g-factor of around -0.33. In that experiment, $|g| \approx 0.36$ was fitted from spectral data.

The sum of all contributions

We summarize the predictions of our formulas plotting the total g-factor [including the sum of all contributions in Eqs. (3.43)–(3.50)] in Fig. 3.6. For the parameters typical for the experiments in Refs. 97,98, the g-factor as a function of the magnetic field direction looks as in Fig. 3.6(a). The curve is characterized by three numbers, the average value, the magnitude of the variation, and the position of the maximum. We plot these

[10] The position of the minimum will be slightly shifted away from [110] by other terms that have extrema along different directions. As these additional variations are much smaller, the shift will be accordingly small, see Fig. 3.6.

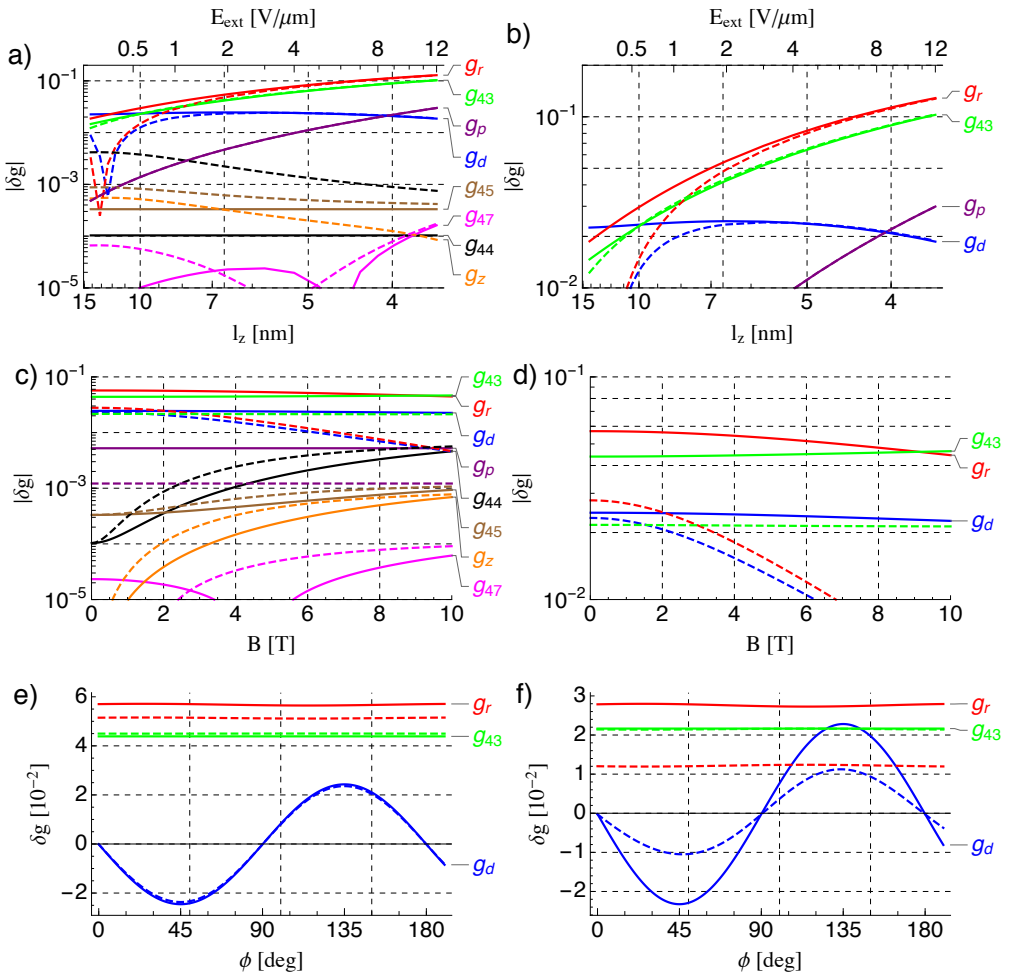

Figure 3.5: The corrections to the g-factor labeled according to the notation of Eqs. (3.43)–(3.50) for the ground state $\alpha = 1$, $n_x = 0$, and $n_y = 0$. The parameters used in this figure are $E_x = 2.34$ meV, $E_y = 2.61$ meV, $\delta = 25°$, $\phi = 45°$, unless stated otherwise (the adopted parameters were taken from fits to data measured in Ref. 98, see Fig. 7 in Ref. 96). (a-b) As a function of the 2DEG width, parametrized by the nominal width l_z (the lower x axis) and the interface electric field $E_{\rm ext}$ (the upper x axis). The solid (dashed) curves show corrections for $B = 0$ T ($B = 6$ T). Panel (b) shows the same as (a) apart from the y-axis range. (c-d) As a function of the magnetic field. The solid (dashed) curves show corrections for $E_{\rm ext} = 2.14$ V/μm ($E_{\rm ext} = 0.5$ V/μm). Panel (d) shows the same as (c) apart from the y-axis range. (e-f) As a function of the magnetic field orientation for (e) $E_{\rm ext} = 2.14$ V/μm (corresponding to $\lambda_z = 6.5$ nm) and (f) $E_{\rm ext} = 0.5$ V/μm (corresponding to $\lambda_z = 10.5$ nm). The solid (dashed) curves show corrections for $B = 0$ T ($B = 6$ T).

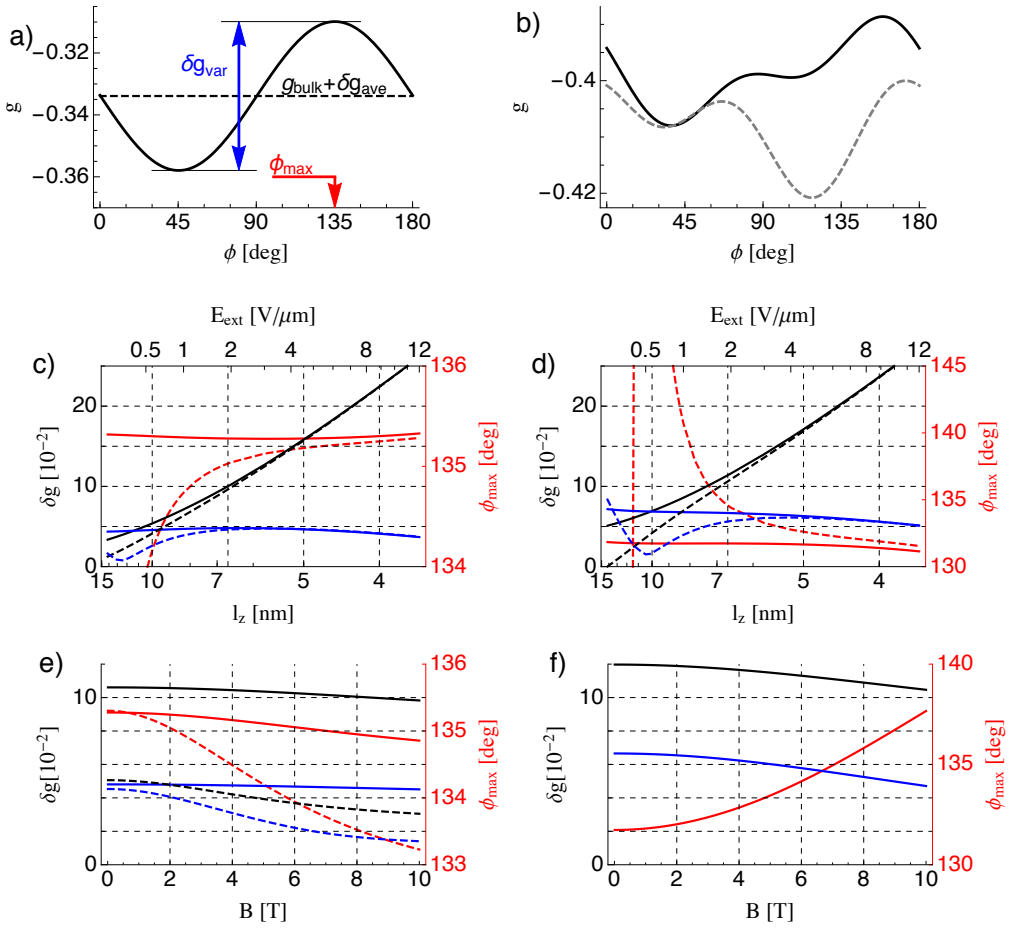

Figure 3.6: The total g-factor (or the g-factor correction) for the ground state $\alpha = 1$, $n_x = 0$, and $n_y = 0$ [panels (a), (c), and (e)] and the excited state $\alpha = 1$, $n_x = 1$, and $n_y = 0$ [panels (b), (d), and (f)] for $E_x = 2.34$ meV, $E_y = 2.61$ meV, $\delta = 25°$, and $E_{\rm ext} = 2.14$ V/μm (unless stated otherwise). (a) The ground state g-factor as a function of the magnetic field direction. (b) The excited state g-factor for $B = 5$ T (solid) and $B = 7$ T (dashed). Panel (a) represents the most typical case: the g-factor is a curve that is well described by its average over ϕ [black; we also subtract the constant -0.44 from it when plotting it in panels (c)-(f)], variation (blue; defined as the difference of the maximal and minimal value as a function of ϕ) and the magnetic-field orientation at the maximum (red). These three quantities are plotted in panels (c)-(f) in the corresponding colors. (c) As a function of the 2DEG width for $B = 0$ (solid) and $B = 6$ T (dashed). (d) Same as (c) for the excited state. (e) As a function of the magnetic field for $E_{\rm ext} = 2.14$ V/μm (solid) and $E_{\rm ext} = 0.5$ V/μm (dashed). (f) Same as (e) for the excited state.

quantities as functions of the 2DEG width and magnetic field in Fig. 3.6(c)-(f). Fig. 3.6(c) shows that the correction grows upon narrowing the 2DEG, in line with the behavior seen in Fig. 3.5(a). On the other hand, the variation magnitude is non-monotonic. It is biggest at around $l_z \approx 7$ nm, where it is almost half of the total correction. The position of the maximum deviates only slightly from $[1\bar{1}0]$, in line with Fig. 3.5(e). Panel (e) shows the effects of the in-plane magnetic field magnitude. Comparing the solid and dashed curves, one can confirm that the g-factor variations upon changing the magnetic field are bigger in wider 2DEG.

Finally, we notice that the g-factor corrections are more pronounced for excited states: the variation can become larger than the average correction sooner, while the position of the extrema can shift by larger angles. These facts are illustrated in Fig. 3.6(d),(f). Figure 3.6(f) shows the largest corrections are due to the same terms as for the ground state. However, the actual values of these contributions are appreciably different in their magnitude. One can therefore expect substantial differences in the g-factor renormalizations for different states of the quantum dot.

3.5 Conclusions

In this article, we have analyzed in-plane-magnetic-field induced terms in the Hamiltonian describing an electron confined in a quasi-two-dimensional quantum dot. We have focused on terms that can be grasped by restricting this Hamiltonian effectively only to the spin degree of freedom,

$$H_{\text{eff}}^{(\alpha,i)} = \frac{\mu_B}{2}\mathbf{B}\cdot\mathbf{g}_{\alpha,i}\cdot\boldsymbol{\sigma}, \tag{3.52}$$

meaning that the orbital degrees of freedom of the electron are fixed to be the subband α and the in-plane orbital i. The g-tensor grasps all the spin-related properties of the electron under such approximation. Apart from the explicit dependence on the quantum numbers α and i, the g-tensor depends on the heterostructure confinement shape and strength, and the magnetic field magnitude and orientation. We have analyzed these dependences in great details.

The various "spin-orbit" interactions of the bulk zinc-blende crystal are the microscopic origin of the g-tensor corrections that we calculated here. Importantly, these interactions go beyond the most usually considered Rashba and Dresselhaus terms. For example, the time-reversal-antisymmetric term denoted as H_{43}, see Eq. (3.21), dominates the g-tensor

corrections for typical parameters of GaAs/AlGaAs quantum dots. The "standard" Rashba spin-orbit term also gives a sizable contribution and the Dresselhaus term dominates the directional anisotropy (the variation of the g-tensor upon changing the magnetic field direction in the 2DEG plane).

We make specific predictions that can be tested experimentally, for example as for the directional anisotropies or magnetic field dependence of the Zeeman energy of the quantum dot with a single electron. Taking an alternative view, these predictions allow to extract several $k \cdot p$ constants from such measurements. Finally, our results have direct implications for electrical manipulation schemes of spin qubits and for understanding of their susceptibility to electrical noise.

3.A List of the off-diagonal effective Zeeman terms

Here, we list the off-diagonal g-tensor terms magnitude, up to the third order in the in-plane field. The terms arising from the Dresselhaus spin-orbit interaction are given by

$$g^{\perp}_{\mathrm{d},0} = \frac{\lambda_d}{\lambda_z}\Big(c_1\cos(2\phi) + c_2\eta_+\cos(2\phi) - c_2\eta_-\cos(2\delta)\Big), \tag{3.53a}$$

$$\begin{aligned} g^{\perp}_{\mathrm{d},2} = \frac{\lambda_d}{\lambda_z}\Phi^2\Big(&c_5\cos(2\phi) + (c_6 - c_{14})\eta_+\cos(2\phi) \\ &+c_{14}\eta_-\cos(2\delta) \\ &-c_4\eta_-\sin(2\phi)\sin(2\phi - 2\delta) \\ &-c_6\eta_-\cos(2\phi)\cos(2\phi - 2\delta) \\ &-c_1c_{16}\cos(2\phi)[\eta_+ - \eta_-\cos(2\phi - 2\delta)]\Big), \end{aligned} \tag{3.53b}$$

whereas $g^{\perp}_{\mathrm{d},1} = 0$. The Rashba spin-orbit interaction gives rise to

$$g^{\perp}_{\mathrm{r},0} = -4\xi_r c_{11}\eta_-\sin(2\phi - 2\delta), \tag{3.54a}$$

$$g^{\perp}_{\mathrm{r},2} = \xi_r\Phi^2 c_{15}\eta_-\sin(2\phi - 2\delta), \tag{3.54b}$$

with $g^{\perp}_{\mathrm{r},1}=0$. The H_{43} terms do not give the off-diagonal g-tensor components, $g^{\perp}_{43,0}=g^{\perp}_{43,1}=g^{\perp}_{43,2}=0$. The H_{44} terms lead to

$$g^{\perp}_{44,0} = -\frac{\lambda_{44}^2}{\lambda_z^2}\eta_- \cos(2\phi)\sin(2\delta), \tag{3.55a}$$

$$g^{\perp}_{44,2} = \frac{\lambda_{44}^2}{\lambda_z^2}\Phi^2\Big(\frac{c_{18}}{4}\sin(4\phi)+2c_{19}\cos(2\phi) \times[\eta_+\sin(2\phi)-\eta_-\sin(2\delta)]\Big), \tag{3.55b}$$

with $g^{\perp}_{44,1}=0$. The terms from H_{45} give

$$g^{\perp}_{45,0} = \frac{\lambda_{45}^2}{\lambda_z^2}\eta_- \sin(2\phi)\cos(2\delta), \tag{3.56a}$$

$$g^{\perp}_{45,2} = -\frac{\lambda_{45}^2}{\lambda_z^2}\Phi^2\Big(\frac{c_{18}}{4}\sin(4\phi)+2c_{19}\sin(2\phi) \times[\eta_+\cos(2\phi)-\eta_-\cos(2\delta)]\Big), \tag{3.56b}$$

with $g^{\perp}_{45,1}=0$. The H_{47} term gives rise to,

$$g^{\perp}_{47,0} = \Big(-\frac{\lambda_{47}^3}{l_z^3}+\frac{\lambda'_{47}}{\lambda_z}c_{22}\Big)\cos(2\phi), \tag{3.57a}$$

$$g^{\perp}_{47,2} = \frac{\lambda'_{47}}{\lambda_z}\Phi^2\cos(2\phi)\Big(c_{23}+(3c_{24}-c_{22}c_{16}) \times[\eta_+-\eta_-\cos(2\phi-2\delta)]\Big), \tag{3.57b}$$

with $g^{\perp}_{47,1}=0$. The interface terms do not lead to off-diagonal terms, $g^{\perp}_{\mathrm{z},0}=g^{\perp}_{\mathrm{z},1}=g^{\perp}_{\mathrm{z},2}=0$.

3.B Derivation of the spin-dependent corrections

Here, we derive Eqs. (3.43)–(3.49) and Eqs. (3.53)–(3.57). To this end, we aim at computing the corrections to the spin Hamiltonian for a chosen orbital state $|\alpha i\rangle$, applying up to the third order perturbation theory (see Footnote 1 in Ref. 96 for a comment on the name of this method). The perturbation comprises the spin and the magnetic-field originated terms,

$$H' = H'_S + H'_B. \tag{3.58}$$

In the following, we first derive the third-order perturbative formula, adjusting the general theory for our case. Then, we derive the Zeeman-term corrections, taking the constituents of H'_S one by one. Before that, we note that, as explained in the discussion around Eq. (3.34), we will express these corrections as a sum of two terms,

$$\delta V_{||}\sigma_{||} + \delta V_{\perp}\sigma_{\perp}. \tag{3.59a}$$

It means that we separate the components parallel and perpendicular to the in-plane magnetic field,

$$\sigma_{||} \equiv \boldsymbol{\sigma}\cdot\mathbf{B}/|\mathbf{B}| = \sigma_x\cos\phi + \sigma_y\sin\phi, \tag{3.59b}$$

$$\sigma_{\perp} \equiv \boldsymbol{\sigma}\cdot(\mathbf{B}/|\mathbf{B}|\times\hat{\mathbf{z}}) = \sigma_x\sin\phi - \sigma_y\cos\phi. \tag{3.59c}$$

The parallel components $\delta V_{||}$, leading to Eqs. (3.43)–(3.49), change the Zeeman energy. The perpendicular components $\delta V_{\perp}$, leading to Eqs. (3.53)–(3.57), change (slightly rotate) the eigenspinor direction.

Perturbation theory up to the third order

In the subspace defined by subband α and orbital state i, the effective Hamiltonian up to the third order is

$$\begin{aligned}
&\langle\alpha i|H'|\alpha i\rangle + \sum_{\beta j\neq\alpha i}\frac{\langle\alpha i|H'|\beta j\rangle\langle\beta j|H'|\alpha i\rangle}{E_{\alpha i}-E_{\beta j}}\\
&+\sum_{\beta j\neq\alpha i}\sum_{\gamma k\neq\alpha i}\frac{\langle\alpha i|H'|\beta j\rangle\langle\beta j|H'|\gamma k\rangle\langle\gamma k|H'|\alpha i\rangle}{(E_{\alpha i}-E_{\beta j})(E_{\alpha i}-E_{\gamma k})}\\
&-\frac{1}{2}\sum_{\beta j\neq\alpha i}\frac{\{\langle\alpha i|H'|\beta j\rangle\langle\beta j|H'|\alpha i\rangle,\langle\alpha i|H'|\alpha i\rangle\}}{(E_{\alpha i}-E_{\beta j})^2}.
\end{aligned} \tag{3.60}$$

The first two terms correspond to Eq. (3.32) for $i = j$, the next two terms arise in the third order. In deriving this expression from the general formulas (see, for example, page 135 in Ref. 22), we used that since the Zeeman term is included among the perturbations in H', the basis state energies are spin independent. It allows us to suppress the spin indexes, by treating the matrix elements such as $\langle\alpha i|H'|\beta j\rangle$ as operators in the spin space (that is, two-by-two matrices). This is why the anticommutator in the last term is necessary.

We now simplify the third order terms further, by restricting to contributions which are linear in the spin-dependent perturbation H'_{S} and

up to the third order in the magnetic field. From $\langle \alpha i|H_1'|\alpha i\rangle = 0$ and $\langle \alpha i|H_2'|\beta j\rangle = 0$ if $j \neq i$, it follows that the last line in Eq. (3.60) can be written as

$$\begin{aligned} &-\sum_{\beta\neq\alpha} \frac{\langle i|\left\langle H_1'\right\rangle \alpha\beta \left\langle H_1'\right\rangle \beta\alpha|i\rangle}{(E_\alpha - E_\beta)^2} \langle \alpha i|H_{\rm S}'|\alpha i\rangle \\ &-\sum_{\beta\neq\alpha} \frac{\langle i|(\left\langle H_1'\right\rangle \alpha\beta \left\langle H_{\rm S}'\right\rangle \beta\alpha + \left\langle H_{\rm S}'\right\rangle \alpha\beta \left\langle H_1'\right\rangle \beta\alpha)|i\rangle}{(E_\alpha - E_\beta)^2} \langle \alpha i|H_2'|\alpha i\rangle. \end{aligned} \tag{3.61}$$

The anticommutator is not needed anymore since H_1' and H_2' do not contain Pauli matrices. The first line of the above formula can be considered as a correction to the intra-subband contribution, such as the one in Eq. (3.33). The second line results in corrections with the same angular dependence as the inter-subband contributions, such as the one in Eq. (3.38). As a result, we split the effective Hamiltonian to the following two contributions,

$$\begin{aligned} \delta H_{\rm s}^{(1)} =& \langle i|\left\langle H_{\rm S}'\right\rangle \alpha|i\rangle(1-\xi_{\alpha i}) + \langle i|[\langle H_{\rm S}'\rangle \alpha, \frac{e}{i\hbar}\left\langle \mathbf{a}_{||}\right\rangle \alpha\cdot\mathbf{r}]|i\rangle \\ &+ \frac{1}{2}\langle i|[[\langle H_{\rm S}'\rangle \alpha, \frac{e}{i\hbar}\left\langle \mathbf{a}_{||}\right\rangle \alpha\cdot\mathbf{r}], \frac{e}{i\hbar}\left\langle \mathbf{a}_{||}\right\rangle \alpha\cdot\mathbf{r}]|i\rangle, \end{aligned} \tag{3.62a}$$

obtained with the help of the identity $H_1' = (e/i\hbar)\left[\mathbf{a}_{||}\cdot\mathbf{r}, h_{2D}\right]$, and

$$\begin{aligned} \delta H_{\rm s}^{(2)} =& \sum_{\beta\neq\alpha}\sum_{k} \frac{\langle i|\left\langle H'\right\rangle \alpha\beta|k\rangle\langle k|\left\langle H'\right\rangle \beta\alpha|i\rangle}{E_\alpha - E_\beta} \\ &+ \sum_{\beta\neq\alpha}\sum_{\gamma\neq\alpha}\sum_{j,k} \frac{\langle i|\left\langle H'\right\rangle \alpha\beta|j\rangle\langle j|\left\langle H'\right\rangle \beta\gamma|k\rangle\langle k|\left\langle H'\right\rangle \gamma\alpha|i\rangle}{(E_\alpha - E_\beta)(E_\alpha - E_\gamma)} \\ &- \left\langle H_2'\right\rangle \alpha \sum_{\beta\neq\alpha} \frac{\langle i|\left\langle H_1'\right\rangle \alpha\beta \left\langle H_{\rm S}'\right\rangle \beta\alpha + \left\langle H_{\rm S}'\right\rangle \alpha\beta \left\langle H_1'\right\rangle \beta\alpha|i\rangle}{(E_\alpha - E_\beta)^2}. \end{aligned} \tag{3.62b}$$

The correction factor in the first is

$$\xi_{\alpha i} = \sum_{\beta\neq\alpha} \frac{\langle i|\left\langle H_1'\right\rangle \alpha\beta \left\langle H_1'\right\rangle \beta\alpha|i\rangle}{(E_\alpha - E_\beta)^2} \tag{3.63}$$

and we neglected the orbital with respect to the subband excitation energies in the second.

Obviously, the role of the commutators is to assure gauge invariance. After demonstrating it in Section 3.B, we put $z_0 = \langle z\rangle \alpha$, upon which the

commutators disappear since $\langle \mathbf{a}_{||} \rangle \, \alpha = 0$. We denote the gauge invariant form of the expectation value in Eq. (3.62a), without the correction $\xi_{\alpha i}$, as the intra-subband contribution. The terms from Eq. (3.62b) are denoted as the inter-subband terms. The correction term $\xi_{\alpha i}$ is calculated separately, in Appendix 3.C. Finally, we note that $\delta H_{\rm s}$ is still an operator in the spin space, and it can be written in the form of Eq. (3.59a). In the following subsections, we compute the intra-subband and inter-subband contributions for every constituent of H'_S separately. From here on, we assume zero out-of-plane component of the magnetic field, $B_z = 0$.

Before continuing, we note that the fourth-order perturbation theory will generate additional corrections that are cubic in the in-plane magnetic flux. These corrections contain one matrix element from the zero-field Rashba or Dresselhaus (i.e. $H_{\rm d,0}$) spin-orbit interactions, and three matrix elements from H'_1. However, since each of these matrix elements comprises an in-plane momentum operator p_x or p_y, the corrections will be of order $O(\Phi^3) \times O(\eta_\pm^2)$. Since this is of the same or higher order of magnitude as the errors introduced when we neglect the in-plane orbital splitting in deriving Eq. (3.62b), in what follows we also neglect the fourth-order terms.

Dresselhaus intra-subband terms

We first take Eq. (3.62a) with the Dresselhaus term as the perturbation, $H'_{\rm S} \to H_{\rm D}$, and sort the resulting terms according to the power of the magnetic field. The term independent on the in-plane magnetic field is the unperturbed Dresselhaus interaction, Eq. (3.28). The linear term is

$$\begin{aligned} \delta H^{(1)}_{\rm d,1} =& \frac{e\gamma_c}{2\hbar^3} \big(\langle \{ \sigma_y a_{||,y} - \sigma_x a_{||,x}, p_z^2 \} \rangle \, \alpha \\ & - \{ \sigma_y \langle a_{||,y} \rangle \, \alpha - \sigma_x \langle a_{||,x} \rangle \, \alpha, \langle p_z^2 \rangle \, \alpha \} \big) \, , \end{aligned} \tag{3.64}$$

where we have used that the expectation values of the momentum operators, p_x, and p_y, are zero in any localized state, including state i. Using Eq. (3.15) further gives

$$\begin{aligned} \delta H^{(1)}_{\rm d,1} =& - \frac{e\gamma_c}{2\hbar^3} \left(B_x \sigma_y + B_y \sigma_x \right) \\ & \times \left(\langle \{ z - z_0, p_z^2 \} \rangle \, \alpha - \{ \langle z - z_0 \rangle \, \alpha, \langle p_z^2 \rangle \, \alpha \} \right) . \end{aligned} \tag{3.65}$$

The gauge choice $z_0 = \langle z \rangle \, \alpha$ simplifies it further,

$$\delta H^{(1)}_{\rm d,1} = - \frac{e\gamma_c}{2\hbar^3} \left(B_x \sigma_y + B_y \sigma_x \right) \langle \{ \Delta z, p_z^2 \} \rangle \, \alpha, \tag{3.66}$$

with $\Delta z = z - \langle z \rangle \alpha$. The components of $\delta \mathbf{V}$ follow as

$$\delta V^{(1)}_{\mathrm{d},1,||} = -\frac{e\gamma_c}{2\hbar^3} B \sin(2\phi) \langle \{\Delta z, p_z^2\} \rangle \alpha, \tag{3.67a}$$

$$\delta V^{(1)}_{\mathrm{d},1,\perp} = \frac{e\gamma_c}{2\hbar^3} B \cos(2\phi) \langle \{\Delta z, p_z^2\} \rangle \alpha, \tag{3.67b}$$

which correspond to the terms proportional to c_1 in Eqs. (3.43a), and (3.53a), respectively.

The term quadratic in the in-plane field is

$$\begin{aligned} \delta H^{(1)}_{\mathrm{d},2} =& \frac{e^2\gamma_c}{2\hbar^3} \sigma_z \left(B_y^2 - B_x^2\right) \left(\langle \{\Delta z^2, p_z\} \rangle \alpha + \right. \\ & \left. + \{ (\langle \Delta z \rangle \alpha)^2, \langle p_z \rangle \alpha \} - 2 \langle \{\Delta z, p_z\} \rangle \alpha \langle \Delta z \rangle \alpha \right), \end{aligned} \tag{3.68}$$

which is again simplified taking $z_0 = \langle z \rangle \alpha$ to

$$\delta H^{(1)}_{\mathrm{d},2} = \frac{e^2\gamma_c}{2\hbar^3} \sigma_z \left(B_y^2 - B_x^2\right) \langle \{\Delta z^2, p_z\} \rangle \alpha. \tag{3.69}$$

Since the last term is an expectation value of a purely imaginary operator, this correction is zero.

Following the same procedure, the cubic term gives

$$\delta V^{(1)}_{\mathrm{d},3,||} = \frac{e^3\gamma_c}{2\hbar^3} B^3 \sin(2\phi) \langle \Delta z^3 \rangle \alpha, \tag{3.70a}$$

$$\delta V^{(1)}_{\mathrm{d},3,\perp} = 0, \tag{3.70b}$$

corresponding to the term c_3 in Eq. (3.43b).

Dresselhaus inter-subband terms

We now consider the Dresselhaus term in Eq. (3.62b), again sorting the terms according to powers of the in-plane magnetic field. We first compute the first line of Eq. (3.62b), arising from the second-order perturbation theory. We calculate the terms involving H_1', and H_2' separately, starting with the former. The linear term, coming from $H_{\mathrm{d},0}$, Eq. (3.26), in the first term of Eq. (3.62b) gives

$$\begin{aligned} \delta H^{(2)}_{\mathrm{d},1} =& \frac{e\gamma_c}{m\hbar^3} \sum_{\beta \neq \alpha} \frac{1}{E_\alpha - E_\beta} z_{\alpha\beta} \langle p_z^2 \rangle \beta\alpha \\ & \times \langle i | \left[(B_y p_x - B_x p_y) (-\sigma_x p_x + \sigma_y p_y) \right. \\ & \left. + (-\sigma_x p_x + \sigma_y p_y) (B_y p_x - B_x p_y) \right] | i \rangle, \end{aligned} \tag{3.71}$$

where we used the fact that $z_{\alpha\beta}$ and $\langle p_z^2\rangle\,\beta\alpha$ are real. Using the reflection symmetry of the in-plane confinement along the axes $\hat{\mathbf{x}}_d$ and $\hat{\mathbf{y}}_d$, we arrive at

$$\begin{aligned}\delta H^{(2)}_{\mathrm{d},1} =& \frac{2e\gamma_c}{m\hbar^3}\sum_{\beta\neq\alpha}\frac{1}{E_\alpha - E_\beta} z_{\alpha\beta}\,\langle p_z^2\rangle\,\beta\alpha \\ &\times\left\{\sigma_x\left[-\left\langle p_+^2\right\rangle iB_y + \left\langle p_-^2\right\rangle i\,(B_x\sin 2\delta - B_y\cos 2\delta)\right]\right. \\ &\left.+\sigma_y\left[-\left\langle p_+^2\right\rangle iB_x + \left\langle p_-^2\right\rangle i\,(B_x\cos 2\delta + B_y\sin 2\delta)\right]\right\},\end{aligned} \tag{3.72}$$

where we put

$$\left\langle p_\pm^2\right\rangle i \equiv \frac{1}{2}\langle i|(\mathbf{p}\cdot\hat{\mathbf{x}}_d)^2 \pm (\mathbf{p}\cdot\hat{\mathbf{y}}_d)^2|i\rangle. \tag{3.73}$$

The components of $\delta\mathbf{V}$ then follow as

$$\begin{aligned}\delta V^{(2)}_{\mathrm{d},1,||} &= \frac{2e\gamma_c}{m\hbar^3}B\sum_{\beta\neq\alpha}\frac{1}{E_\alpha - E_\beta} z_{\alpha\beta}\,\langle p_z^2\rangle\,\beta\alpha \\ &\quad\times\left[-\left\langle p_+^2\right\rangle i\sin(2\phi) + \left\langle p_-^2\right\rangle i\sin(2\delta)\right], \qquad (3.74a)\\ \delta V^{(2)}_{\mathrm{d},1,\perp} &= \frac{2e\gamma_c}{m\hbar^3}B\sum_{\beta\neq\alpha}\frac{1}{E_\alpha - E_\beta} z_{\alpha\beta}\,\langle p_z^2\rangle\,\beta\alpha \\ &\quad\times\left[\left\langle p_+^2\right\rangle i\cos(2\phi) - \left\langle p_-^2\right\rangle i\cos(2\delta)\right], \qquad (3.74b)\end{aligned}$$

which gives the c_2 terms in Eqs. (3.43a) and (3.53a).

The quadratic term, coming from $H_{\mathrm{d},1}$, is

$$\begin{aligned}\delta H^{(2)}_{\mathrm{d},2} \approx& \frac{e^2\gamma_c}{m\hbar^3}\sum_{\beta\neq\alpha}\left[\frac{z_{\alpha\beta}\,\langle\{\Delta z, p_z\}\rangle\,\beta\alpha}{E_\alpha - E_\beta} + \frac{\langle\{\Delta z, p_z\}\rangle\,\alpha\beta z_{\beta\alpha}}{E_\alpha - E_\beta}\right] \\ &\times\sigma_z\left[\left\langle p_+^2\right\rangle i\left(B_y^2 - B_x^2\right) + \left\langle p_-^2\right\rangle i\left(B_x^2 + B_y^2\right)\cos 2\delta\right].\end{aligned} \tag{3.75}$$

Since $z_{\alpha\beta}$ is real, the summand is proportional to $\langle\{\Delta z, p_z\}\rangle\,\alpha\beta + \langle\{\Delta z, p_z\}\rangle\,\beta\alpha$, which vanishes for any (α,β). As a consequence, these terms do not contribute to $\delta\mathbf{V}$.

The cubic term, involving $H_{\mathrm{d},2}$, is

$$\begin{aligned}\delta H^{(2)}_{\mathrm{d},3} \approx& \frac{2e^3\gamma_c}{m\hbar^3}\sum_{\beta\neq\alpha}\frac{1}{E_\alpha - E_\beta} z_{\alpha\beta}\,\langle\Delta z^2\rangle\,\beta\alpha \\ &\times\left(\sigma_x B_x\left\{3B_xB_y\left\langle p_+^2\right\rangle i\right.\right. \\ &\qquad\left.\left.-\left\langle p_-^2\right\rangle i\left[(B_x^2 + 2B_y^2)\sin 2\delta + B_xB_y\cos 2\delta\right]\right\}\right. \\ &\left.+\sigma_y B_y\left\{3B_xB_y\left\langle p_+^2\right\rangle i\right.\right. \\ &\qquad\left.\left.-\left\langle p_-^2\right\rangle i\left[(2B_x^2 + B_y^2)\sin 2\delta - B_xB_y\cos 2\delta\right]\right\}\right),\end{aligned} \tag{3.76}$$

with $\langle \Delta z^2 \rangle \, \alpha\beta$ being real. The components of $\delta \mathbf{V}$ follow as

$$\begin{aligned} \delta V^{(2)}_{\mathrm{d},3,||} &= \frac{e^3\gamma_c}{m\hbar^3} B^3 \sum_{\beta\neq\alpha} \frac{1}{E_\alpha - E_\beta} z_{\alpha\beta} \langle \Delta z^2 \rangle \, \beta\alpha \\ &\quad \times \left[3 \left\langle p_+^2 \right\rangle i \sin(2\phi) - 3 \left\langle p_-^2 \right\rangle i \sin(2\delta) \right. \\ &\quad \left. - \left\langle p_-^2 \right\rangle i \cos(2\phi) \sin(2\phi - 2\delta) \right], \end{aligned} \tag{3.77a}$$

$$\begin{aligned} \delta V^{(2)}_{\mathrm{d},3,\perp} &= -\frac{e^3\gamma_c}{m\hbar^3} B^3 \sum_{\beta\neq\alpha} \frac{1}{E_\alpha - E_\beta} z_{\alpha\beta} \langle \Delta z^2 \rangle \, \beta\alpha \\ &\quad \times \left\langle p_-^2 \right\rangle i \sin(2\phi) \sin(2\phi - 2\delta), \end{aligned} \tag{3.77b}$$

giving the c_4 terms in Eqs. (3.43b) and (3.53b).

We now turn to terms involving H_2' in the first line of Eq. (3.62b). The quadratic terms in the in-plane field, arising from H_2' and $H_{\mathrm{d},0}$, vanish after taking the expectation value with respect to $|i\rangle$, as they contain odd number of in-plane momentum operators. The cubic terms, due to H_2' and $H_{\mathrm{d},1}$, lead to the following components of $\delta \mathbf{V}$,

$$\delta V^{(2)}_{\mathrm{d},\mathrm{H}_2,||} = -\frac{e^3\gamma_c}{2m\hbar^3} B^3 \sum_{\beta\neq\alpha} \frac{\langle \Delta z^2 \rangle \, \alpha\beta \, \langle \{\Delta z, p_z^2\} \rangle \, \beta\alpha}{E_\alpha - E_\beta} \sin(2\phi), \tag{3.78a}$$

$$\delta V^{(2)}_{\mathrm{d},\mathrm{H}_2,\perp} = \frac{e^3\gamma_c}{2m\hbar^3} B^3 \sum_{\beta\neq\alpha} \frac{\langle \Delta z^2 \rangle \, \alpha\beta \, \langle \{\Delta z, p_z^2\} \rangle \, \beta\alpha}{E_\alpha - E_\beta} \cos(2\phi), \tag{3.78b}$$

where we used that $\langle \{\Delta z, p_z^2\} \rangle \, \alpha\beta$ is real. They correspond to c_5 in Eqs. (3.43b) and (3.53b).

Finally, we consider the second and third lines of Eq. (3.62b), arising

from the third-order perturbation theory. They result in

$$\begin{aligned}\delta V^{(2)}_{\mathrm{d,3rd},||} &= \frac{3\gamma_c e^3}{m^2\hbar^3}B^3\sum_{\beta\neq\alpha}\sum_{\gamma\neq\alpha}\frac{z_{\alpha\beta}z_{\beta\gamma}\left\langle\Delta z p_z^2\right\rangle\gamma\alpha}{(E_\alpha-E_\beta)(E_\alpha-E_\gamma)}\\ &\times\sin(2\phi)\left[-\left\langle p_+^2\right\rangle i+\left\langle p_-^2\right\rangle i\cos(2\phi-2\delta)\right]\\ &-\frac{\gamma_c e^3}{m^2\hbar^3}B^3\sum_{\beta\neq\alpha}\frac{z_{\alpha\beta}\left\langle p_z^2\right\rangle\beta\alpha\left\langle\Delta z^2\right\rangle\alpha}{(E_\alpha-E_\beta)^2}\\ &\times\left[-\left\langle p_+^2\right\rangle i\sin(2\phi)+\left\langle p_-^2\right\rangle i\sin(2\delta)\right], \qquad (3.79a)\\ \delta V^{(2)}_{\mathrm{d,3rd},\perp} &= \frac{3\gamma_c e^3}{m^2\hbar^3}B^3\sum_{\beta\neq\alpha}\sum_{\gamma\neq\alpha}\frac{z_{\alpha\beta}z_{\beta\gamma}\left\langle\Delta z p_z^2\right\rangle\gamma\alpha}{(E_\alpha-E_\beta)(E_\alpha-E_\gamma)}\\ &\times\cos(2\phi)\left[\left\langle p_+^2\right\rangle i-\left\langle p_-^2\right\rangle i\cos(2\phi-2\delta)\right]\\ &-\frac{\gamma_c e^3}{m^2\hbar^3}B^3\sum_{\beta\neq\alpha}\frac{z_{\alpha\beta}\left\langle p_z^2\right\rangle\beta\alpha\left\langle\Delta z^2\right\rangle\alpha}{(E_\alpha-E_\beta)^2}\\ &\times\left[\left\langle p_+^2\right\rangle i\cos(2\phi)-\left\langle p_-^2\right\rangle i\cos(2\delta)\right], \qquad (3.79b)\end{aligned}$$

giving the c_6 and c_{14} terms in Eqs. (3.43b) and (3.53b).

Rashba terms

Comparing to the previous section, now the calculations are simpler as the Rashba interaction, Eq. (3.19), contains only terms of zeroth and first order in the in-plane magnetic field. The intra-subband contribution from the former is the unperturbed Rashba interaction, Eq. (3.29). The latter gives

$$\delta H^{(1)}_{\mathrm{r},1}=-\frac{\beta_{BA}e}{\hbar}(\sigma_x B_x+\sigma_y B_y)\left\langle\delta(z)\right\rangle\alpha\left\langle z\right\rangle\alpha, \qquad (3.80)$$

which directly gives the c_{10} term in Eq. (3.44a). Analogous terms, originating in the interface-generated spin-orbit interactions (see Footnote 4), were derived in Ref. 148 and used to fit experiments in Si in Refs. 149 and 150.

We now move on to the inter-subband contributions. The term linear in the in-plane magnetic field is

$$\begin{aligned}\delta H^{(2)}_{\mathrm{r},1} &= -\frac{4e\beta_{BA}}{m\hbar}\sum_{\beta\neq\alpha}\frac{z_{\alpha\beta}\left\langle\delta(z)\right\rangle\beta\alpha}{E_\alpha-E_\beta}\\ &\times\left\{\sigma_x\left[-\left\langle p_+^2\right\rangle iB_x+\left\langle p_-^2\right\rangle i\left(B_x\cos 2\delta+B_y\sin 2\delta\right)\right]\right.\\ &\left.+\sigma_y\left[-\left\langle p_+^2\right\rangle iB_y-\left\langle p_-^2\right\rangle i\left(B_y\cos 2\delta-B_x\sin 2\delta\right)\right]\right\},\end{aligned} \qquad (3.81)$$

and gives the following components of $\delta\mathbf{V}$,

$$\begin{aligned}\delta V^{(2)}_{\mathrm{r},1,||} =& -\frac{4e\beta_{BA}}{m\hbar}B\sum_{\beta\neq\alpha}\frac{z_{\alpha\beta}\left\langle\delta(z)\right\rangle\beta\alpha}{E_\alpha-E_\beta}\\ &\times\left[-\left\langle p_+^2\right\rangle i+\left\langle p_-^2\right\rangle i\cos(2\phi-2\delta)\right],\end{aligned} \tag{3.82}$$

$$\delta V^{(2)}_{\mathrm{r},1,\perp} = -\frac{4e\beta_{BA}}{m\hbar}B\sum_{\beta\neq\alpha}\frac{z_{\alpha\beta}\left\langle\delta(z)\right\rangle\beta\alpha}{E_\alpha-E_\beta}\left\langle p_-^2\right\rangle i\sin(2\phi-2\delta). \tag{3.83}$$

These are the c_{11} terms in Eqs. (3.44a) and (3.54a).

Similarly as before, the quadratic term is zero. For the cubic term, considering H_2' in the first line of Eq. (3.62b) gives

$$\begin{aligned}\delta H^{(2)}_{\mathrm{r,H_2}} &= \frac{e^3}{m\hbar}(\sigma_xB_x+\sigma_yB_y)(B_x^2+B_y^2)\\ &\times\sum_{\beta\neq\alpha}\frac{\langle\Delta z^2\rangle\,\alpha\beta}{E_\alpha-E_\beta}\left(\alpha_0eE_{\mathrm{ext}}z_{\beta\alpha}-\beta_{BA}\left\langle z\right\rangle\alpha\left\langle\delta(z)\right\rangle\beta\alpha\right),\end{aligned} \tag{3.84}$$

and generates therefore only a parallel component of $\delta\mathbf{V}$, as the c_4, and c_{12} terms in Eq. (3.44b). Finally, the second and third lines of Eq. (3.62b) result in

$$\begin{aligned}\delta V^{(2)}_{\mathrm{r,3rd},||} &= -\frac{3e^3B^3}{m^2\hbar}\sum_{\beta\neq\alpha}\sum_{\gamma\neq\alpha}\frac{z_{\alpha\beta}z_{\beta\gamma}}{(E_\alpha-E_\beta)(E_\alpha-E_\gamma)}\\ &\times\left[\beta_{BA}\left\langle\delta(z)\right\rangle\gamma\alpha\left\langle z\right\rangle\alpha-\alpha_0eE_{\mathrm{ext}}z_{\gamma\alpha}\right]\\ &\times\left[\left\langle p_+^2\right\rangle i-\left\langle p_-^2\right\rangle i\cos(2\phi-2\delta)\right]\\ &-\frac{\beta_{BA}e^3B^3}{m^2\hbar}\sum_{\beta\neq\alpha}\frac{z_{\alpha\beta}\left\langle\delta(z)\right\rangle\beta\alpha\left\langle\Delta z^2\right\rangle\alpha}{(E_\alpha-E_\beta)^2}\\ &\times\left[\left\langle p_+^2\right\rangle i-\left\langle p_-^2\right\rangle i\cos(2\phi-2\delta)\right],\end{aligned} \tag{3.85}$$

$$\begin{aligned}\delta V^{(2)}_{\mathrm{r,3rd},\perp} &= \frac{\beta_{BA}e^3B^3}{m^2\hbar}\sum_{\beta\neq\alpha}\frac{z_{\alpha\beta}\left\langle\delta(z)\right\rangle\beta\alpha\left\langle\Delta z^2\right\rangle\alpha}{(E_\alpha-E_\beta)^2}\\ &\times\left\langle p_-^2\right\rangle i\sin(2\phi-2\delta),\end{aligned} \tag{3.86}$$

entering Eq. (3.44b) and Eq. (3.54b) as c_7, c_{13}, and c_{15}.

Terms from H_{43}, H_{44}, H_{45}, and H_{47}

The contributions from the in-plane field-induced spin-orbit interaction (H_{43}, H_{44}, H_{45} and H_{47}') can be computed similarly. Since these terms

are directly proportional to the magnetic field, it is more convenient to express them using the Bohr magneton. Namely, we can start with the following expressions,

$$H_{43} = \frac{\lambda_{43}^2}{2\hbar^2}\mu_B(\mathbf{B}\cdot\boldsymbol{\sigma})\Big(P_x^2+P_y^2+P_z^2\Big), \tag{3.87}$$

$$H_{44} = \frac{\lambda_{44}^2}{4\hbar^2}\mu_B\Big[\left(\{P_x,P_y\}\,B_y\sigma_x+\{P_y,P_x\}\,B_x\sigma_y\right) + \left(\{P_z,P_x\}\,B_x+\{P_z,P_y\}\,B_y\right)\sigma_z\Big], \tag{3.88}$$

$$H_{45} = \frac{\lambda_{45}^2}{2\hbar^2}\mu_B\Big(P_x^2B_x\sigma_x+P_y^2B_y\sigma_y\Big). \tag{3.89}$$

For the purpose of this subsection, we also define the following part of H_{47},

$$H'_{47} = -\frac{\lambda'_{47}}{2}\delta(z)\mu_B(B_y\sigma_x+B_x\sigma_y). \tag{3.90}$$

The remaining part of H_{47} is already in the form of a g-tensor,

$$H_{47}-H'_{47} = \frac{e^2\gamma_{47}E_{\text{ext}}}{\hbar}(B_y\sigma_x+B_x\sigma_y), \tag{3.91}$$

and therefore does not need a perturbative treatment: it directly gives the term proportional to λ_{47}^3 in Eq. (3.48a).

The intra-subband contributions from H_{43} can be put as

$$\delta H_{43}^{(1)} = \frac{\lambda_{43}^2}{2\hbar^2}\mu_B(\mathbf{B}\cdot\boldsymbol{\sigma})\Big(\left\langle p_z^2\right\rangle\alpha+2\left\langle p_+^2\right\rangle i+e^2B^2\left\langle\Delta z^2\right\rangle\alpha\Big), \tag{3.92}$$

what gives the c_{17} and η_+ terms in Eq. (3.45a), and c_{17} and c_{18} terms in Eq. (3.45b). The inter-subband contributions from H_{43} can be written as

$$\begin{aligned}\delta H_{43}^{(2)} =& \frac{2e^2B^2\lambda_{43}^2}{m\hbar^2}\mu_B(\mathbf{B}\cdot\boldsymbol{\sigma})\Big(\left\langle p_+^2\right\rangle i-\left\langle p_-^2\right\rangle i\cos(2\phi-2\delta)\Big)\\ &\times\sum_{\beta\neq\alpha}\frac{|z_{\alpha\beta}|^2}{E_\alpha-E_\beta}\\ &+\frac{e^2B^2\lambda_{43}^2}{2m\hbar^2}\mu_B(\mathbf{B}\cdot\boldsymbol{\sigma})\sum_{\beta\neq\alpha}\frac{\left\langle\Delta z^2\right\rangle\alpha\beta\left\langle p_z^2\right\rangle\beta\alpha}{E_\alpha-E_\beta}\\ &+\frac{3e^2B^2\lambda_{43}^2}{2m^2\hbar^2}\mu_B(\mathbf{B}\cdot\boldsymbol{\sigma})\Big(\left\langle p_+^2\right\rangle i-\left\langle p_-^2\right\rangle i\cos(2\phi-2\delta)\Big)\\ &\times\sum_{\beta\neq\alpha}\sum_{\gamma\neq\alpha}\frac{z_{\alpha\beta}z_{\beta\gamma}\left\langle p_z^2\right\rangle\gamma\alpha}{(E_\alpha-E_\beta)(E_\alpha-E_\gamma)},\end{aligned} \tag{3.93}$$

what gives the c_{19}, c_{20}, and c_{21} terms in Eq. (3.45b).

The intra-subband contributions from H_{44} can be written as

$$\begin{aligned}\delta H_{44}^{(1)} =&\frac{\lambda_{44}^2}{2\hbar^2}\mu_B\Big(B_y\sigma_x + B_x\sigma_y\Big)\left\langle p_-^2\right\rangle i\sin(2\delta)\\ &-\frac{\lambda_{44}^2 e^2B^2}{4\hbar^2}\mu_B\Big(B_y\sigma_x + B_x\sigma_y\Big)\left\langle\Delta z^2\right\rangle\alpha\sin(2\phi),\end{aligned}\tag{3.94}$$

what gives the η_- term in Eq. (3.46a) and (3.55a), and c_{18} term in Eq. (3.46b) and (3.55b). The inter-subband contributions from H_{44} can be written as

$$\begin{aligned}\delta H_{44}^{(2)} =&-\frac{\lambda_{44}^2 e^2B^2}{m\hbar^2}\mu_B\Big(B_y\sigma_x + B_x\sigma_y\Big)\sum_{\beta\neq\alpha}\frac{|z_{\alpha\beta}|^2}{E_\alpha - E_\beta}\\ &\times\Big[\left\langle p_+^2\right\rangle i\sin(2\phi) - \left\langle p_-^2\right\rangle i\sin(2\delta)\Big],\end{aligned}\tag{3.95}$$

what gives the c_{19} term in Eq. (3.46b) and Eq. (3.55b).

The intra-subband contributions from H_{45} can be written as

$$\begin{aligned}\delta H_{45}^{(1)} =&\frac{\lambda_{45}^2}{2\hbar^2}\mu_B\Big\{B_x\sigma_x\Big[\left\langle p_+^2\right\rangle i + \left\langle p_-^2\right\rangle i\cos(2\delta)\Big]\\ &+B_y\sigma_y\Big[\left\langle p_+^2\right\rangle i - \left\langle p_-^2\right\rangle i\cos(2\delta)\Big]\Big\}\\ &+\frac{\lambda_{45}^2 e^2B^2}{4\hbar^2}\mu_B\Big(B_y\sigma_x + B_x\sigma_y\Big)\left\langle\Delta z^2\right\rangle\alpha\sin(2\phi),\end{aligned}\tag{3.96}$$

where the first two lines contribute as η_+ and η_- terms in Eqs. (3.47a) and (3.56a). These terms were derived in Ref. 148. The last line enters in Eqs. (3.47b) and (3.56b) as c_{18} terms. The inter-subband contribution from H_{45} is given by

$$\begin{aligned}\delta H_{45}^{(2)} =&\frac{\lambda_{45}^2 e^2B^2}{m\hbar^2}\mu_B\sum_{\beta\neq\alpha}\frac{|z_{\alpha\beta}|^2}{E_\alpha - E_\beta}\sin(2\phi)\\ &\times\Big\{\sigma_x\Big[\left\langle p_+^2\right\rangle iB_y - \left\langle p_-^2\right\rangle iB\sin(2\delta-\phi)\Big]\\ &+\sigma_y\Big[\left\langle p_+^2\right\rangle iB_x - \left\langle p_-^2\right\rangle iB\cos(2\delta-\phi)\Big]\Big\},\end{aligned}\tag{3.97}$$

what gives the c_{19} term in Eq. (3.47b) and Eq. (3.56b).

The intra-subband contributions from H'_{47} can be written as

$$\delta H_{47}^{(1)} = -\lambda'_{47}\left\langle\delta(z)\right\rangle\alpha\frac{\mu_B}{2}\Big(B_y\sigma_x + B_x\sigma_y\Big),\tag{3.98}$$

giving c_{22} in Eqs. (3.48a) and (3.57a). The inter-subband contribution from H'_{47} is given by

$$\begin{aligned}\delta H^{(2)}_{47} = &- \frac{\lambda'_{47} e^2 B^2}{2m} \mu_B (B_y \sigma_x + B_x \sigma_y) \left\{ \sum_{\beta\neq\alpha} \frac{\langle \Delta z^2 \rangle \, \alpha\beta \, \langle \delta(z) \rangle \, \beta\alpha}{E_\alpha - E_\beta} \right. \\ &+ 3 \sum_{\beta\neq\alpha} \sum_{\gamma\neq\alpha} \frac{z_{\alpha\beta} z_{\beta\gamma} \, \langle \delta(z) \rangle \, \gamma\alpha}{(E_\alpha - E_\beta)(E_\alpha - E_\gamma)} \\ &\left. \times \left[\left\langle p_+^2 \right\rangle i - \left\langle p_-^2 \right\rangle i \cos(2\phi - 2\delta) \right] \right\} ,\end{aligned} \tag{3.99}$$

what gives the c_{23} and c_{24} terms in Eqs. (3.48b) and (3.57b).

Terms from the inhomogeneous g-factor

The important difference to the previously considered spin-orbit interactions, the Zeeman term $H_{\rm Z}$ depends only on the z coordinate, and is therefore diagonal in the in-plane orbital sector of the basis, $\langle i|H_Z|j\rangle \propto \delta_{ij}$. This, first of all, makes the intra-subband contributions zero. For the same reason, in the inter-subband terms, H'_1 does not contribute in the first line of Eq. (3.62b). The only contribution, due to H'_2, reads

$$\delta V^{(2)}_{\mathrm{z,H_2,||}} = \frac{\mu_B e^2}{2m} B^3 \sum_{\beta\neq\alpha} \frac{\langle g(z) \rangle \, \alpha\beta \, \langle \Delta z^2 \rangle \, \beta\alpha}{E_\alpha - E_\beta}, \tag{3.100}$$

what gives the c_8 term in Eq. (3.49b). In the third order of the perturbation theory, the second line of Eq. (3.62b), we get

$$\begin{aligned}\delta V^{(2)}_{\mathrm{z,3rd,||}} = &\frac{3e^2}{m^2} B^3 \sum_{\beta\neq\alpha} \sum_{\gamma\neq\alpha} \frac{z_{\alpha\beta} z_{\beta\gamma} \, \langle g(z) \rangle \, \gamma\alpha}{(E_\alpha - E_\beta)(E_\alpha - E_\gamma)} \\ &\times \left[\left\langle p_+^2 \right\rangle i - \left\langle p_-^2 \right\rangle i \cos(2\phi - 2\delta) \right] ,\end{aligned} \tag{3.101}$$

what gives the c_9 term in Eq. (3.49b).

3.C List of all dimensionless constants

In this appendix, we give the correlation factor $\xi_{\alpha i}$ in Eq. (3.63), and list all dimensionless constants introduced in Eqs. (3.43)–(3.49). The correlation factor is given by

$$\xi_{\alpha i} = \Phi^2 c_{16} \left[\eta_+ - \eta_- \cos(2\phi - 2\delta) \right] , \tag{3.102}$$

which enters Eqs. (3.43b), (3.44b), (3.45b), (3.48b), (3.53b), and (3.57b) as c_{16}. The dimensionless constants c_i are given by

$$c_1 = \frac{\lambda_z}{2\hbar^2} \langle \{\Delta z, p_z^2\} \rangle \, \alpha, \tag{3.103a}$$

$$c_2 = \frac{2}{m\lambda_z} \sum_{\beta \neq \alpha} \frac{z_{\alpha\beta} \langle p_z^2 \rangle \, \beta\alpha}{E_\alpha - E_\beta}, \tag{3.103b}$$

$$c_3 = \frac{1}{2\lambda_z^3} \langle \Delta z^3 \rangle \, \alpha, \tag{3.103c}$$

$$c_4 = \frac{\hbar^2}{m\lambda_z^5} \sum_{\beta \neq \alpha} \frac{z_{\alpha\beta} \langle \Delta z^2 \rangle \, \beta\alpha}{E_\alpha - E_\beta}, \tag{3.103d}$$

$$c_5 = \frac{1}{2m\lambda_z^3} \sum_{\beta \neq \alpha} \frac{\langle \Delta z^2 \rangle \, \alpha\beta \, \langle \{\Delta z, p_z^2\} \rangle \, \beta\alpha}{E_\alpha - E_\beta}, \tag{3.103e}$$

$$c_6 = \frac{3\hbar^2}{m^2\lambda_z^5} \sum_{\beta \neq \alpha} \sum_{\gamma \neq \alpha} \frac{z_{\alpha\beta} z_{\beta\gamma} \langle \Delta z p_z^2 \rangle \, \gamma\alpha}{(E_\alpha - E_\beta)(E_\alpha - E_\gamma)}, \tag{3.103f}$$

$$c_7 = \frac{3\hbar^4}{m^2\lambda_z^7} \sum_{\beta \neq \alpha} \sum_{\gamma \neq \alpha} \frac{z_{\alpha\beta} z_{\beta\gamma} z_{\gamma\alpha}}{(E_\alpha - E_\beta)(E_\alpha - E_\gamma)}, \tag{3.103g}$$

$$c_8 = \frac{\hbar^2}{m\lambda_z^4} \sum_{\beta \neq \alpha} \frac{\langle g(z) \rangle \, \alpha\beta \, \langle \Delta z^2 \rangle \, \beta\alpha}{E_\alpha - E_\beta}, \tag{3.103h}$$

$$c_9 = \frac{3\hbar^4}{m^2\lambda_z^6} \sum_{\beta \neq \alpha} \sum_{\gamma \neq \alpha} \frac{z_{\alpha\beta} z_{\beta\gamma} \langle g(z) \rangle \, \gamma\alpha}{(E_\alpha - E_\beta)(E_\alpha - E_\gamma)}, \tag{3.103i}$$

$$c_{10} = |\psi_\alpha(z=0)|^2 \langle z \rangle \, \alpha, \tag{3.103j}$$

$$c_{11} = \frac{\hbar^2}{m\lambda_z^2}\sum_{\beta\neq\alpha}\frac{z_{\alpha\beta}\left\langle\delta(z)\right\rangle\beta\alpha}{E_\alpha - E_\beta}, \tag{3.103k}$$

$$c_{12} = \frac{\hbar^2}{m\lambda_z^4}\sum_{\beta\neq\alpha}\frac{\left\langle\Delta z^2\right\rangle\alpha\beta\left\langle z\right\rangle\alpha\left\langle\delta(z)\right\rangle\beta\alpha}{E_\alpha - E_\beta}, \tag{3.103l}$$

$$c_{13} = \frac{\hbar^4}{m^2\lambda_z^6}\sum_{\beta\neq\alpha}\sum_{\gamma\neq\alpha}\frac{\left\langle z\right\rangle\alpha z_{\alpha\beta}z_{\beta\gamma}\left\langle\delta(z)\right\rangle\gamma\alpha}{(E_\alpha - E_\beta)(E_\alpha - E_\gamma)}, \tag{3.103m}$$

$$c_{14} = \frac{\hbar^2}{m^2\lambda_z^5}\sum_{\beta\neq\alpha}\frac{z_{\alpha\beta}\left\langle p_z^2\right\rangle\beta\alpha\left\langle\Delta z^2\right\rangle\alpha}{(E_\alpha - E_\beta)^2}, \tag{3.103n}$$

$$c_{15} = \frac{\hbar^4}{m^2\lambda_z^6}\sum_{\beta\neq\alpha}\frac{z_{\alpha\beta}\left\langle\delta(z)\right\rangle\beta\alpha\left\langle\Delta z^2\right\rangle\alpha}{(E_\alpha - E_\beta)^2}, \tag{3.103o}$$

$$c_{16} = \frac{\hbar^4}{m^2\lambda_z^6}\sum_{\beta\neq\alpha}\frac{|z_{\alpha\beta}|^2}{(E_\alpha - E_\beta)^2}, \tag{3.103p}$$

$$c_{17} = \frac{\lambda_z^2\left\langle p_z^2\right\rangle\alpha}{\hbar^2}, \tag{3.103q}$$

$$c_{18} = \frac{\left\langle\Delta z^2\right\rangle\alpha}{\lambda_z^2}, \tag{3.103r}$$

$$c_{19} = \frac{\hbar^2}{m\lambda_z^4}\sum_{\beta\neq\alpha}\frac{|z_{\alpha\beta}|^2}{E_\alpha - E_\beta}, \tag{3.103s}$$

$$c_{20} = \frac{1}{m\lambda_z^2}\sum_{\beta\neq\alpha}\frac{\left\langle\Delta z^2\right\rangle\alpha\beta\left\langle p_z^2\right\rangle\beta\alpha}{E_\alpha - E_\beta}, \tag{3.103t}$$

$$c_{21} = \frac{\hbar^2}{m^2\lambda_z^4}\sum_{\beta\neq\alpha}\sum_{\gamma\neq\alpha}\frac{z_{\alpha\beta}z_{\beta\gamma}\left\langle p_z^2\right\rangle\gamma\alpha}{(E_\alpha - E_\beta)(E_\alpha - E_\gamma)}, \tag{3.103u}$$

$$c_{22} = \lambda_z |\psi_\alpha(z=0)|^2, \tag{3.103v}$$

$$c_{23} = \frac{\hbar^2}{m^2\lambda_z^3} \sum_{\beta\neq\alpha} \frac{\langle \Delta z^2 \rangle \, \alpha\beta \, \langle \delta(z) \rangle \, \beta\alpha}{E_\alpha - E_\beta}, \tag{3.103w}$$

$$c_{24} = \frac{\hbar^2}{m^2\lambda_z^5} \sum_{\beta\neq\alpha} \sum_{\gamma\neq\alpha} \frac{z_{\alpha\beta} z_{\beta\gamma} \, \langle \delta(z) \rangle \, \gamma\alpha}{(E_\alpha - E_\beta)(E_\alpha - E_\gamma)}. \tag{3.103x}$$

3.D Symmetric quantum well

Our main results, Eqs. (3.43)-(3.50), are valid for a general heterostructure potential and therefore also for a symmetric one. However, the latter choice substantially changes the values of constants c. Namely, for a symmetric well, only the following constants are nonzero: c_{11}, and c_{15}-c_{22}. With that, the terms g_{43}, g_{44}, g_{45} and $g_{47,0}$ are the same as given in Eqs. (3.45)-(3.48a), while the Dresselhaus and the interface term are zero, $g_d = 0 = g_z$. The remaining terms can be simplified by removing the zero c's. We get

$$g_{\rm r} = \xi_r(4c_{11} - \Phi^2 c_{15})[\eta_+ - \eta_- \cos(2\phi - 2\delta)], \tag{3.104}$$

for the contribution from the Rashba interaction, and

$$g_{47,2} = \frac{\lambda'_{47}}{\lambda_z} c_{22} c_{16} \Phi^2 \sin(2\phi)[\eta_+ - \eta_- \cos(2\phi - 2\delta)], \tag{3.105}$$

for the H_{47} contribution.

The above results are valid for a general symmetric quantum-well potential. We now specify to a rectangular potential,

$$V_z = \begin{cases} V_A, & \text{if } z \notin \langle -l_z/2, l_z/2 \rangle, \\ V_B, & \text{if } z \in \langle -l_z/2, l_z/2 \rangle. \end{cases} \tag{3.106}$$

It defines the nominal width as the thickness of the material B layer sandwiched by material A. The effective mass and the g-factor are taken piecewise constant in the three regions. We take the same parameter values for the mass and bulk g-factor in material A and B as given below Eq. (3.25), and use $V_B - V_A = 300$ meV. With these amendments, we are ready to analyze the g-factor corrections for a rectangular quantum well quantitatively. We plot the g-factor subband average in the main

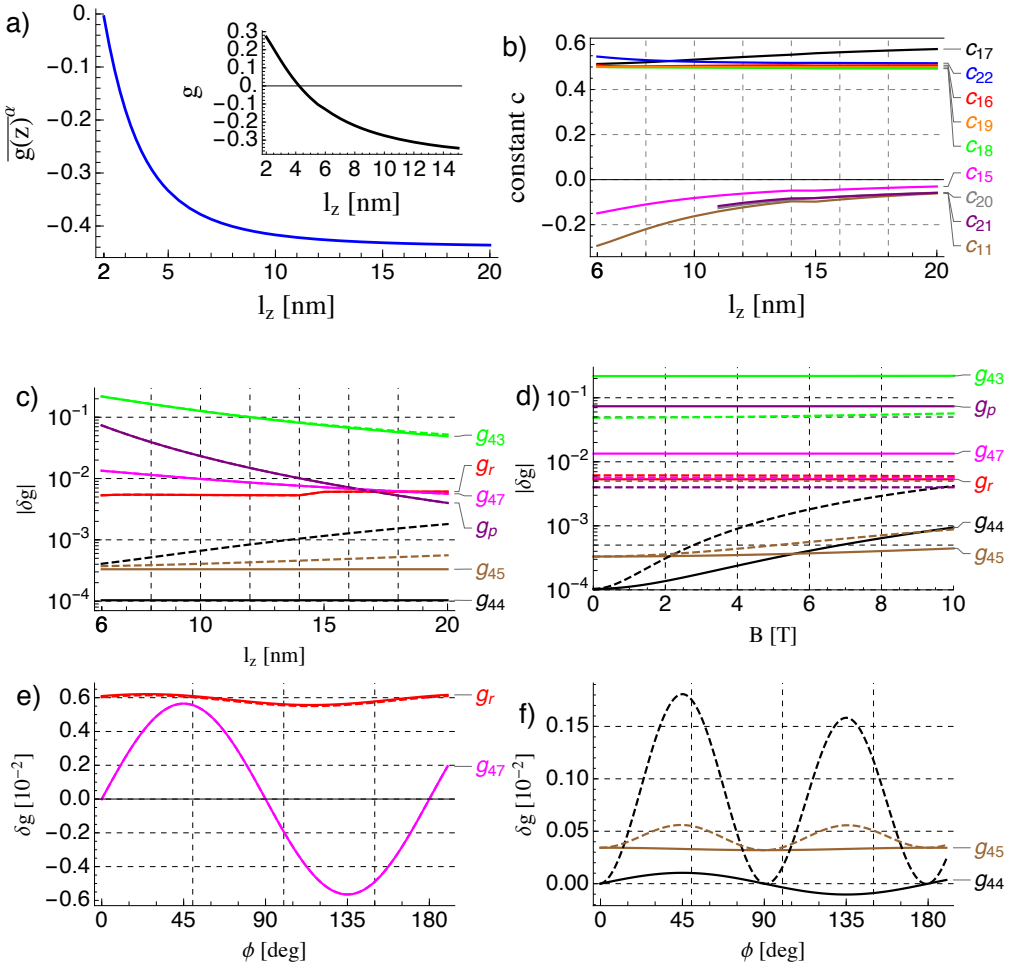

Figure 3.7: The corrections to the g-factor, labeled according to the notation of Eqs. (3.43)–(3.50), for a symmetric quantum well with a rectangular confinement. The parameters are the same as in Fig. 3.5 unless stated otherwise. (a) The lowest order approximation to the g-factor, showing the value of $\langle g(z)\rangle\,\alpha$ for the lowest subband, $\alpha = 1$, as a function of the well width, defined in Eq. (3.106). Inset: The total g-factor, calculated by adding all corrections to the bulk value in material B. (b) The values of non-zero constants c. Note that c_{20} and c_{21} become formally zero if the quantum well does not have at least 2 subbands. To correct this behavior, one would have to include the contributions from delocalized eigenstates of Eq. (3.4), what we do not do here (the resulting effects on the other panels would be hard to spot). (c) Corrections as a function of the quantum well width. The solid (dashed) curves show corrections for $B = 0$ T ($B = 6$ T). (d) As a function of the magnetic field. The solid (dashed) curves show corrections for $l_z = 6$ nm ($l_z = 20$ nm). (e-f) As a function of the magnetic field orientation. The solid (dashed) curves show corrections for $B = 0$ T ($B = 6$ T).

panel of Fig. 3.7(a). Upon narrowing the quantum well, the g-factor grows, reflecting the wavefunction penetrating into AlGaAs. The inset of Fig. 3.7(a) shows the total g-factor as a function of the quantum well width. We plot it to demonstrate the crossing of zero, at about $l_z = 4.2$ nm for our parameters, what has been debated some years ago. [123, 124, 128, 151]

We plot the constants c in Fig. 3.7(b). One can see that now they fall into 2 groups, with similar values among their members. Changes in constants c compared to the triangular potential imply changes in the hierarchy of g-factor corrections. Indeed, Fig. 3.7(c)-(d) shows that for a symmetric well, the g-factor correction is basically dominated by a single term, H_{43}. For very narrow wells, the penetration might be also visible in experiments with high resolution. On the other hand, there is no appreciable effect from the magnetic field to be expected. Finally, the directional dependence is shown in Fig. 3.7(e)-(f). There is very little variation, [152] way below the current experimental resolution. The largest variation is from H_{47} and reaches 0.01, with extrema along the crystal axes.

3.E Magnetic-field-dependent corrections

We obtained corrections to the g-factor which are proportional to the second power of the flux Φ, and therefore second power of the in-plane magnetic field (see also Footnote 9). In the main text, we denoted such terms as $g_{\mathrm{x},2}$, where x denotes the origin of the term, for example, $\mathrm{x} = \mathrm{d}$ for Dresselhaus. We note that such a cubic Zeeman energy term was fitted from the data measured in Ref. 153. The notation of that reference, g_3, relates to our notation here by $g_3 = g_{\mathrm{x},2}\mathbf{b}^{-2}$. We plot our results in this notation in Fig. 3.8. From that figure, one can see that the Rashba and, for wide 2DEGs, the Dresselhaus terms dominate, respectively. Unlike for the magnetic-field-independent corrections, the term $\mathrm{x} = 43$ is not very relevant. We also find an agreement with the value $g_3 \approx +4.7 \times 10^{-4}\ \mathrm{T}^{-2}$ fitted in that experiment, including its sign, for the effective 2DEG width of around 8.5 nm. Under these conditions, the g-factor B-field nonlinearity is dominated by the Rashba term.

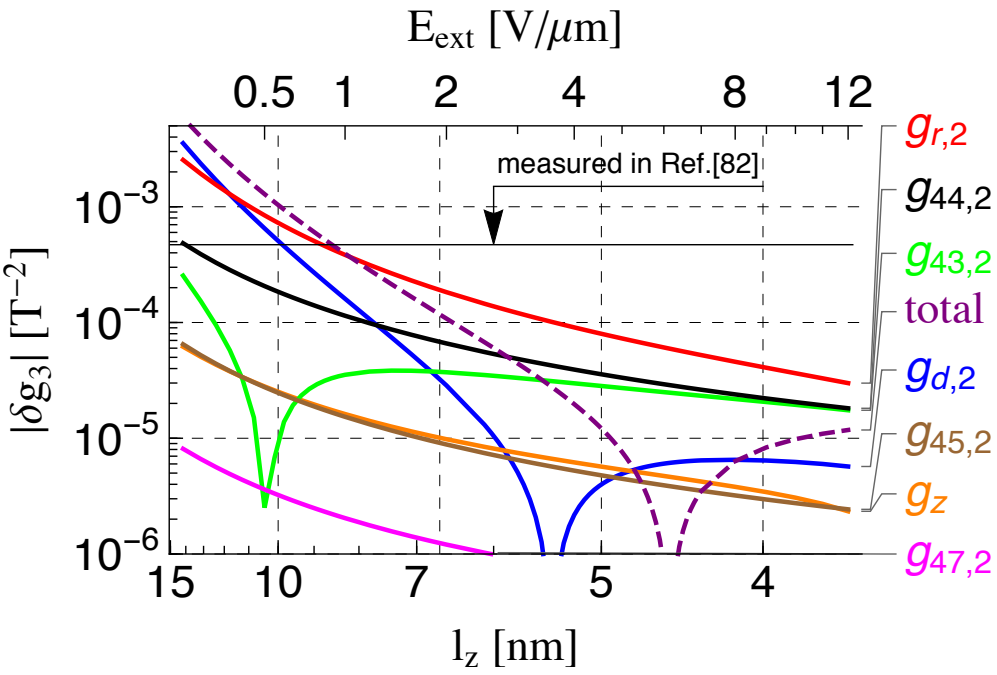

Figure 3.8: The g-factor corrections quadratic in the in-plane magnetic field as a function of the 2DEG width. All parameters are the same as in Fig. 3.5(a) except for $\phi = -45°$, chosen in line with the experiment in Ref. 153. We label the curves using the notation in Eqs. (3.43)-(3.49) and label the sum of all plotted contributions by "total". We transform our dimensionless quantities into the notation of Ref. 153, defined by $g_3 = g_{x,2}b^{-2}$, which has therefore units of T^{-2}. In that experiment, the value $g_3 \approx 0.47 \times 10^{-3}$ T^{-2} was fitted from data, which is drawn as a horizontal black solid line. The 2DEG width in that experiment is not known to us.

3.F Mixed contribution example

Here we derive a g-factor correction which is of the second order in spin-orbit couplings. For the sake of illustration, we do it only for the Rashba term, Eq. (3.19). According to the scheme followed in Sec. 3.2, this term would be split according to the powers of the in-plane magnetic field to two terms, $H_R = H_{r,0} + H_{r,1}$, with

$$H_{r,0} = \frac{\alpha_R(z)}{\hbar}(p_x\sigma_y - p_y\sigma_x), \tag{3.107a}$$

$$H_{r,1} = \frac{e\alpha_R(z)}{\hbar}(a_{||,x}\sigma_y - a_{||,y}\sigma_x). \tag{3.107b}$$

In further, we use the relation

$$\mathbf{p} = \frac{im}{\hbar}[h_{2D}, \mathbf{r}] \equiv \frac{im}{\hbar}L_{2D}(\mathbf{r}), \tag{3.108}$$

where the identity sign is the definition of the Liouvillian operator L_{2D} corresponding to the two-dimensional Hamiltonian Eq. (3.8). Since we aim at calculating the contributions to the effective Hamiltonian up to the second order only, we can use the simplified formula given in Eq. (3.32). With this, several terms result: choosing the pair $H_{r,n}$-$H_{r,m}$ in the two terms in the latter equation gives four choices, each of which splits to the intra-subband and inter-subband term (eight terms in total).

Let us calculate one of these: the intra-subband contribution coming from a pair $H_{r,0}$-$H_{r,0}$. In this case, using the Liouvillian definition allows us to bring the effective Hamiltonian into the following form

$$H^{(\alpha)}_{r,0;r,0}(\text{intra}) = \frac{1}{2}[L^{-1}_{2D}(\langle H_{r,0}\rangle\,\alpha), \langle H_{r,0}\rangle\,\alpha]. \tag{3.109}$$

Using the explicit form of the Liouvillian, the commutator can be evaluated, and we get

$$H^{(\alpha)}_{r,0;r,0}(\text{intra}) = -m\left(\frac{\langle\alpha_R(z)\rangle\,\alpha}{\hbar}\right)^2\left(1 + \sigma_z\frac{L_z}{\hbar}\right), \tag{3.110}$$

with $L_z = xp_y - yp_x$. If we now assume a symmetric in-plane confinement potential, $l_x = l_y = l_0$, the expectation value of this operator in the ground state can be easily calculated,

$$\langle 0|L_z|0\rangle = \frac{eB_z}{4}l_B^2. \tag{3.111}$$

The magnetic-field-renormalized confinement length is

$$l_B = \left(l_0^{-4} + \frac{e^2 B_z^2}{4\hbar^2} \right)^{-\frac{1}{4}}. \tag{3.112}$$

We can now convert this expression into a renormalization of the out-of-plane component of the g-tensor,

$$(g_{rr,0})_{zz} = -\frac{1}{2} \left(\frac{\langle \alpha_R(z) \rangle \, \alpha}{\hbar} \right)^2 \frac{me}{\hbar \mu_B} l_B^2. \tag{3.113}$$

For small out-of-plane fields, so that the magnetic field does not strongly renormalize the confinement, $l_B \approx l_0$, this term evaluates to $(g_{rr,0})_{zz} \approx -0.0012$ for a typical value $l_0 = 34$ nm. Therefore, it is 1-2 orders of magnitude smaller than the leading terms which are linear in the spin-orbit couplings.

The remaining terms among the possibilities that we enumerated below Eq. (3.108) are even smaller due to the smallness of various matrix elements of the function $\alpha_R(z)$. For example, the inter-subband term for the pair $H_{r,0}$-$H_{r,0}$ is proportional to the minute value of $\langle \alpha_R(z) \rangle \, \alpha\beta$. Similarly, the intra-subband term for the pair $H_{r,0}$-$H_{r,1}$ would contain the matrix element $\langle (z - z_0) \alpha_R(z) \rangle \, \alpha$, etc. All these matrix elements are very small, as they are similar in nature, and in value, to the constants c_8 and c_9, see App. 3.C and Fig. 3.4.

Finally, we note that similar terms would arise from the Dresselhaus interaction. The analogous term, the intra-subband contribution from $H_{d,0}$-$H_{d,0}$, would give

$$H^{(\alpha)}_{d,0;d,0}(\text{intra}) \approx -m \left(\frac{\gamma_c \langle p_z^2 \rangle \, \alpha}{\hbar^3} \right)^2 \left(1 - \sigma_z \frac{L_z}{\hbar} \right). \tag{3.114}$$

The largest-in-magnitude correction arising in the second order of the spin-orbit coupling is therefore [71, 154]

$$g_{zz}^{\text{2nd}} = \frac{1}{2} \left[\left(\frac{\gamma_c \langle p_z^2 \rangle \, \alpha}{\hbar^3} \right)^2 - \left(\frac{\langle \alpha_R(z) \rangle \, \alpha}{\hbar} \right)^2 \right] \frac{me}{\hbar \mu_B} l_B^2. \tag{3.115}$$

Only the zz component of the g-tensor is changed by a very small value, typically 10^{-3}. Even though this effect was invoked to interpret the experiment in Ref. 155, probably a different interaction was responsible for the observed anisotropy there, perhaps H_{45}. As we are mostly interested in the in-plane magnetic fields, we do not pursue this issue further.

CHAPTER 4

Boundary Spin Polarization as a Robust Signature of a Topological Phase Transition

Adapted from:
Marcel Serina, Daniel Loss, and Jelena Klinovaja,
"Boundary spin polarization as a robust signature of a topological phase transition in Majorana nanowires",
Phys. Rev. B **98**, 035419 (2018).

We show that the boundary charge and spin can be used as alternative signatures of the topological phase transition in topological models such as semiconducting nanowires with strong Rashba spin-orbit interaction in the presence of a magnetic field and in proximity to an s-wave superconductor. We identify signatures of the topological phase transition that do not rely on the presence of Majorana zero-energy modes and, thus, can serve as independent probes of topological properties. The boundary spin component along the magnetic field, obtained by summing contributions from all states below the Fermi level, has a pronounced peak at the topological phase transition point. Generally, such signatures can be observed at boundaries between topological and trivial sections in nanowires and are stable against disorder.

4.1 Introduction

Topological models have attracted a lot of attention in recent years. One of the first topological systems proposed about fourty years ago is the Su-Schrieffer-Heeger (SSH) model [156], describing properties of one-dimensional dimerized polymers. In this spinless model, a nondegenerate fermionic zero-mode, localized at a domain wall, is associated with a well-defined half-integer boundary charge [157, 158]. The same results were first predicted in a continuum model proposed by Jackiw and Rebbi [159]. The half-integer value of the boundary charge in these models is protected by the chiral symmetry. If this symmetry is broken, the value of the boundary charge can deviate from $e/2$ [157, 160]. Importantly, however, in the topological regime, there is always a boundary charge (independent of the presence of bound states) at the domain wall as was shown in several extensions of the SSH model [161–163]. Recently, the concept of the fractional boundary charge in topological SSH models was revisited, aiming at different systems that could be realized in modern experimental settings [164–182] and even in higher dimensions [183–185]. Motivated by these studies on boundary charges we would like to go a step further and focus in this work on boundary spins. In particular, we want to study the behavior of boundary spins in- and outside the topological phase and demonstrate that the total moment of spins close to the boundary can be used as signature for the topological phase transition.

Currently, Majorana fermions (MFs), proposed as a real-field solution of the Dirac equation and thus being its own antiparticle [37], attract the most attention among the known bound states in topological systems. With the rapidly growing interest in topological properties of condensed matter systems [186–192], MFs were proposed to be present in various theoretical and experimental setups [39, 193–208]. The most promising ones among them being chains of magnetic adatoms on superconducting surfaces [209–211] and semiconducting nanowires (NWs) with sizeable Rashba spin-orbit interaction (SOI) in the presence of a magnetic field and proximity-induced superconductivity [212–216]. Majorana fermions can be used as building blocks for topological quantum computing [217, 218] and can be combined with spin qubits in quantum dots into hybrid architectures [219–229].

Most of the studies [229–239] so far focused on the transport properties of such NWs in the topological regime or on properties of MFs themselves and their dependence on physical parameters. Also, there

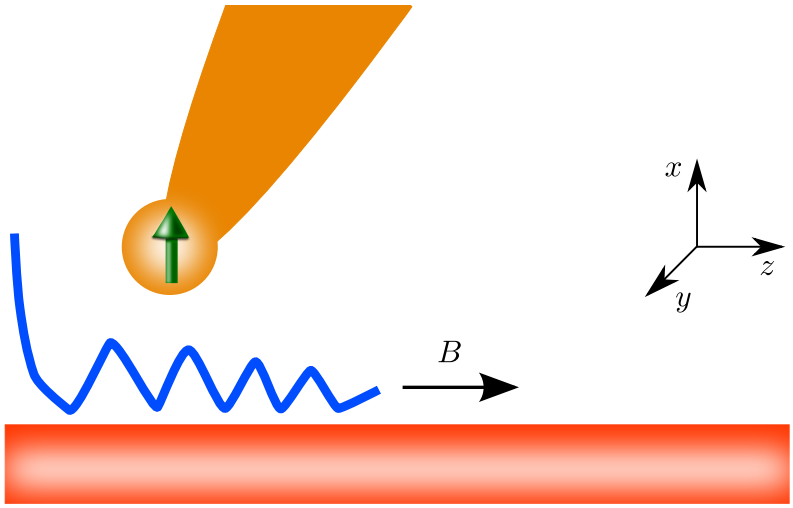

Figure 4.1: Our setup consists of a semiconducting NW (red bar) with Rashba SOI and with proximity-induced superconductivity due to coupling to a bulk s-wave superconductor (not shown). The SOI vector α points along the y direction. A magnetic field B applied along the NW axis is used to tune the system in and out of the topological phase. The boundary spin accumulates at the edges of the NW (blue curve) and can be used to identify the topological phase transition point. The magnetic signal can be measured by using *e.g.* NV centers (green arrow) on a tip (orange).

has been substantial interest recently in the investigation of the spin polarization of Andreev and Majorana bound states [240, 241]. However, it has been pointed out that great care must be taken when identifying topological phases from the presence of quasiparticle states inside the superconducting gap [242–244]. Thus, it is most desirable to have additional signatures available (besides MFs) that would allow one to identify the topological phase transition. Recent works, which analyzed the bulk signatures of the topological transition, focused either on the spinless Kitaev model [245] or studied finite-size scaling of the ground state energy in a generic conformal field theory approach for each of the symmetry classes [246]. In this work, we would like to investigate the experimentally most relevant model of Rashba NWs and to provide relevant quantities accessible by state-of-the-art measurements. In contrast to aformentioned works, we also focus on local boundary effects and consider here different aspects of topological phases in one-dimensional systems, namely non-transport signatures of the topological phase tran-

sition in the *bulk* states, or, more precisely, in the boundary charge and boundary spin to which all occupied states close to the Fermi level contribute.

4.2 Model

We investigate the system composed of a semiconducting NW with strong Rashba SOI in the proximity to a bulk s-wave superconductor in the presence of a magnetic field B applied along the NW axis along z direction, see Fig. 4.1. The SOI vector α points along the y direction. The B-field results in the Zeeman energy $\Delta_Z = g\mu_B B/2$, where g is g-factor and μ_B the Bohr magneton. The corresponding tight-binding Hamiltonian is written as [234]

$$\begin{aligned} H = &-t\sum_{\langle jj'\rangle\sigma}\left(c^\dagger_{j\sigma}c_{j'\sigma} + \text{H.c.}\right) + (2t-\mu)\sum_{j\sigma} c^\dagger_{j\sigma}c_{j\sigma} \\ &+ \Delta_Z \sum_{j\sigma\sigma'} c^\dagger_{j\sigma}\sigma_z^{\sigma\sigma'}c_{j\sigma'} + i\sum_{\langle jj'\rangle\sigma\sigma'}\left(\alpha c^\dagger_{j\sigma}\sigma_y^{\sigma\sigma'}c_{j'\sigma'} + \text{H.c.}\right) \\ &+ \Delta_{SC}\sum_j\left(c^\dagger_{j\uparrow}c^\dagger_{j\downarrow} + \text{H.c.}\right), \end{aligned} \tag{4.1}$$

where the creation operator $c^\dagger_{i\sigma}$ creates an electron with spin $\sigma =\uparrow,\downarrow$ at site j of a chain consisting of N sites with lattice constant a. In the first and fourth terms, the summation runs only over neighbouring sites j and j'. Here, t denotes a nearest-neighbour hopping matrix element, μ is the chemical potential, and Δ_{SC} denotes the superconducting gap induced by proximity to the bulk s-wave superconductor. We note that in our model $\mu = 0$ corresponds the chemical potential being tuned to the SOI energy, which is defined here as $E_{SO} = \alpha^2/t$. For the rest of the paper we fix $t = 1$ and use it as an energy scale. The system is in the topological phase hosting zero-energy MFs at the nanowire ends if $\Delta_Z > \Delta_Z^c$, where $\Delta_Z^c = \sqrt{\mu^2 + \Delta_{SC}^2}$ [39, 195]. To study the topological phase transition in semiconducting NWs, we focus on the experimentally most relevant strong SOI regime, $E_{SO} \gg \Delta_{SC}, \Delta_Z$ [212, 216].

By diagonalizing numerically the Hamiltonian H [see Eq. (4.1)], one can determine the energy spectrum E_n. In addition, one also finds the operators $\psi_n = \sum_j\left(u^*_{\uparrow nj}c_{\uparrow j} + u^*_{\downarrow nj}c_{\downarrow j} + v^*_{\uparrow nj}c^\dagger_{\uparrow j} + v^*_{\downarrow nj}c^\dagger_{\downarrow j}\right)$, corresponding to annihilation operators for each of these $n = 4N$ states. Due to particle-hole symmetry, all states appear in pairs, *i.e.* if E_n is a solution, then so

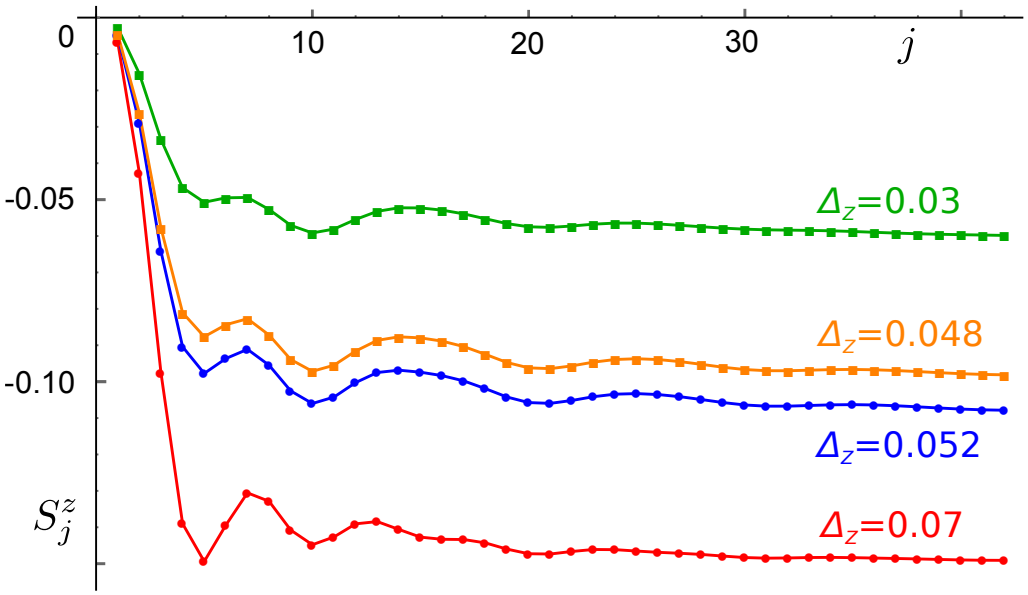

Figure 4.2: The spin density S_j^z (projection along B-field) as a function of site j. Away from the NW ends, S_j^z is constant and given by S_0^z determined solely by bulk properties of the system. However, close to NW ends, S_j^z oscillates in all parameter regimes and there is no qualitative difference between trivial (indicated by squares) and topological (indicated by dots) phase. In all plots, the lines are guides to the eye. However, there is a quantitative shift in the amplitude of the first oscillations, as the system is driven through the topological phase transition. We consider the system being deep in (red, $\Delta_Z = 0.07$) and out of (green, $\Delta_Z = 0.03$) the topological phase as well as close to the topological phase transition in (blue, $\Delta_Z = 0.048$) and out of (orange, $\Delta_Z = 0.052$) the topological phase. The parameters are fixed to $N = 150$, $\mu = 0$, $\alpha = 0.3$, and $\Delta_{SC} = 0.05$. This choice of parameters corresponds to typical values observed in experiments with nanowires such as: $m = 0.015 m_e$, $v_F = 0.8 \times 10^6$ m/s, $E_{SO} = 0.9$ meV, and $\Delta_{SC} = 0.5$ meV (with $a = 15$ nm, $t = 10$ meV).

is $-E_n$. In what follows, we will focus on non-positive energy states. To characterize local bulk properties, we define the local charge ρ_j and the

local spin densities $S_j^{x,y,z}$ at each site as

$$\rho_j = \sum_{E_n<0;\sigma} \left(|u_{\sigma nj}|^2 - |v_{\sigma nj}|^2\right), \tag{4.2a}$$

$$S_j^z = \sum_{E_n<0;\sigma} \sigma \left(|u_{\sigma nj}|^2 - \sigma|v_{\sigma nj}|^2\right), \tag{4.2b}$$

$$S_j^x = \sum_{E_n<0;\sigma} \left(u_{\sigma nj}u^*_{\bar{\sigma} nj} - v_{\sigma nj}v^*_{\bar{\sigma} nj}\right), \tag{4.2c}$$

$$S_j^y = i \sum_{E_n<0;\sigma} \left(\sigma u_{\sigma nj}u^*_{\bar{\sigma} nj} - \sigma v_{\sigma nj}v^*_{\bar{\sigma} nj}\right), \tag{4.2d}$$

where the index $\sigma = 1$ ($\bar{1}$) corresponds also to spin up (down) states defined above, see Fig. 4.2. For zero-energy MF wavefunctions one can show that $u^*_{\uparrow nj} = v_{\uparrow nj}$ and $u^*_{\downarrow nj} = v_{\downarrow nj}$. Thus, the MF charge and spin densities are exactly zero [40] and they do not contribute to Eq. (4.2). For this reason, we take in our definition only bulk states with negative energies into account. In addition, in our model, the Hamiltonian is real, so all the eigenvectors can also be chosen to be real. As a consequence, we find that S^y is identically zero for all configurations considered below.

Away for the NW ends, both spin and charge densities are constant as expected in a translationally invariant system, see Fig. 4.2. However, close to the NW end, these quantities oscillate around their bulk values ρ_0 and $S_0^{x,z}$ determined as the value at the middle of the NW $\rho_0 = \rho_{j=\left[\frac{N}{2}\right]}$ and $S_0^{x,z} = S^{x,z}_{j=\left[\frac{N}{2}\right]}$, where $[M]$ denotes the integer part of M. Here, we assume that the NW is long enough such that these oscillations decay in the middle of the NW. In the strong SOI regime [40, 239], there are two lengthscales associated with bulk gaps at exterior branches $\xi_e/a = 2\alpha/\Delta_{SC}$ and interior branches $\xi_i/a = 2\alpha/\left|\Delta_{SC} - \Delta_Z\right|$. In what follows, we work in the regime in which the NW length L is much longer than both ξ_e and ξ_i, see Fig. 4.2.

Our main interest are boundary effects. As a result, for further convenience [247], we define the left and right boundary charge and spin

as

$$\tilde{\rho}_{Lm} = \sum_{j=1}^{m} (\rho_j - \rho_0) , \tag{4.3}$$

$$\tilde{S}^{x,z}_{Lm} = \sum_{j=1}^{m} \left(S^{x,z}_j - S^{x,z}_0\right) , \tag{4.4}$$

$$\tilde{\rho}_{Rm} = \sum_{j=N-m}^{N} (\rho_j - \rho_0) , \tag{4.5}$$

$$\tilde{S}^{x,z}_{Rm} = \sum_{j=N-m}^{N} \left(S^{x,z}_j - S^{x,z}_0\right) . \tag{4.6}$$

First, we subtract from charge and spin densities their bulk values. Second, we sum densities over m sites at the left or right edge to define the right and left boundary charge or spin. Our system is symmetric with respect to the middle of the NW, so right and left boundary charges and spins can at most differ in sign. In our case, we find that $\tilde{\rho}_{Lm} = \tilde{\rho}_{Rm}$ and $\tilde{S}^z_{Lm} = \tilde{S}^z_{Rm}$, whereas $\tilde{S}^x_{Lm} = -\tilde{S}^x_{Rm}$, see the Appendix 4.A. We confirm that for values of m such that $\max\{\xi_e, \xi_i\}/a \ll m \ll N/2$, $\tilde{\rho}_m$ and $\tilde{S}^{x,z}_m$ converge to a constant values $\tilde{\rho}_{R,L}$ and $\tilde{S}^{x,z}_{R,L}$. Without loss of generality, in what follows, we focus only on the left boundary charge and spin.

4.3 Signature of topological phase transition

Next, we focus on the characteristic behavior of the boundary charge and spin around the topological phase transition. First, we analyze the behaviour of the spin density along the magnetic field S^z_j for various values of Zeeman gaps and all the other parameters fixed, see Fig. 4.2. As expected, S^z_j is constant in the middle of the chain and saturates to S^z_0, however, as one approaches the end of the chain, spatial oscillations in S^z_j begin to emerge. Not surprisingly, the spin polarization along the magnetic field strongly depends on the strength of the B-field. The stronger the magnetic field is, the larger is the polarization, see Fig. 4.2. Close to the phase transition point, the oscillations in S^z_j at the NW ends get more pronounced and are characterized by higher amplitudes and longer decay lengths. In order to quantify these oscillations, we calculate numerically the boundary spin and charge as defined in Eq. (4.4). The signature of the topological phase transition can be clearly seen in the z-component

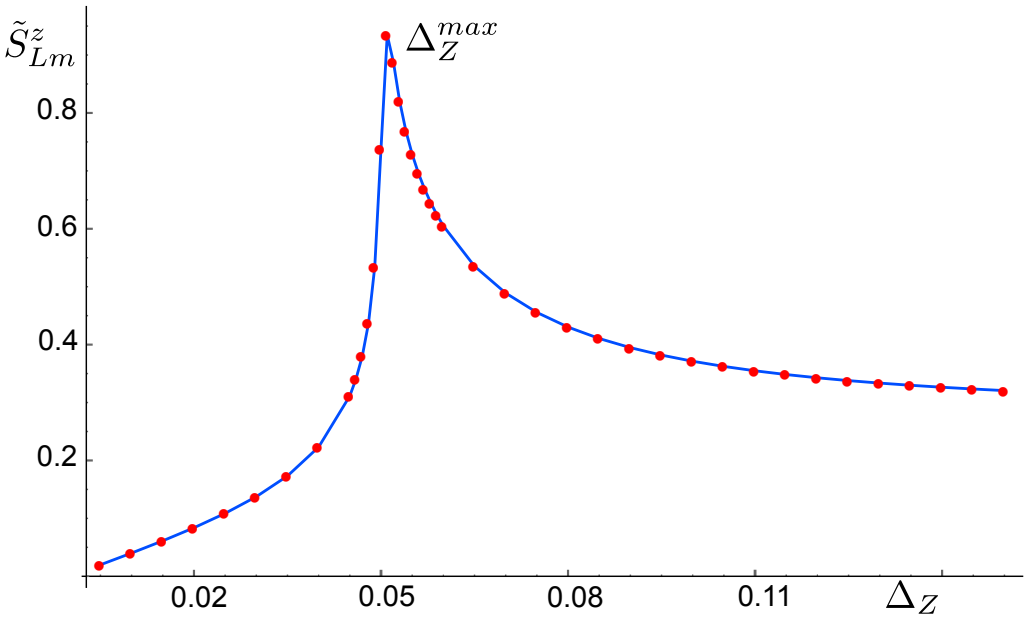

Figure 4.3: The left boundary spin component along z direction, $\tilde{S}^z_{Lm}$, [see Eq. (4.4)] as a function of the Zeeman energy Δ_Z. The $\tilde{S}^z_{Lm}$ has a peak at Δ_Z^{max}, which coincides in sufficiently long systems with the point of the topological phase transition $\Delta_Z = \Delta_{SC}$. This peak is an independent signature of the topological phase transition. The system parameters are taken to be $\alpha = 0.3, \Delta_{SC} = 0.05$, $\mu = 0$, $N = 2000$, and $m = 1000$.

of the boundary spin, $S^z_{L/Rm}$, see Fig. 4.3. In the Appendix 4.A, we also provide details on the boundary charge and the S^x-component, however, there is no signature of the topological phase transition in these quantities. In contrast to that, the $S^z_{L/Rm}$ has a pronounced peak at the value of the Zeeman energy Δ_Z^{max} that is very close to the critical value Δ_Z^c determined from the topological criterion. The longer the system is, the more close Δ_Z^{max} to Δ_Z^c, see Fig. 4.4. We find that Δ_Z^{max} weakly depends on the system size N and approaches the critical value asymptotically as a function of $1/N$. Importantly, the value of $S^z_{L/Rm}$ does not depend on whether the MF state is occupied or not as its contribution is identically zero. Thus, for long enough systems, the position of the peak in $S^z_{L/Rm}$ can be used as an independent signature of the topological phase transition.

It is also important to emphasize the role of the chemcical potential μ. It is well known that the system can also be driven between topological and trivial phases by changing μ [39, 195]. In this case, when the topo-

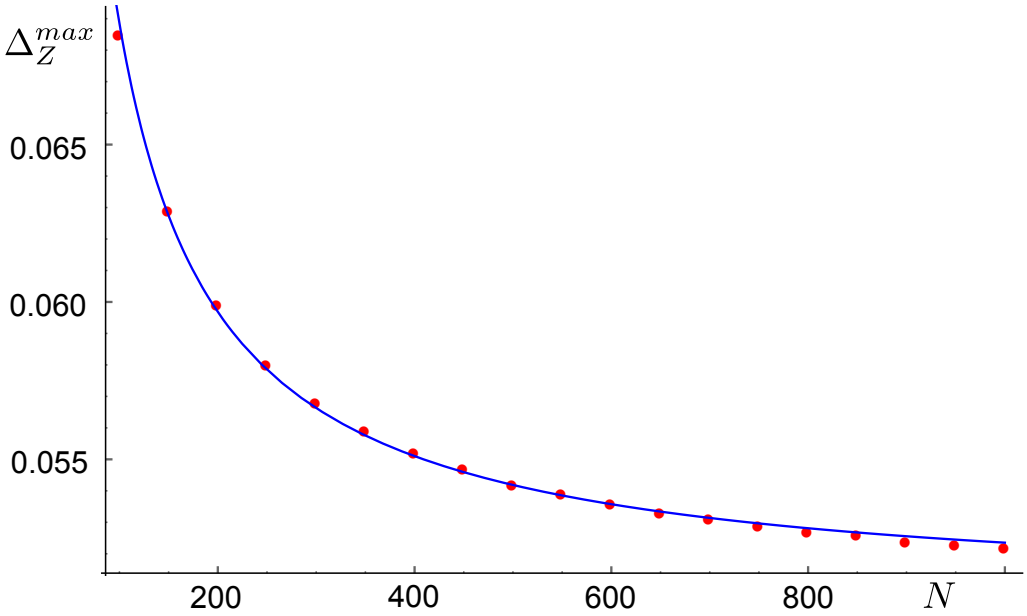

Figure 4.4: The position of the peak Δ_Z^{max} in $\tilde{S}^z_{Lm}$ [see Eq. (4.4)] as a function of system size N. As the system size is increases, Δ_Z^{max} gets more and more close to the critical value Δ_Z^c at which the topological phase transition takes place. We find that the obtained numerically results (red dots) can be fitted the best with the analytical formula $(\Delta_Z^{max} - \Delta_Z^c) \propto 1/N$ (blue curve). The system parameters are the same as in Fig. 4.3 with $m = N/2$.

logical phase is reached, there are two peaks in $\tilde{S}^z_{Lm}$ at two critical values $\mu = \pm\mu_c$ with $\mu_c = \sqrt{\Delta_Z^2 - \Delta_{SC}^2}$, see Fig. 4.5. Again, we see that the critical values $\pm\mu_c$ are asymptotically reached as the size of the system is increased. However, when the width of two peaks is comparable with μ_c, the two peaks will merge. Thus, this criterion works best for large values of Δ_Z and long systems. We note that one faces the same problem if the detection of the phase transition is done via zero-bias peak signatures in transport measurments. In short nanowires, the MFs of opposite ends will overlap and split away from zero energy if one is not deeply in the topological phase.

Finally, we would like to demonstrate the stability of the presented signatures against disorder and, thus, show that they are also topologically protected. For this, we add on-site disorder to our model [see Eq. (4.1)] as well as we modify the system by adding trivial section at the NW end. Results for the both cases are presented in the Appen-

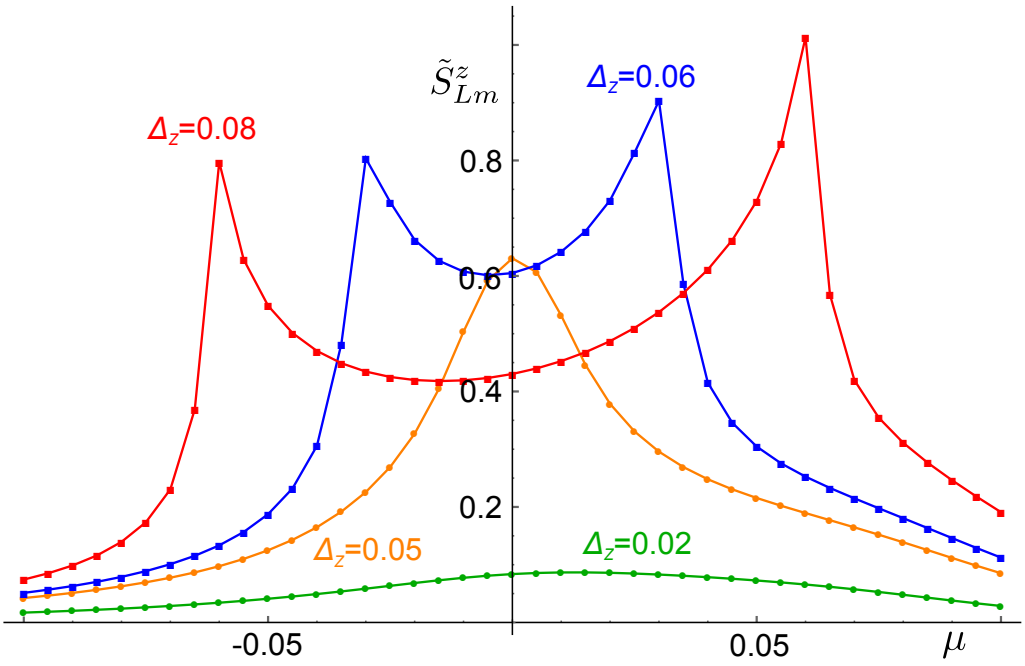

Figure 4.5: The z component of the boundary spin $\tilde{S}^z_{Lm}$ [see Eq. (4.4)] as a function of the chemical potential μ. In the topological regime, there are two peaks corresponding to two critical values of the chemical potential $\pm\mu_c$, at which the system goes through the topological phase transition. In the trivial regime such peaks are absent as the system cannot be tuned into the topological phase. Far from the transition point (green, $\Delta_Z = 0.02$) there is a broad maximum in $\tilde{S}^z_{Lm}$ which gets more pronounced as system approaches the topological phase transition (orange, $\Delta_Z = 0.05$) and develops later into a double peak structure (blue, $\Delta_Z = 0.06$ and red, $\Delta_Z = 0.08$) in the topological phase. The system parameters are fixed to $N = 1000$, $\alpha = 0.3$, $\Delta_{SC} = 0.05$, and $m = 500$.

dices 4.C, 4.D. In all configurations, the signature of the topological phase transition in the boundary spin $\tilde{S}^z_{Lm}$ is still fully present.

So far we have focused on signatures of the topological phase transition to be detected in the boundary spin. However, the bulk values of the spin component along the magnetic field S^z_0 also carry information about the topological phase transition if periodic boundary conditions are imposed, see the Appendix 4.E for details. In this case, the system is translationally invariant and it does not matter at which point one computes the bulk value of the spin component S^z_{PBC}. The signature of the topo-

logical phase transition is still present but different. In particular, there is now a sharp discontinuity in $\bar{S}^z_{PBC}$ with a jump of order $1/N$ at the point of the topological phase transition, $\Delta_Z = \Delta_Z^c$, see the Appendix 4.E.

The measurement of boundary spins will be challenging but seems to be within reach for state-of-the-art magnetometry with NV-centers or nanoSQUIDs [248–252, 252, 253]. We furthermore recall that it is the total integral over the spin density within the localization length that determines the spin signature of the phase transition. Thus, a resolution of the measurement device over this length scale should be sufficient and is already reached in the aformentioned magnetometric measurements. Moreover, all those techniques were already perfomed at cryogenic temperatures necessary for our proposal as one should work at temperatures that do not exceed the scale set by the bulk gap [254]. Finally, in contrast to STM measurements, these techniques are non-invasive and, thus, can be used to measure reliably the magnetic signals we propose.

4.4 Conclusions

We have identified signatures of the topological phase transition in the boundary spin component in one-dimensional topological systems. These signatures are present when tuning through the phase transition point either with the magnetic field or with the chemical potential. Moreover, we have shown that these signatures do not rely on the presence of MFs and always occur at the boundary between topological and trivial sections of the NW. We have analyzed the finite-size effects of the boundary spin and shown that the position of the peak converges to the value obtained analytically in the continuum limit. These results are also stable with respect to disorder. We also found that such signatures of the phase transition do not show up in all boundary observables, *e.g.* the boundary charge and the other polarizations of the boundary spin do not exhibit such discontinuities at the phase transition. These signatures are all related to the extended wavefunctions which contain information about the whole system, *i.e.*, bulk and boundaries. Bulk properties which are determined by the same extended wavefunctions can also exhibit signatures of the phase transitions [245, 246]. As an outlook, it would thus be interesting to explore the connection between phase transition signatures at the boundaries with those occurring in the bulk of the system.

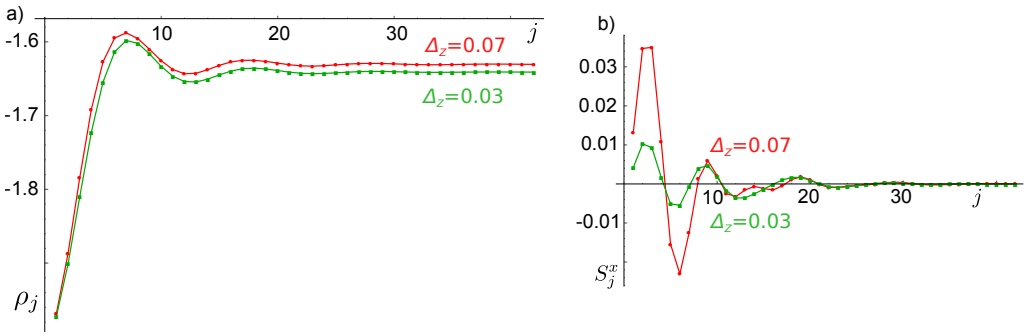

Figure 4.6: (a) Charge density ρ_j and (b) component of the spin density along the x axis, S_j^x, as a function of site position j. The characteristic features are similar to those of S_j^z discussed in the main text, again there are oscillations close to the NW ends in both trivial and topological phases. However, neither the amplitude of the first oscillation does not differ between the two phases [see (a)] nor the oscillations tend to cancel each other [see (b)]. Results for the trivial (topological) phase are marked by green squares (red cycles) and correspond to $\Delta_Z = 0.03$ ($\Delta_Z = 0.07$). The system parameters are chosen to be $N = 150$, $\mu = 0$, $\alpha = 0.3$, $\Delta_{SC} = 0.05$.

4.A Results for boundary spin component S_{Lm}^x and boundary charge ρ_{Lm}

For the sake of completeness, we present here our results for the local spin density S_j^x and charge density ρ_j, see Fig. 4.6. As the SOI vector points along the x direction, it is expected that S_j^x in the center of the chain vanishes and moreover $\sum_{j=1}^{N} S_j^x = 0$, which imposes that S_j^x must be antisymmetric with respect to the middle of the chain. We confirm this expectation by exact numerical diagonalization. As in the case of S_j^z, spatial oscillations in S_j^x appear close to the ends of the NW, getting more pronounced as one approaches the topological phase transition. In case of the charge density ρ_j, the characteristic behavior is very similar while in this case, as expected, the results are symmetric with respect to the middle of the wire. We also calculate the corresponding boundary charge $\tilde{\rho}_{Lm}$ and the boundary spin component $\tilde{S}_{Lm}^x$ (see Fig. 4.7). However, we do not observe any well-pronounced signatures of the topological phase transition in these quantities. For $\tilde{\rho}_{Lm}$, we can see a transition from almost constant to a linear dependence of Δ_Z, however, this signature seems to be difficult to measure.

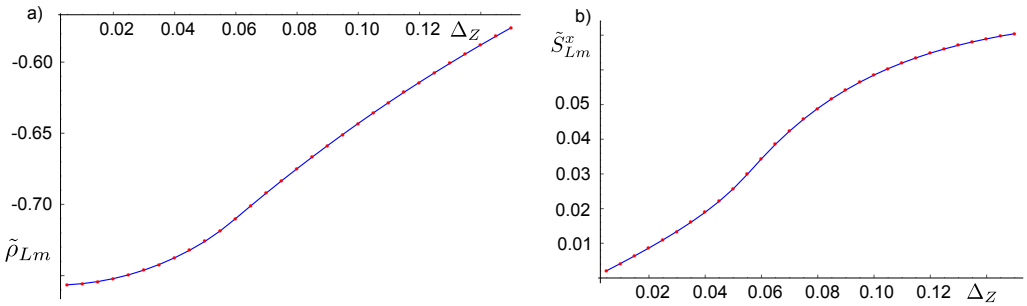

Figure 4.7: (a) Boundary charge $\tilde{\rho}_{Lm}$ and (b) component of the boundary spin along the x axis $\tilde{S}^x_{Lm}$ as a function of Zeeman energy Δ_Z. There are only weak features associated with the topological phase transition. Unlike the pronounced peak in $\tilde{S}^z_{Lm}$, the component $\tilde{S}^x_{Lm}$ cannot reliably distinguish the trivial from topological phase. The system parameters are chosen to be $\alpha = 0.3$, $\Delta_{SC} = 0.05$, $\mu = 0$, $N = 200$, and $m = 100$.

4.B Local properties of boundary spin component $\tilde{S}^z_{Lm}$

We would like to elaborate on the question in which sense $\tilde{S}^z_{Lm}$ is a *local* signature emerging only at the end of the NW. In other words, we should investigate the behavior of $\tilde{S}^z_{Lm}$ with respect to changes in m, see Fig. 4.8. Far from the topological phase transition, we observe that $\tilde{S}^z_{Lm}$ converges very quickly with increasing m and is therefore a local property of the end of the NW. As we approach the transition point, values for the respective m's start to differ. Nevertheless, even for $m = 20$ we still observe a well-pronounced peak almost at the same Δ_Z as for $m = 100$. Based on that we can conclude that $\tilde{S}^z_{Lm}$ is a local quantity with main support at the end of the NW.

For completeness, we also show that the signature of the topological phase transition in $\tilde{S}^z_{Lm}$ does not crucially depend on a large value of the SOI strength, see Fig. 4.9. Indeed, the peak is even more pronounced in the regime of weak SOI.

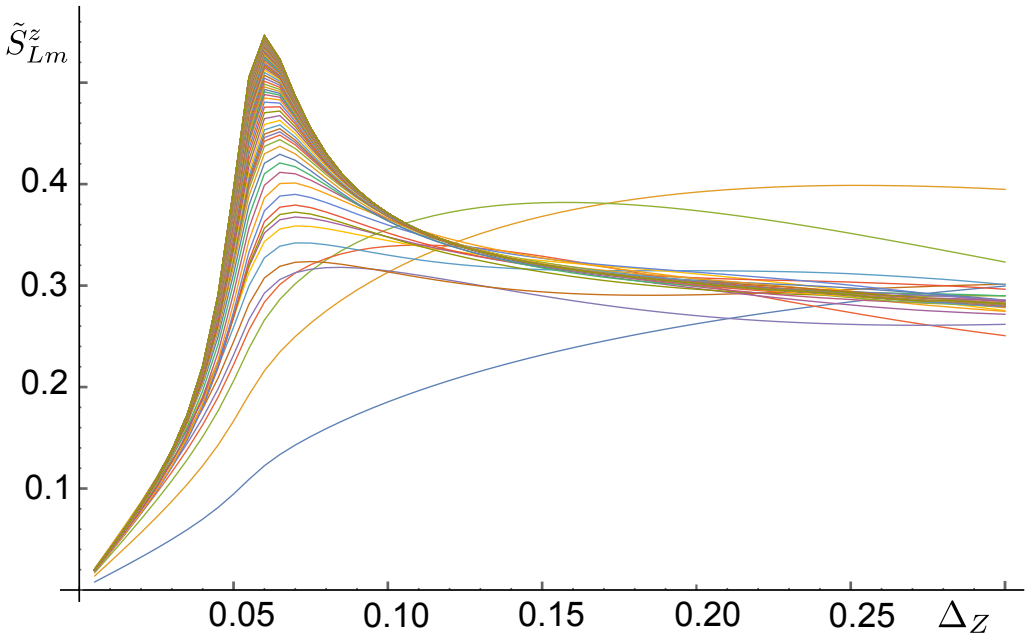

Figure 4.8: Component of the boundary spin along z axis, $\tilde{S}^z_{Lm}$, [see Eq. (4.4)] as a function of Zeeman energy Δ_Z for different cut-off values: $m = 1, ..., 100$. Here, $m = 1$ corresponds to the lowest blue curve. Other curves are ordered according to ascending m at small Δ_Z. The peak in $\tilde{S}^z_{Lm}$ close to Δ^c_Z is observed already for $m = \xi_{SC}/a$ ($\xi_{SC}/a = 12$ for this plot), thus, the proposed signature of the topological phase transition is local with contributions coming from the occupied bulk states at the end of the NW. The system parameters are chosen to be $N = 200$, $\alpha = 0.3$, $\Delta_{SC} = 0.05$, and $\mu = 0$.

4.C Effect of on-site disorder - stability of topological phase transition signature in $\tilde{S}^z_{Lm}$

To demonstrate that the presented signature of the topological phase transition in the boundary spin component $\tilde{S}^z_{Lm}$ is robust, we must verify that this signature persists even if the disorder is present, see Fig. 4.10. We perform the same calculations as before, however, add fluctuations in the chemical potential. We see that, locally, disorder causes the appearance of a similar feature in the spin density as already observed at the NW ends. Namely, there is a local maximum in the spin density S^z_j at

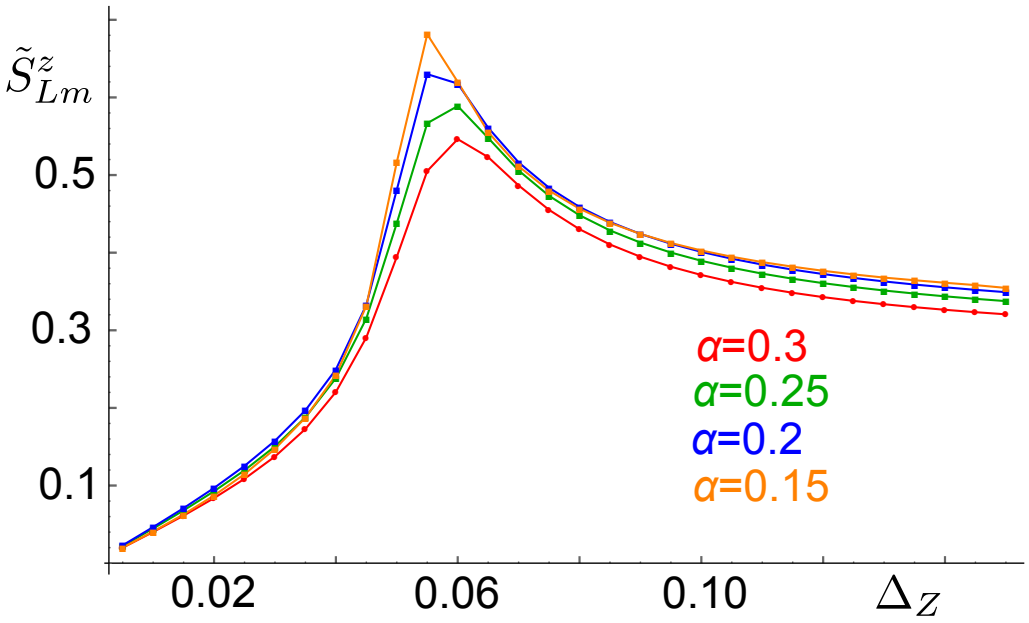

Figure 4.9: Component of the boundary spin along z axis, $\tilde{S}^z_{Lm}$, [see Eq. (4.4)] as a function of Zeeman energy Δ_Z for different values of SOI. We compare the experimentally relevant regime of strong SOI (red), $\alpha = 0.3$, with intermediate SOI regimes, $\alpha = 0.25$ (green) and $\alpha = 0.2$ (blue), as well as with weak SOI regime, $\alpha = 0.15$ (orange). The peak gets even more pronounced as one tunes from strong to weak SOI regime. The system parameters are chosen to be $N = 200$, $\Delta_{SC} = 0.05$, $m = 100$ and $\mu = 0$.

the position of the impurity. The oscillations around the impurity position decay as one moves away. If there are many impurities, such effects will average out. As a result, there can be only local redistribution of the spin density S^z_j, which do not affect the boundary spin $\tilde{S}^z_{Lm}$. Therefore, as expected, the signature of the topological phase transition, *i.e.* peak in $\tilde{S}^z_{Lm}$ at Δ^c_Z, is robust against local disorder. This holds also in the case of disorder as strong as the superconducting gap Δ_{SC} itself and well beyond.

Next, we add magnetic disorder. A magnetic impurity at site j pointing in arbitrary direction defined by two spherical angles (θ, ϕ) is mod-

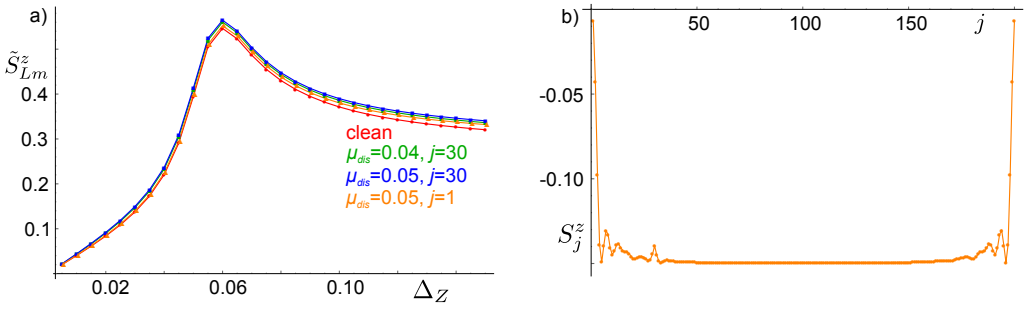

Figure 4.10: (a) Component of the boundary spin, $\tilde{S}^z_{Lm}$, and (b) the z-component of the local spin density S^z_j in the system with on-site potential disorder. Generally, we observe the same behavior as in the clean case, accompanied by small overall renormalization of $\tilde{S}^z_j$ even in the case of relatively strong disorder. We add disorder in the chemical potential μ_{dis} on site j, elsewhere, we keep $\mu = 0$. In panel (a), $\tilde{S}^z_{Lm}$ for the clean wire (red) is compared with results for a disordered wire with $\mu_{dis} = 0.04$ at site $j = 30$ (green); with $\mu_{dis} = 0.05$ at site $j = 30$ (blue); and with $\mu_{dis} = 0.04$ at site $j = 1$ (orange). If an impurity located at the first site of the NW, the boundary spin is left unchanged even for very strong values of disorder, $\mu_{dis} = 0.1$. The signature of the topological phase transition is clearly not affected by disorder. In panel (b), S^z_j is shown for a disordered NW with $\mu_{dis} = 0.04$ at site $j = 30$ ($\Delta_Z = 0.07$). The presence of the impurity manifests itself as an additional local peak in S^z_j accompanied by spatial oscillations. As a result, there is a local redistribution of the spin density, which does not affect the boundary spin. If there are several impurities, their contributions average out and the system gets even more stable to disorder. The system parameters are chosen to be $N = 200$, $\alpha = 0.3$, $\Delta_{SC} = 0.05$, and $m = 100$.

eled by adding the following term to the total Hamiltonian H,

$$H_{MI,j} = J \sum_{\sigma,\sigma'} c^\dagger_{j\sigma} \Big(\sin\theta \cos\phi \, \sigma_x^{\sigma\sigma'} + \sin\theta \sin\phi \, \sigma_y^{\sigma\sigma'} + \cos\theta \, \sigma_z^{\sigma\sigma'} \Big) c_{j\sigma'}. \tag{4.7}$$

We repeat the same procedure as described before for potential disorder and again compare the results with the case of the clean wire, see Fig. 4.11. In case of a magnetic impurity pointing in the z direction along (opposite to) the direction of magnetic field, there is a dip (peak) in the local spin density. Such an effective local magnetic field sums up with the

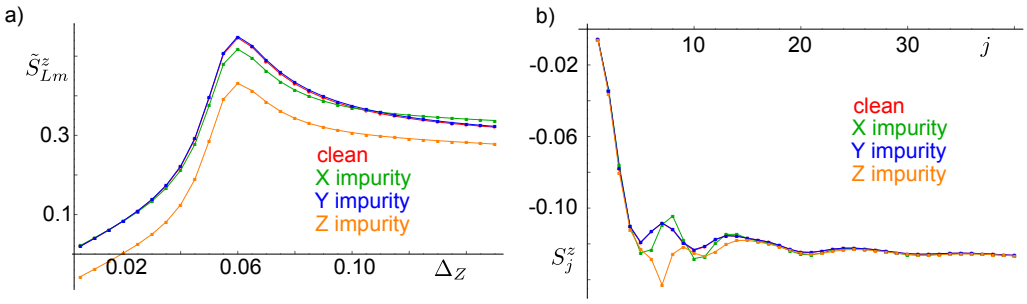

Figure 4.11: (a) Component of the boundary spin, $\tilde{S}^z_{Lm}$, and (b) the z-component of the local spin density S^z_j in the presence of on-site magnetic disorder. Generally, we observe the same behavior as in the clean case accompanied by small overall renormalization of $\tilde{S}^z_{Lm}$. (a) Boundary spin $\tilde{S}^z_{Lm}$ for the clean wire (red) is compared with results for a disordered wire with a magnetic impurity of the strength $J = 0.05$ placed at site $j = 7$ in different configurations: polarization along the x direction (green) with $\theta = \pi/2$, $\phi = 0$; polarization along the y direction (blue) with $\theta = \pi/2$, $\phi = \pi/2$; polarization along the z direction (orange) with $\theta = 0$. (b) Close to the magnetic impurity, the local spin density S^z_j is changed, resulting in either an increase or decrease in the local spin polarization ($\Delta_Z = 0.06$). This local redistribution of the spin density hardly affects the boundary spin and does not obscure the signature of the topological phase transition. If there are several magnetic impurities, their contributions average out. The system parameters are chosen to be $N = 200$, $\alpha = 0.3$, $\Delta_{SC} = 0.05$, and $m = 100$ if not specified otherwise.

externally applied uniform field and increases (decreases) the total spin polarization, and, thus, affects the height but not the position of the peak in the boundary spin. In the case of the magnetic impurity pointing along the x direction, there is a peak in the local spin density. This can be understood as follows: the local magnetic field polarizes spins locally along the x direction, and, thus, diminishes the polarization in the z direction, resulting in a local peak. In the case of a magnetic impurity pointing along the y direction, there are practically no changes in the local spin density of states nor in the boundary spin. If the magnetic impurity is far away from the boundary, there is no effect on the boundary spin. In case of multiple magnetic impurities such effects average out. To conclude, magnetic disorder does not affect the signature of the topological phase transition carried by the boundary spin.

4.D Boundary spin $\tilde{S}^z_{Rm}$ at the boundary between topological and trivial phases

In the main text, we have focused on the boundary spin located at the ends of the NW. Here, we show that, generally, the boundary spin is associated with the boundary between topological and trivial sections in the NW. As a result, there is a contribution to $\tilde{S}^z_{L/Rm}$ coming from both sides of the boundary, *i.e.* from the topological section and from the trivial section. This means that the definitions for $\tilde{S}^z_{R/Lm}$ given by Eqs. (4) and (6) should be generalized. For the moment, let us focus on the boundary located at the site N and introduce the boundary spin as

$$\tilde{S}^z_{Bm} = \sum_{j=N-m_<}^{N} \left(S^z_j - S^z_{0<}\right) - \sum_{j=N+1}^{N+m_>} \left(S^z_j - S^z_{0>}\right),$$
$$S^z_{0<} = S^z_{j=[\frac{N_<}{2}]}, \quad S^z_{0>} = S^z_{j=[N_<+\frac{N_>}{2}]}. \tag{4.8}$$

Here, the sum runs over $m_<$ ($m_>$) sites of the left (right) section of the NW consisting in total of $N_<$ ($N_>$) sites, such that $m = m_< + m_>$. Without loss of generality, we can assume that the left (right) section is in the topological (trivial) phase. Assuming that both sections are long enough, one determines the bulk value of the spin density as $S^z_{0<}$ and $S^z_{0>}$ for each section separately, as they are generally not the same. This can be seen clearly in Figs. 4.13(b) and 4.12(b), where we show how a typical spin density profile looks like in NWs divided into two sections.

We consider two scenarios. In the first scenario (see Fig. 4.12), we attach a superconducting lead at the right end of the NW. In this lead, we assume that the Zeeman field is screened and the SOI is absent. As a result, this NW section is always in the trivial phase. Again, one observes a well-pronounced peak in $\tilde{S}^z_{Bm}$ at Zeeman energies close to the critical value Δ^c_Z. In the second scenario (see Fig. 4.13), the right section of the NW has stronger proximity-induced superconductivity. Thus, it enters the topological phase at larger values of Zeeman energy. As a result, there are two peaks in $\tilde{S}^z_{Bm}$. The first (second) peak corresponds to a Zeeman energy at which left (right) section of the NW becomes topological.

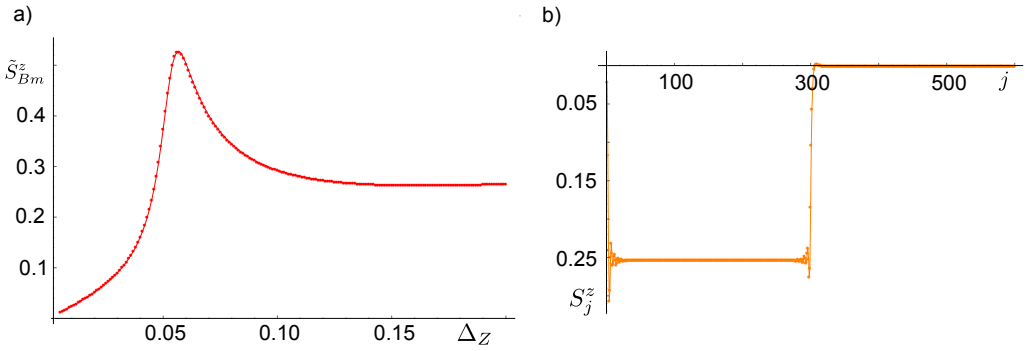

Figure 4.12: (a) Component of the boundary spin, $\tilde{S}^z_{Bm}$, and (b) the z-component of the local spin density S^z_j. The right section of the NW corresponds to a superconducting lead, in which we fix $\alpha = \Delta_Z = 0$. In contrast to that, the left section of the NW is described by $\alpha = 0.3$. The chemical potential is uniform, $\mu = 0$, as well as the superconducting strength $\Delta_{SC} = 0.05$. In addition, $N_< = N_> = 300$ and $m_< = m_> = 150$. (a) Again, there is a signature of the topological phase transition in $\tilde{S}^z_{Bm}$. (b) The boundary spin has contributions from both topological and trivial sections of the NW ($\Delta_Z = 0.15$). We also note that the bulk values of spin density S^z_j are different in two sections.

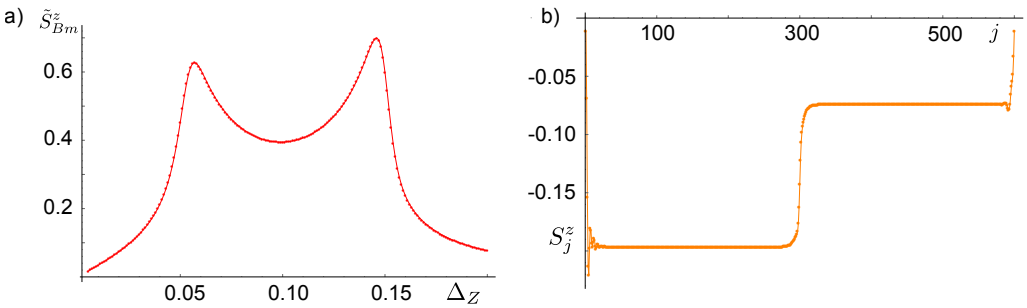

Figure 4.13: The same as in Fig. 4.12, however, here, both sections of the NW have the same strength of the SOI ($\alpha = 0.3$) and the same strength of Zeeman energy. However, the proximity-gap is non-uniform: *i.e.* the right (left) section has $\Delta_{SC} = 0.15$ ($\Delta_{SC} = 0.05$). As a result, in panel (a), there are two peaks in $\tilde{S}^z_{Bm}$, which corresponds to two values at which each of sections changes from the trivial to the topological phase. (b) The z-component of the local spin density S^z_j saturates at two different values at the left and right sections, which motivates us to introduce $S^z_{0<}$ and $S^z_{0>}$ for each section separately ($\Delta_Z = 0.10$).

4.E Signatures of topological phase transition in bulk values of spin

So far we have focused on signatures of the topological phase transition to be detected in the boundary spin. However, the bulk values of the spin polarization along the magnetic field, S_0^z, also carries the information about the phase transition in finite-size systems. To focus on bulk properties only and to exclude any influence of boundary effects, we impose now periodic boundary conditions on the system, forming a NW ring. In this case the system is translationally invariant and it does not matter at which point one computes the bulk value of the spin polarization S_{PBC}^z. In finite-size systems, we always observe a sharp discontinuity in S_{PBC}^z at the point of the topological phase transition, $\Delta_Z = \Delta_Z^c$, see Fig. 4.14. In contrast to the boundary spin, this discontinuity always takes place at Δ_Z^c independent of the system size. However, the value of the jump ΔS_{PBC}^z in S_{PBC}^z depends on the size of the system. We analyzed the value of the jump as a function of system size N and conclude that it can be fitted best by an $1/N$ dependence. We note that the results of this subsection obtained for bulk states with periodic boundary conditions are closely related to the ones obtained for bulk states in Ref. [185]. In particular, the sign reversal of the spin polarization of the bulk state with zero momentum is responsible for the jump in S_{PBC}^z. In stark contrast, the features of the boundary spin $\tilde{S}_{Bm}^z$ are due to boundary effects and thus are of different physical origin.

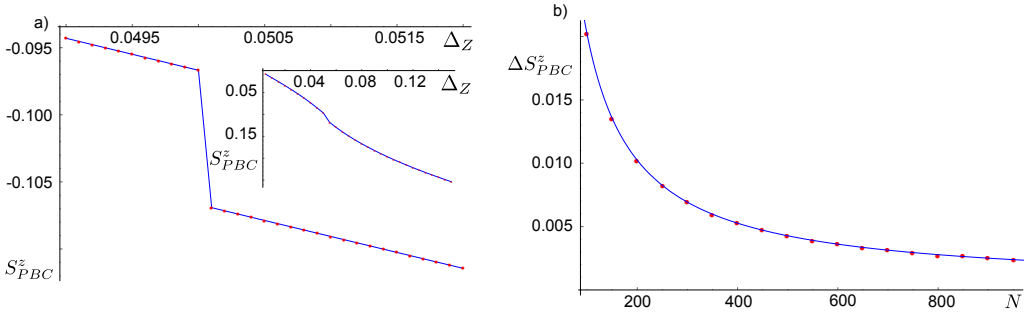

Figure 4.14: (a) Component of spin polarization along the z axis, S^z_{PBC}, as a function of Zeeman energy in the system with periodic boundary conditions. Away from the topological phase transition point Δ^c_Z, S^z_{PBC} is a linear function of Δ_Z. The discontinuity in spin polarization, ΔS^z_{PBC}, occurs exactly at Δ^c_Z. (b) The size of the jump ΔS^z_{PBC} is inversely proportional to the system size N. Numerical results (red dots) are fitted by the analytical formula $\Delta S^z_{PBC} \propto 1/N$ (blue curve). The system parameters are chosen to be $\alpha = 0.3$, $\Delta_{SC} = 0.05$, $\mu = 0$, and $m = N/2$

Bibliography

[1] R. Feynman, "Simulating physics with computers," *International Journal of Theoretical Physics*, vol. 21, no. 6-7, pp. 467–488, 1982.

[2] https://en.wikipedia.org/wiki/File:Bloch_Sphere.svg.

[3] D. DiVincenzo, "Topics in quantum computers," *arXiv:cond-mat/9612126*.

[4] G. Wendin, "Quantum information processing with superconducting circuits: a review," *Reports on Progress in Physics*, vol. 80, no. 10, p. 106001, 2017.

[5] K. R. Brown, J. Kim, and C. Monroe, "Co-designing a scalable quantum computer with trapped atomic ions," *Npj Quantum Information*, vol. 2, p. 16034, 11 2016.

[6] C. Kloeffel and D. Loss, "Prospects for spin-based quantum computing in quantum dots," *Annual Review of Condensed Matter Physics*, vol. 4, no. 1, pp. 51–81, 2013.

[7] D. Loss and D. P. DiVincenzo, "Quantum computation with quantum dots," *Phys. Rev. A*, vol. 57, pp. 120–126, 1998.

[8] M. Veldhorst, H. G. J. Eenink, C. H. Yang, and A. S. Dzurak, "Silicon cmos architecture for a spin-based quantum computer," *Nature Communications*, vol. 8, no. 1, p. 1766, 2017.

[9] P. Shor, "Polynomial-time algorithms for prime factorization and discrete logarithms on a quantum computer," *SIAM Review*, vol. 41, no. 2, pp. 303–332, 1999.

[10] L. K. Grover, "A fast quantum mechanical algorithm for database search," *arXiv:quant-ph/9605043*.

[11] A. Montanaro, "Quantum algorithms: an overview," *Npj Quantum Information*, vol. 2, pp. 15023 EP –, 01 2016.

[12] T. Ando, A. B. Fowler, and F. Stern, "Electronic properties of two-dimensional systems," *Rev. Mod. Phys.*, vol. 54, pp. 437–672, 1982.

[13] E. P. Nordberg, G. A. T. Eyck, H. L. Stalford, R. P. Muller, R. W. Young, K. Eng, L. A. Tracy, K. D. Childs, J. R. Wendt, R. K. Grubbs, J. Stevens, M. P. Lilly, M. A. Eriksson, and M. S. Carroll, "Enhancement-mode double-top-gated metal-oxide-semiconductor nanostructures with tunable lateral geometry," *Phys. Rev. B*, vol. 80, p. 115331, Sep 2009.

[14] https://en.wikipedia.org/wiki/File:MOS_Capacitor.svg.

[15] V. Umansky, M. Heiblum, Y. Levinson, J. Smet, J. Nübler, and M. Dolev, "Mbe growth of ultra-low disorder 2deg with mobility exceeding 35x106cm2/vs," *Journal of Crystal Growth*, vol. 311, no. 7, pp. 1658 – 1661, 2009. International Conference on Molecular Beam Epitaxy (MBE-XV).

[16] https://en.wikipedia.org/wiki/File:HEMT-band_structure_scheme en.svg.

[17] N. P. Dasgupta, J. Sun, C. Liu, S. Brittman, S. C. Andrews, J. Lim, H. Gao, R. Yan, and P. Yang, "25th anniversary article: Semiconductor nanowires – synthesis, characterization, and applications," *Advanced Materials*, vol. 26, no. 14, pp. 2137–2184, 2014.

[18] M. Royo, M. D. Luca, R. Rurali, and I. Zardo, "A review on iii–v core–multishell nanowires: growth, properties, and applications," *Journal of Physics D: Applied Physics*, vol. 50, no. 14, p. 143001, 2017.

[19] J. Fabian, A. Matos-Abiague, C. Ertler, P. Stano, and I. Zutic, "Semiconductor spintronics," *Acta Physica Slovaca*, vol. 57, pp. 565–907, 2007.

[20] D. F. Koster, J. O. Dimmock, R. G. Wheeler, and H. Statz, *Properties of the Thirty-Two Point Groups*. MIT Press, 1963.

[21] E. O. Kane, "Band structure of indium antimonide," *Journal of Physics and Chemistry of Solids*, vol. 1, no. 4, pp. 249 – 261, 1957.

[22] G. L. Bir and G. E. Pikus, *Symmetry and Strain-Induced Effects in Semiconductors*. Wiley, 1974.

[23] M. Braun and U. Rössler, "Magneto-optic transitions and nonparabolicity parameters in the conduction band of semiconductors," *Journal of Physics C: Solid State Physics*, vol. 18, no. 17, p. 3365, 1985.

[24] O. Zitouni, K. Boujdaria, and H. Bouchriha, "Band parameters for gaas and si in the 24-k.p model," *Semiconductor Science and Technology*, vol. 20, no. 9, p. 908, 2005.

[25] M. Nielsen and I. Chuang, *Quantum Computation and Quantum Information*. Cambridge University Press, 2016.

[26] R. Hanson, L. P. Kouwenhoven, J. R. Petta, S. Tarucha, and L. M. K. Vandersypen, "Spins in few-electron quantum dots," *Rev. Mod. Phys.*, vol. 79, pp. 1217–1265, 2007.

[27] T. A. Baart, P. T. Eendebak, C. Reichl, W. Wegscheider, and L. M. K. Vandersypen, "Computer-automated tuning of semiconductor double quantum dots into the single-electron regime," *Applied Physics Letters*, vol. 108, no. 21, p. 213104, 2016.

[28] S. Bednarek, B. Szafran, and J. Adamowski, "Solution of the poisson-schrödinger problem for a single-electron transistor," *Phys. Rev. B*, vol. 61, pp. 4461–4464, 2000.

[29] F. A. Zwanenburg, A. S. Dzurak, A. Morello, M. Y. Simmons, L. C. L. Hollenberg, G. Klimeck, S. Rogge, S. N. Coppersmith, and M. A. Eriksson, "Silicon quantum electronics," *Rev. Mod. Phys.*, vol. 85, pp. 961–1019, 2013.

[30] M. Veldhorst, C. H. Yang, J. C. C. Hwang, W. Huang, J. P. Dehollain, J. T. Muhonen, S. Simmons, A. Laucht, F. E. Hudson, K. M. Itoh, A. Morello, and A. S. Dzurak, "A two-qubit logic gate in silicon," *Nature*, vol. 526, p. 410, 10 2015.

[31] M. Sato and Y. Ando, "Topological superconductors: a review," *Reports on Progress in Physics*, vol. 80, no. 7, p. 076501, 2017.

[32] D. J. Thouless, M. Kohmoto, M. P. Nightingale, and M. den Nijs, "Quantized hall conductance in a two-dimensional periodic potential," *Phys. Rev. Lett.*, vol. 49, pp. 405–408, 1982.

[33] A. P. Schnyder, S. Ryu, A. Furusaki, and A. W. W. Ludwig, "Classification of topological insulators and superconductors in three spatial dimensions," *Phys. Rev. B*, vol. 78, p. 195125, 2008.

[34] A. Altland and M. R. Zirnbauer, "Nonstandard symmetry classes in mesoscopic normal-superconducting hybrid structures," *Phys. Rev. B*, vol. 55, pp. 1142–1161, 1997.

[35] A. Y. Kitaev, "Unpaired majorana fermions in quantum wires," *Physics-Uspekhi*, vol. 44, no. 10S, p. 131, 2001.

[36] M. Leijnse and K. Flensberg, "Introduction to topological superconductivity and majorana fermions," *Semiconductor Science and Technology*, vol. 27, no. 12, p. 124003, 2012.

[37] E. Majorana, "Teoria simmetrica dell'elettrone e del positrone," *Nuovo Cimento*, vol. 14, no. 4, p. 171, 1937.

[38] F. Wilczek, "Majorana returns," *Nature Physics*, vol. 5, pp. 614 EP –, 09 2009.

[39] Y. Oreg, G. Refael, and F. von Oppen, "Helical liquids and majorana bound states in quantum wires," *Phys. Rev. Lett.*, vol. 105, p. 177002, 2010.

[40] J. Klinovaja and D. Loss, "Composite majorana fermion wave functions in nanowires," *Phys. Rev. B*, vol. 86, p. 085408, 2012.

[41] H. Zhang, C.-X. Liu, S. Gazibegovic, D. Xu, J. A. Logan, G. Wang, N. van Loo, J. D. S. Bommer, M. W. A. de Moor, D. Car, R. L. M. Op het Veld, P. J. van Veldhoven, S. Koelling, M. A. Verheijen, M. Pendharkar, D. J. Pennachio, B. Shojaei, J. S. Lee, C. J. Palmstrøm, E. P. A. M. Bakkers, S. D. Sarma, and L. P. Kouwenhoven, "Quantized majorana conductance," *Nature*, vol. 556, pp. 74 EP –, 03 2018.

[42] W. G. van der Wiel, S. De Franceschi, J. M. Elzerman, T. Fujisawa, S. Tarucha, and L. P. Kouwenhoven, "Electron transport through double quantum dots," *Rev. Mod. Phys.*, vol. 75, pp. 1–22, 2002.

[43] R. Maurand, X. Jehl, D. Kotekar-Patil, A. Corna, H. Bohuslavskyi, R. Laviéville, L. Hutin, S. Barraud, M. Vinet, M. Sanquer, and S. De Franceschi, "A cmos silicon spin qubit," *Nature Communications*, vol. 7, p. 13575, 2016.

[44] M. Veldhorst, H. Eenink, C. Yang, and A. Dzurak, "Silicon cmos architecture for a spin-based quantum computer," *arXiv:1609.09700*.

[45] Z. Shi, C. B. Simmons, J. R. Prance, J. K. Gamble, T. S. Koh, Y.-P. Shim, X. Hu, D. E. Savage, M. G. Lagally, M. A. Eriksson, M. Friesen, and S. N. Coppersmith, "Fast hybrid silicon double-quantum-dot qubit," *Phys. Rev. Lett.*, vol. 108, p. 140503, 2012.

[46] T. S. Koh, J. K. Gamble, M. Friesen, M. A. Eriksson, and S. N. Coppersmith, "Pulse-gated quantum-dot hybrid qubit," *Phys. Rev. Lett.*, vol. 109, p. 250503, 2012.

[47] D. Kim, D. R. Ward, C. B. Simmons, J. K. Gamble, R. Blume-Kohout, E. Nielsen, D. E. Savage, M. G. Lagally, M. Friesen, S. N. Coppersmith, and M. A. Eriksson, "Microwave-driven coherent operation of a semiconductor quantum dot charge qubit," *Nat. Nano.*, vol. 10, pp. 243–247, 2015.

[48] D. Kim, D. R. Ward, C. B. Simmons, D. E. Savage, M. G. Lagally, M. Friesen, S. N. Coppersmith, and M. A. Eriksson, "High-fidelity resonant gating of a silicon-based quantum dot hybrid qubit," *Npj Quant. Inf.*, vol. 1, p. 15004, 2015.

[49] L. Trifunovic, O. Dial, M. Trif, J. R. Wootton, R. Abebe, A. Yacoby, and D. Loss, "Long-distance spin-spin coupling via floating gates," *Phys. Rev. X*, vol. 2, p. 011006, 2012.

[50] J. R. Petta, A. C. Johnson, J. M. Taylor, E. A. Laird, A. Yacoby, M. D. Lukin, C. M. Marcus, M. P. Hanson, and A. C. Gossard, "Coherent manipulation of coupled electron spins in semiconductor quantum dots," *Science*, vol. 309, no. 5744, pp. 2180–2184, 2005.

[51] B. M. Maune, M. G. Borselli, B. Huang, T. D. Ladd, P. W. Deelman, K. S. Holabird, A. A. Kiselev, I. Alvarado-Rodriguez, R. S. Ross, A. E. Schmitz, M. Sokolich, C. A. Watson, M. F. Gyure, and A. T. Hunter, "Spins in few-electron quantum dots," *Nature*, vol. 481, pp. 344–347, 2012.

[52] J. Levy, "Universal quantum computation with spin-$1/2$ pairs and heisenberg exchange," *Phys. Rev. Lett.*, vol. 89, p. 147902, 2002.

[53] H. Bluhm, S. Foletti, I. Neder, M. Rudner, D. Mahalu, V. Umansky, and A. Yacoby, "Dephasing time of gaas electron-spin qubits

coupled to a nuclear bath exceeding 200μs," *Nature Physics*, vol. 7, p. 109, 2011.

[54] F. H. L. Koppens, C. Buizert, K. J. Tielrooij, I. T. Vink, K. C. Nowack, T. Meunier, L. P. Kouwenhoven, and L. M. K. Vandersypen, "Driven coherent oscillations of a single electron spin in a quantum dot," *Nature*, vol. 442, pp. 766–771, 2006.

[55] A. Barenco, C. H. Bennett, R. Cleve, D. P. DiVincenzo, N. Margolus, P. Shor, T. Sleator, J. A. Smolin, and H. Weinfurter, "Elementary gates for quantum computation," *Phys. Rev. A*, vol. 52, pp. 3457–3467, 1995.

[56] J. C.-E. Sten, "Ellipsoidal harmonics and their application in electrostatics," *Journal of Electrostatics*, vol. 64, no. 10, pp. 647 – 654, 2006.

[57] G. Burkard, D. Loss, and D. P. DiVincenzo, "Coupled quantum dots as quantum gates," *Phys. Rev. B*, vol. 59, pp. 2070–2078, 1999.

[58] In a 2D parabolic potential with circular symmetry, there are two degenerate orbital states that correspond to a first excited state. We assume here that this degeneracy is lifted and consider only one excited state, which is justified because asymmetries in the DQD potential can be generated electrically with the gates that control the in-plane confinement.

[59] N. Schuch and J. Siewert, "Natural two-qubit gate for quantum computation using the XY interaction," *Phys. Rev. A*, vol. 67, p. 032301, 2003.

[60] T. Hiltunen, H. Bluhm, S. Mehl, and A. Harju, "Charge-noise tolerant exchange gates of singlet-triplet qubits in asymmetric double quantum dots," *Phys. Rev. B*, vol. 91, p. 075301, 2015.

[61] M. Trif, V. Golovach, and D. Loss, "Spin-spin coupling in electrostatically coupled quantum dots," *Phys. Rev. B*, vol. 75, p. 085307, 2007.

[62] L. P. Kouwenhoven, D. G. Austing, and S. Tarucha, "Few-electron quantum dots," *Rep. Prog. Phys.*, vol. 64, no. 6, p. 701, 2001.

[63] M. D. Shulman, O. E. Dial, S. P. Harvey, H. Bluhm, V. Umansky, and A. Yacoby, "Demonstration of entanglement of electrostatically coupled singlet-triplet qubits," *Science*, vol. 336, no. 6078, pp. 202–205, 2012.

[64] F. Martins, F. K. Malinowski, P. D. Nissen, E. Barnes, S. Fallahi, G. C. Gardner, M. J. Manfra, C. M. Marcus, and F. Kuemmeth, "Noise suppression using symmetric exchange gates in spin qubits," *Phys. Rev. Lett.*, vol. 116, p. 116801, 2016.

[65] W. Knap, C. Skierbiszewski, A. Zduniak, E. Litwin-Staszewska, D. Bertho, F. Kobbi, J. L. Robert, G. E. Pikus, F. G. Pikus, S. V. Iordanskii, V. Mosser, K. Zekentes, and Y. B. Lyanda-Geller, "Weak antilocalization and spin precession in quantum wells," *Phys. Rev. B*, vol. 53, pp. 3912–3924, 1996.

[66] C. Tahan and R. Joynt, "Rashba spin-orbit coupling and spin relaxation in silicon quantum wells," *Phys. Rev. B*, vol. 71, p. 075315, 2005.

[67] H. Malissa, W. Jantsch, M. Mühlberger, F. Schäffler, Z. Wilamowski, M. Draxler, and P. Bauer, "Bychkov-rashba effect and g-factor tuning in modulation doped sige quantum wells," *Acta Physica Polonica A*, vol. 105, no. 6, pp. 585–590, 2004.

[68] E. A. Laird, C. Barthel, E. I. Rashba, C. M. Marcus, M. P. Hanson, and A. C. Gossard, "Hyperfine-mediated gate-driven electron spin resonance," *Phys. Rev. Lett.*, vol. 99, p. 246601, 2007.

[69] M. Pioro-Ladriere, T. Obata, Y. Tokura, Y.-S. Shin, T. Kubo, K. Yoshida, T. Taniyama, and S. Tarucha, "Electrically driven single-electron spin resonance in a slanting zeeman field," *Nature Physics*, vol. 4, no. 10, pp. 776–779, 2008.

[70] T. Takakura, M. Pioro-Ladrière, T. Obata, Y.-S. Shin, R. Brunner, K. Yoshida, T. Taniyama, and S. Tarucha, "Triple quantum dot device designed for three spin qubits," *Applied Physics Letters*, vol. 97, no. 21, 2010.

[71] I. L. Aleiner and V. I. Fal'ko, "Spin-orbit coupling effects on quantum transport in lateral semiconductor dots," *Phys. Rev. Lett.*, vol. 87, p. 256801, 2001.

[72] V. N. Golovach, A. Khaetskii, and D. Loss, "Phonon-induced decay of the electron spin in quantum dots," *Phys. Rev. Lett.*, vol. 93, p. 016601, 2004.

[73] P. Stano and J. Fabian, "Theory of phonon-induced spin relaxation in laterally coupled quantum dots," *Phys. Rev. Lett.*, vol. 96, p. 186602, 2006.

[74] S. Goswami, K. Slinker, M. Friesen, L. McGuire, J. Truitt, C. Tahan, L. Klein, J. Chu, P. Mooney, D. W. Van Der Weide, R. Joynt, S. N. Coppersmith, and M. A. Eriksson, "Controllable valley splitting in silicon quantum devices," *Nature Physics*, vol. 3, no. 1, pp. 41–45, 2007.

[75] M. Xiao, M. G. House, and H. W. Jiang, "Parallel spin filling and energy spectroscopy in few-electron si metal-on-semiconductor-based quantum dots," *Applied Physics Letters*, vol. 97, no. 3, p. 032103, 2010.

[76] C. H. Yang, A. Rossi, R. Ruskov, N. S. Lai, F. A. Mohiyaddin, S. Lee, C. Tahan, G. Klimeck, A. Morello, and A. S. Dzurak, "Spin-valley lifetimes in a silicon quantum dot with tunable valley splitting," *Nat. Commun.*, vol. 4, p. 2096, 2013.

[77] Our formula differs from the one given in Ref. [49] by a factor of 1/2. For the details see Appendix 2.A.

[78] L. D. Landau and E. M. Lifshitz, *Electrodynamics of Continuous Media*. Pergamon Press, 1960.

[79] M. R. Delbecq, T. Nakajima, P. Stano, T. Otsuka, S. Amaha, J. Yoneda, K. Takeda, G. Allison, A. Ludwig, A. D. Wieck, S. Tarucha, *Quantum dephasing in a gated GaAs triple quantum dot due to non-ergodic noise*, Phys. Rev. Lett. **116**, 046802 (2016).

[80] T. Nakajima, M. R. Delbecq, T. Otsuka, P. Stano, S. Amaha, J. Yoneda, A. Noiri, K. Kawasaki, K. Takeda, G. Allison, A. Ludwig, A. D. Wieck, D. Loss, S. Tarucha, *Robust single-shot measurement of spin correlations using a metastable charge state in a quantum dot array*, Phys. Rev. Lett. **119**, 017701 (2017).

[81] A. Hofmann, V. F. Maisi, T. Krähenmann, C. Reichl, W. Wegscheider, K. Ensslin, and T. Ihn, *Anisotropy and Suppression of Spin-Orbit*

Interaction in a GaAs Double Quantum Dot, Phys. Rev. Lett. **119**, 176807 (2017).

[82] F. K. Malinowski, F. Martins, P. D. Nissen, E. Barnes, L. Cywiński, M. S. Rudner, S. Fallahi, G. C. Gardner, M. J. Manfra, C. M. Marcus, F. Kuemmeth, *Notch filtering the nuclear environment of a spin qubit*, Nat. Nanotech., **12**,16 (2017).

[83] T. Botzem, R. P. G. McNeil, J.-M. Mol, D. Schuh, D. Bougeard, H. Bluhm, *Quadrupolar and anisotropy effects on dephasing in two-electron spin qubits in GaAs*, Nat. Commun. **7**, 11170 (2016).

[84] J. M. Nichol, L. A. Orona, S. P. Harvey, S. Fallahi, G. C. Gardner, M. J. Manfra, and A. Yacoby, *High-fidelity entangling gate for double-quantum-dot spin qubits*, npj Quant. Inf. **3**, 3 (2017).

[85] J. Yoneda, K. Takeda, T. Otsuka, T. Nakajima, M. R. Delbecq, G. Allison, T. Honda, T. Kodera, S. Oda, Y. Hoshi, N. Usami, K. M. Itoh, S. Tarucha, *A ¿99.9%-fidelity quantum-dot spin qubit with coherence limited by charge noise*, Nat. Nanotech. **13**, 102 (2018).

[86] D. M. Zajac, T. M. Hazard, X. Mi, E. Nielsen, and J. R. Petta, *Scalable gate architecture for a one-dimensional array of semiconductor spin qubits*, Phys. Rev. Appl. **6**, 054013 (2016).

[87] T.-Y. Yang, A. Andreev, Y. Yamaoka, T. Ferrus, S. Oda, T. Kodera, D. A. Williams, *Quantum information processing in a silicon-based system*, Tech. Digest Of Ieee International Electron Devices Meeting (iedm), p850 (2016).

[88] F. Watson, S. G. J. Philips, E. Kawakami, D. R. Ward, P. Scarlino, M. Veldhorst, D. E. Savage, M. G. Lagally, Mark Friesen, S. N. Coppersmith, M. A. Eriksson, L. M. K. Vandersypen, *A programmable two-qubit quantum processor in silicon*, Nature **555**, 633 (2018).

[89] M. D. Reed, B. M. Maune, R. W. Andrews, M. G. Borselli, K. Eng, M. P. Jura, A. A. Kiselev, T. D. Ladd, S. T. Merkel, I. Milosavljevic, E. J. Pritchett, M. T. Rakher, R. S. Ross, A. E. Schmitz, A. Smith, J. A. Wright, M. F. Gyure, and A. T. Hunter, *Reduced Sensitivity to Charge Noise in Semiconductor Spin Qubits via Symmetric Operation*, Phys. Rev. Lett. **116**, 110402 (2016).

[90] A. Laucht, R. Kalra, S. Simmons, J. P. Dehollain, J. T. Muhonen, F. A. Mohiyaddin, S. Freer, F. E. Hudson, K. M. Itoh, D. N. Jamieson, J. C. McCallum, A. S. Dzurak, A. Morello, *A Dressed Spin Qubit in Silicon* Nat. Nanotech. 12, 61(2017).

[91] P. Harvey-Collard, N. T. Jacobson, M. Rudolph, J. Dominguez, G. A. Ten Eyck, J. R. Wendt, T. Pluym, J. K. Gamble, M. P. Lilly, M. Pioro-Ladriére, and M. S. Carroll, *Coherent coupling between a quantum dot and a donor in silicon*, Nat. Commun. **8**, 1029 (2017).

[92] N.W. Hendrickx, D.P. Franke, A. Sammak, M. Kouwenhoven, D. Sabbagh, L. Yeoh, R. Li, M.L.V. Tagliaferri, M. Virgilio, G. Capellini, G. Scappucci, M. Veldhorst, *Gate-controlled quantum dots and superconductivity in planar germanium*, arxiv:1801.08869.

[93] H. Watzinger, J. Kukučka, L. Vukušić, F. Gao, T. Wang, F. Schäffler, J.-J. Zhang, G. Katsaros, *Ge hole spin qubit*, arxiv:1802.00395.

[94] M. Eich, R. Pisoni, A. Pally, H. Overweg, A. Kurzmann, Y. Lee, P. Rickhaus, K. Watanabe, T. Taniguchi, K. Ensslin, T. Ihn, *Coupled quantum dots in bilayer graphene*, arxiv:1805.02943.

[95] F. Stern, *Transverse Hall effect in the Electric Quantum Limit* Phys. Rev. **21**, 1687 (1968).

[96] P. Stano, C.-H. Hsu, L. C. Camenzind, L. Yu, D. M. Zumbühl, D. Loss, *Gate-defined quantum dot in a strong in-plane magnetic field: orbital effects* arxiv:1804.00128.

[97] L. C. Camenzind, L. Yu, P. Stano, J. Zimmerman, A. C. Gossard, D. Loss, and D. M. Zumbühl, *Spectroscopy of Quantum-Dot Orbitals with In-Plane Magnetic Fields* arxiv:1804.00162.

[98] L. C. Camenzind, L. Yu, P. Stano, J. Zimmerman, A. C. Gossard, D. Loss, and D. M. Zumbühl, *Hyperfine spin relaxation in a GaAs single electron quantum dot* arxiv:1711.01474.

[99] D. M. Zumbühl, C. M. Marcus, M. P. Hanson, and A. C. Gossard, *Cotunneling Spectroscopy in Few-Electron Quantum Dots*, Phys. Rev. Lett. **93**, 256801 (2004).

[100] R. Hanson, B. Witkamp, L. M. K. Vandersypen, L. H. Willems van Beveren, J. M. Elzerman, and L. P. Kouwenhoven, *Zeeman Energy*

and Spin Relaxation in a One-Electron Quantum Dot, Phys. Rev. Lett. **91**, 196802 (2003).

[101] A. Kogan, S. Amasha, D. Goldhaber-Gordon, G. Granger, M. A. Kastner, and H. Shtrikman, *Measurements of Kondo and Spin Splitting in Single-Electron Transistors*, Phys. Rev. Lett. **93**, 166602 (2004).

[102] M. J. Snelling, G. P. Flinn, A. S. Plaut, R. T. Harley, A. C. Tropper, R. Eccleston, and C. C. Phillips, *Magnetic g factor of electrons in GaAs/$Al_xGa_{1-x}As$ quantum wells*, Phys. Rev. B **44**, 11345 (1991).

[103] K. J. Thomas, J. T. Nicholls, M. Y. Simmons, M. Pepper, D. R. Mace, and D. A. Ritchie, *Possible Spin Polarization in a One-Dimensional Electron Gas*, Phys. Rev. Lett. **77**, 135 (1996).

[104] E. Tutuc, S. Melinte, E. P. De Poortere, M. Shayegan, and R. Winkler, *Role of finite layer thickness in spin polarization of GaAs two-dimensional electrons in strong parallel magnetic fields*, Phys. Rev. B **67**, 241309 (2003).

[105] G. C. La Rocca, Nammee Kim, and S. Rodriguez, *Effect of uniaxial stress on the electron spin resonance in zinc-blende semiconductors*, Phys. Rev. B **38**, 7595 (1988).

[106] B. Kowalski, P. Omling, B. K. Meyer, D. M. Hofmann, C. Wetzel, V. Härle, F. Scholz, and P. Sobkowicz, *Conduction-band spin splitting of type-I $Ga_xIn_{1-x}As$/InP quantum wells*, Phys. Rev. B **49**, 14786(R) (1994).

[107] S. Takahashi, R. S. Deacon, K. Yoshida, A. Oiwa, K. Shibata, K. Hirakawa, Y. Tokura, and S. Tarucha *Large Anisotropy of the Spin-Orbit Interaction in a Single InAs Self-Assembled Quantum Dot*, Phys. Rev. Lett. **104**, 246801 (2010).

[108] S. Takahashi, R. S. Deacon, A. Oiwa, K. Shibata, K. Hirakawa, and S. Tarucha, *Electrically tunable three-dimensional g-factor anisotropy in single InAs self-assembled quantum dots*, Phys. Rev. B **67**, 161302(R) (2013).

[109] V. P. Michal, T. Fujita, T. A. Baart, J. Danon, C. Reichl, W. Wegscheider, L. M. K. Vandersypen, and Y. V. Nazarov, *Non-linear and dot-dependent Zeeman splitting in GaAs/AlGaAs quantum dot arrays*, Phys. Rev. B **97**, 035301 (2018).

[110] D. S. Miserev, and O. P. Sushkov, *Dimensional reduction of the Luttinger Hamiltonian and g-factors of holes in symmetric two-dimensional semiconductor heterostructures*, Phys. Rev. B **95**, 085431 (2017).

[111] L. C. Camenzind, L. Yu, P. Stano, J. Zimmerman, A. C. Gossard, D. Loss, and D. M. Zumbühl, *G-factor paper* arxiv:XXXX.XXXXX.

[112] Zh. A. Devizorova, A. V. Shchepetilnikov, Yu. A. Nefyodov, V. A. Volkov, I. V. Kukushkin, *Interface contributions to the spin-orbit interaction parameters of electrons at the (001) GaAs/AlGaAs interface*, JETP Letters, **100**, 102 (2014).

[113] T. K. Rebane, *The anisotropic harmonic oscillator in a magnetic field*, Theor. Exp. Chem. **5**, 1 (1972).

[114] I. M. Davies, *The propagator for a charged particle in a constant magnetic field and with a quadratic potential*, J. Phys. A: Math. Gen. **18**, 2737 (1985).

[115] B. Schuh, *Algebraic solution of a non-trivial oscillator problem*, J. Phys. A: Math. Gen. **18**, 803 (1985).

[116] H. W. Jiang and E. Yablonovitch, *Gate-controlled electron spin resonance in GaAs-$Al_xGa_{1-x}As$ heterostructures*, Phys. Rev. B **64**, 041307(R) (2001).

[117] G. Salis, Y. Kato, K. Ensslin, D. C. Driscoll, A. C. Gossard, and D. D. Awschalom, *Electrical control of spin coherence in semiconductor nanostructures*, Nature **414**, 619 (2001).

[118] Y. Kato, R. C. Myers, D. C. Driscoll, A. C. Gossard, J. Levy, D. D. Awschalom, *Gigahertz Electron Spin Manipulation Using Voltage-Controlled g-Tensor Modulation*, Science **299**, 1201 (2003).

[119] N. R. Ogg, *Conduction-band g factor anisotropy in indium antimonide*, Proc. Phys. Soc. **89**, 431 (1966).

[120] B. D. McCombe, *Infrared studies of combined resonance in n-type InSb*, Phys. Rev. **181**, 1206 (1969).

[121] F. Malcher, G. Lommer, U. Rössler, *Electronic states in $GaAs/Ga_{1-x}Al_xAs$ heterostructures: nonparabolicity and spin-splitting*, Superlatt. and Microstruct. **2**, 267 (1986).

[122] P. Pfeffer and W. Zawadzki, *Spin and cyclotron energies of electrons in GaAs/$Ga_{1-x}Al_xAs$ quantum wells*, Phys. Rev. B **74**, 115309 (2006).

[123] A. Malinowski and R. T. Harley, *Anisotropy of the electron g factor in lattice-matched and strained-layer III-V quantum wells*, Phys. Rev. B **62**, 2051 (2000).

[124] E. L. Ivchenko, and A. A. Kiselev, *Elektronnyi g-faktor v kvantovych jamach i sverchreshetkach*, Fiz. Tekh. Poluprov. **26**, 1471 (1992).

[125] J. Fabian, A. Matos-Abiague, Ch. Ertler, P. Stano, and I. Zutic, *Semiconductor Spintronics*, Acta Phys. Slovaca 57, 565-907 (2007).

[126] G. Lommer, F. Malcher, and U. Rössler, *Electron states in GaAs/$Ga_{1-x}Al_xAs$ heterostructures: Subband Landau-levels*, Superlattices and Microstructures **2** 273 (1986).

[127] R. M. Hannak, M. Oestreich, A. P. Heberle, W. W. Rühle, and K. Köhler, *Electron g factor in quantum wells determined by spin quantum beats* Solid State Commun. **93**, 313 (1995).

[128] P. Le Jeune, D. Robart, X. Marie, T. Amand, M. Brousseau, J. Barrau, V. Kalevich and D. Rodichev, *Anisotropy of the electron Landé g factor in quantum wells* Semicon. Sci. and Technol. **12**, 380 (1997).

[129] E. L. Ivchenko, A. A. Kiselev, and M. Willander, *Electronic g-factor in biased quantum wells*, Solid State Comm. **102**, 375 (1997).

[130] A. A. Kiselev, E. L. Ivchenko, and U. Rössler, *Electron g factor in one- and zero-dimensional semiconductor nanostructures*, Phys. Rev. B **58**, 16353 (1998).

[131] R. Winkler, *Spin Orbit Coupling Effects in Two-Dimensional Electron and Hole Systems*, Springer Berlin Heidelberg (2003).

[132] I. Vurgaftman, J. R. Meyer, and L. R. Ram-Mohan, *Band parameters for III-V compound semiconductors and their alloys*, J. Appl. Phys. **89**, 5815 (2001).

[133] F. Dettwiler, J. Fu, S. Mack, P. J. Weigele, J. C. Egues, D. D. Awschalom, and D. M. Zumbühl, *Stretchable Persistent Spin Helices in GaAs Quantum Wells*, Phys. Rev. X **7**, 031010 (2017).

[134] U. Rössler, *Nonparabolicity and warping in the conduction band of GaAs*, Solid State Commun. **49** 943 (1984).

[135] P. S. Alekseev and M. O. Nestoklon, *Effective one-band approach for the spin splittings in quantum wells*, Phys. Rev. B **95**, 125303 (2017).

[136] L. E. Golub and E. L. Ivchenko, *Spin splitting in symmetrical SiGe quantum wells*, Phys. Rev. B **69**, 115333 (2004).

[137] V. K. Kalevich, and V. L. Korenev, *Electron g-factor anisotropy in asymmetric GaAs/AlGaAs quantum well*, J. Exp. Theor. Phys. Lett., **57**, 571 (1993).

[138] D. S. Miserev, A. Srinivasan, O. A. Tkachenko, V. A. Tkachenko, I. Farrer, D. A. Ritchie, A. R. Hamilton, and O. P. Sushkov, *Mechanisms for Strong Anisotropy of In-Plane g-Factors in Hole Based Quantum Point Contacts*, Phys. Rev. Lett. **119**, 116803 (2017).

[139] Vladimir I. Faĺko, B. L. Altshuler, and O. Tsyplyatyev, *Anisotropy of Spin Splitting and Spin Relaxation in Lateral Quantum Dots*, Phys. Rev. Lett. **95**, 076603 (2005).

[140] P. Scarlino, E. Kawakami, P. Stano, M. Shafiei, C. Reichl, W. Wegscheider, and L. M. K. Vandersypen, *Spin-Relaxation Anisotropy in a GaAs Quantum Dot*, Phys. Rev. Lett. **113**, 256802 (2014).

[141] P. Stano and J. Fabian, *Control of electron spin and orbital resonance in quantum dots through spin-orbit interactions*, Phys. Rev. B **77**, 045310 (2008).

[142] G. Lommer, F. Malcher, and U. Rössler, *Reduced g factor of subband Landau levels in AlGaAs/GaAs heterostructures*, Phys. Rev. B **32** 6965 (1985).

[143] M. Dobers, K. v. Klitzing, and G. Weimann, *Electron-spin resonance in the two-dimensional electron gas of GaAs-$Al_xGa_{1-x}As$ heterostructures* Phys. Rev. B **38** 5453 (1988).

[144] A. P. Heberle, W. W. Rühle, and K. Ploog, *Quantum beats of electron Larmor precession in GaAs wells*, Phys. Rev. Lett. **72**, 3887 (1994).

[145] Yu. A. Nefyodov, A. V. Shchepetilnikov, I. V. Kukushkin, W. Dietsche, and S. Schmult, *g-factor anisotropy in a GaAs/$Al_xGa_{1-x}As$*

quantum well probed by electron spin resonance, Phys. Rev. B **83**, 041307(R) (2011).

[146] Yu. A. Nefyodov, A. V. Shchepetilnikov, I. V. Kukushkin, W. Dietsche, and S. Schmult, *Electron g-factor anisotropy in a GaAs/$Al_xGa_{1-x}As$ quantum wells of different symmetry*, Phys. Rev. B **84**, 233302 (2011).

[147] P. S. Eldridge, J. Hübner, S. Oertel, R. T. Harley, M. Henini, and M. Oestreich, *Spin-orbit fields in asymmetric (001)-oriented GaAs/$Al_xGa_{1-x}As$ quantum wells*, Phys. Rev. B **83**, 041301(R) (2011).

[148] P. S. Alekseev, *Anisotropy of the electron g factor in quantum wells based on cubic semiconductors*, Semiconductors **47**, 1241(2013).

[149] Rusko Ruskov, Menno Veldhorst, Andrew S. Dzurak, Charles Tahan, *Electron g-factor of valley states in realistic silicon quantum dots*, arxiv:1708.04555.

[150] R. M. Jock, N. T. Jacobson, P. Harvey-Collard, A. M. Mounce, V. Srinivasa, D. R. Ward, J. Anderson, R. Manginell, J. R. Wendt, M. Rudolph, T. Pluym, J. K. Gamble, A. D. Baczewski, W. M. Witzel and M. S. Carroll, *A silicon metal-oxide-semiconductor electron spin-orbit qubit*, Nature Comm. **9**,1768 (2018).

[151] A. Arora, A. Mandal, S. Chakrabarti, and S. Ghosh, *Magneto-optical Kerr effect spectroscopy based study of Landé g-factor for holes in GaAs/AlGaAs single quantum wells under low magnetic fields*, J. Appl. Phys. **113**, 213505 (2013).

[152] P. Pfeffer and W. Zawadzki, *Anisotropy of spin g factor in GaAs-$Ga_{1-x}Al_xAs$ symmetric quantum wells*, Phys. Rev. B **74**, 233303 (2006).

[153] T. Fujita, T. A. Baart, Ch. Reichl, W. Wegscheider, and L. M. K. Vandersypen, *Coherent shuttle of electron-spin states*, npj Quant. Inf. **3**, 22 (2017).

[154] P. Stano, J. Fabian, *Spin-orbit effects in single-electron states in coupled quantum dots*, Phys. Rev. B **72**, 155410 (2005).

[155] J. Könemann, R. J. Haug, D. K. Maude, V. I. Faĺko, and B. L. Altshuler, *Spin-Orbit Coupling and Anisotropy of Spin Splitting in Quantum Dots*, Phys. Rev. Lett. **94**, 226404 (2005).

[156] W. P. Su, J. R. Schrieffer, and A. J. Heeger, "Solitons in polyacetylene," *Phys. Rev. Lett.*, vol. 42, pp. 1698–1701, 1979.

[157] W. P. Su and J. R. Schrieffer, "Fractionally charged excitations in charge-density-wave systems with commensurability 3," *Phys. Rev. Lett.*, vol. 46, pp. 738–741, 1981.

[158] J. Goldstone and F. Wilczek, "Fractional quantum numbers on solitons," *Phys. Rev. Lett.*, vol. 47, pp. 986–989, 1981.

[159] R. Jackiw and C. Rebbi, "Solitons with fermion number 1/2," *Phys. Rev. D*, vol. 13, pp. 3398–3409, 1976.

[160] R. Jackiw and J. Schrieffer, "Solitons with fermion number 12 in condensed matter and relativistic field theories," *Nuclear Physics B*, vol. 190, no. 2, pp. 253 – 265, 1981.

[161] M. J. Rice and E. J. Mele, "Elementary excitations of a linearly conjugated diatomic polymer," *Phys. Rev. Lett.*, vol. 49, pp. 1455–1459, 1982.

[162] R. Jackiw and G. Semenoff, "Continuum quantum field theory for a linearly conjugated diatomic polymer with fermion fractionization," *Phys. Rev. Lett.*, vol. 50, pp. 439–442, 1983.

[163] S. Kivelson, "Solitons with adjustable charge in a commensurate peierls insulator," *Phys. Rev. B*, vol. 28, pp. 2653–2658, 1983.

[164] X.-L. Qi, T. L. Hughes, and S.-C. Zhang, "Fractional charge and quantized current in the quantum spin hall state," *Nature Physics*, vol. 4, p. 273, 2008.

[165] N. Goldman, I. Satija, P. Nikolic, A. Bermudez, M. A. Martin-Delgado, M. Lewenstein, and I. B. Spielman, "Realistic time-reversal invariant topological insulators with neutral atoms," *Phys. Rev. Lett.*, vol. 105, p. 255302, 2010.

[166] S. Gangadharaiah, L. Trifunovic, and D. Loss, "Localized end states in density modulated quantum wires and rings," *Phys. Rev. Lett.*, vol. 108, p. 136803, 2012.

[167] Y. E. Kraus, Y. Lahini, Z. Ringel, M. Verbin, and O. Zilberberg, "Topological states and adiabatic pumping in quasicrystals," *Phys. Rev. Lett.*, vol. 109, p. 106402, 2012.

[168] J. Klinovaja, P. Stano, and D. Loss, "Transition from fractional to majorana fermions in rashba nanowires," *Phys. Rev. Lett.*, vol. 109, p. 236801, 2012.

[169] J. C. Budich and E. Ardonne, "Fractional topological phase in one-dimensional flat bands with nontrivial topology," *Phys. Rev. B*, vol. 88, p. 035139, 2013.

[170] Z. Xu, L. Li, and S. Chen, "Fractional topological states of dipolar fermions in one-dimensional optical superlattices," *Phys. Rev. Lett.*, vol. 110, p. 215301, 2013.

[171] F. Grusdt, M. Höning, and M. Fleischhauer, "Topological edge states in the one-dimensional superlattice bose-hubbard model," *Phys. Rev. Lett.*, vol. 110, p. 260405, 2013.

[172] J. Klinovaja and D. Loss, "Fractional fermions with non-abelian statistics," *Phys. Rev. Lett.*, vol. 110, p. 126402, 2013.

[173] K. A. Madsen, E. J. Bergholtz, and P. W. Brouwer, "Topological equivalence of crystal and quasicrystal band structures," *Phys. Rev. B*, vol. 88, p. 125118, 2013.

[174] A. V. Poshakinskiy, A. N. Poddubny, L. Pilozzi, and E. L. Ivchenko, "Radiative topological states in resonant photonic crystals," *Phys. Rev. Lett.*, vol. 112, p. 107403, 2014.

[175] D. Rainis, A. Saha, J. Klinovaja, L. Trifunovic, and D. Loss, "Transport signatures of fractional fermions in rashba nanowires," *Phys. Rev. Lett.*, vol. 112, p. 196803, 2014.

[176] J. Klinovaja and D. Loss, "Parafermions in an interacting nanowire bundle," *Phys. Rev. Lett.*, vol. 112, p. 246403, 2014.

[177] R. Wakatsuki, M. Ezawa, Y. Tanaka, and N. Nagaosa, "Fermion fractionalization to majorana fermions in a dimerized kitaev superconductor," *Phys. Rev. B*, vol. 90, p. 014505, 2014.

[178] P. Marra, R. Citro, and C. Ortix, "Fractional quantization of the topological charge pumping in a one-dimensional superlattice," *Phys. Rev. B*, vol. 91, p. 125411, 2015.

[179] J. Klinovaja and D. Loss, "Fermionic and majorana bound states in hybrid nanowires with non-uniform spin-orbit interaction," *The European Physical Journal B*, vol. 88, no. 3, p. 62, 2015.

[180] G. van Miert and C. Ortix, "Excess charges as a probe of one-dimensional topological crystalline insulating phases," *Phys. Rev. B*, vol. 96, p. 235130, 2017.

[181] B. Pérez-González, M. Bello, A. Gómez-León, and G. Platero *arXiv:1802.03973*.

[182] S. Ryu, C. Mudry, C. Hou, and C. Chamon *Phys. Rev. B*, vol. 80, p. 205319, 2009.

[183] B. Seradjeh, C. Weeks, and M. Franz, "Fractionalization in a square-lattice model with time-reversal symmetry," *Phys. Rev. B*, vol. 77, p. 033104, 2008.

[184] A. Rüegg and G. A. Fiete, "Fractionally charged topological point defects on the kagome lattice," *Phys. Rev. B*, vol. 83, p. 165118, 2011.

[185] P. Szumniak, J. Klinovaja, and D. Loss, "Chiral and nonchiral edge states in quantum hall systems with charge density modulation," *Phys. Rev. B*, vol. 93, p. 245308, 2016.

[186] B. A. Volkov and O. Pankratov, "Two-dimensional massless electrons in an inverted contact," *Pi'sma Zh. Eksp. Teor. Fiz.*, vol. 42, p. 145, 1985.

[187] B. A. Bernevig, T. L. Hughes, and S.-C. Zhang, "Quantum spin hall effect and topological phase transition in hgte quantum wells," *Science*, vol. 314, no. 5806, pp. 1757–1761, 2006.

[188] M. König, S. Wiedmann, C. Brüne, A. Roth, H. Buhmann, L. W. Molenkamp, X.-L. Qi, and S.-C. Zhang, "Quantum spin hall insulator state in hgte quantum wells," *Science*, vol. 318, no. 5851, pp. 766–770, 2007.

[189] L. Fu, C. L. Kane, and E. J. Mele, "Topological insulators in three dimensions," *Phys. Rev. Lett.*, vol. 98, p. 106803, 2007.

[190] A. Roth, C. Brüne, H. Buhmann, L. W. Molenkamp, J. Maciejko, X.-L. Qi, and S.-C. Zhang, "Nonlocal transport in the quantum spin hall state," *Science*, vol. 325, no. 5938, pp. 294–297, 2009.

[191] M. Z. Hasan and C. L. Kane, "Colloquium," *Rev. Mod. Phys.*, vol. 82, pp. 3045–3067, 2010.

[192] T. A. Bernevig and T. L. Hughes, *Topological Insulators and Topological Superconductors*. Princeton University Press, 2013.

[193] L. Fu and C. L. Kane, "Superconducting proximity effect and majorana fermions at the surface of a topological insulator," *Phys. Rev. Lett.*, vol. 100, p. 096407, 2008.

[194] M. Sato and S. Fujimoto, "Topological phases of noncentrosymmetric superconductors: Edge states, majorana fermions, and nonabelian statistics," *Phys. Rev. B*, vol. 79, p. 094504, 2009.

[195] R. M. Lutchyn, J. D. Sau, and S. Das Sarma, "Majorana fermions and a topological phase transition in semiconductor-superconductor heterostructures," *Phys. Rev. Lett.*, vol. 105, p. 077001, 2010.

[196] J. Alicea, "Majorana fermions in a tunable semiconductor device," *Phys. Rev. B*, vol. 81, p. 125318, 2010.

[197] A. C. Potter and P. A. Lee, "Majorana end states in multiband microstructures with rashba spin-orbit coupling," *Phys. Rev. B*, vol. 83, p. 094525, 2011.

[198] J. Klinovaja, S. Gangadharaiah, and D. Loss, "Electric-field-induced majorana fermions in armchair carbon nanotubes," *Phys. Rev. Lett.*, vol. 108, p. 196804, 2012.

[199] D. Chevallier, D. Sticlet, P. Simon, and C. Bena, "Mutation of andreev into majorana bound states in long superconductor-normal and superconductor-normal-superconductor junctions," *Phys. Rev. B*, vol. 85, p. 235307, 2012.

[200] S. Nadj-Perge, I. K. Drozdov, B. A. Bernevig, and A. Yazdani, "Proposal for realizing majorana fermions in chains of magnetic atoms on a superconductor," *Phys. Rev. B*, vol. 88, p. 020407, 2013.

[201] F. Pientka, L. I. Glazman, and F. von Oppen, "Topological superconducting phase in helical shiba chains," *Phys. Rev. B*, vol. 88, p. 155420, 2013.

[202] J. Klinovaja, P. Stano, A. Yazdani, and D. Loss, "Topological superconductivity and majorana fermions in rkky systems," *Phys. Rev. Lett.*, vol. 111, p. 186805, 2013.

[203] B. Braunecker and P. Simon, "Interplay between classical magnetic moments and superconductivity in quantum one-dimensional conductors: Toward a self-sustained topological majorana phase," *Phys. Rev. Lett.*, vol. 111, p. 147202, 2013.

[204] M. M. Vazifeh and M. Franz, "Self-organized topological state with majorana fermions," *Phys. Rev. Lett.*, vol. 111, p. 206802, 2013.

[205] M. Thakurathi, A. A. Patel, D. Sen, and A. Dutta, "Floquet generation of majorana end modes and topological invariants," *Phys. Rev. B*, vol. 88, p. 155133, 2013.

[206] F. Maier, J. Klinovaja, and D. Loss, "Majorana fermions in ge/si hole nanowires," *Phys. Rev. B*, vol. 90, p. 195421, 2014.

[207] F. Setiawan, K. Sengupta, I. B. Spielman, and J. D. Sau, "Dynamical detection of topological phase transitions in short-lived atomic systems," *Phys. Rev. Lett.*, vol. 115, p. 190401, 2015.

[208] G. L. Fatin, A. Matos-Abiague, B. Scharf, and I. Žutić, "Wireless majorana bound states: From magnetic tunability to braiding," *Phys. Rev. Lett.*, vol. 117, p. 077002, 2016.

[209] S. Nadj-Perge, I. K. Drozdov, J. Li, H. Chen, S. Jeon, J. Seo, A. H. MacDonald, B. A. Bernevig, and A. Yazdani, "Observation of majorana fermions in ferromagnetic atomic chains on a superconductor," *Science*, vol. 346, no. 6209, pp. 602–607, 2014.

[210] M. Ruby, F. Pientka, Y. Peng, F. von Oppen, B. W. Heinrich, and K. J. Franke, "End states and subgap structure in proximity-coupled chains of magnetic adatoms," *Phys. Rev. Lett.*, vol. 115, p. 197204, 2015.

[211] R. Pawlak, M. Kisiel, J. Klinovaja, T. Meier, S. Kawai, T. Glatzel, D. Loss, and E. Meyer, "Probing atomic structure and majorana wavefunctions in mono-atomic fe chains on superconducting pb surface," *Npj Quantum Information*, vol. 2, p. 16035, 11 2016.

[212] V. Mourik, K. Zuo, S. M. Frolov, S. R. Plissard, E. P. A. M. Bakkers, and L. P. Kouwenhoven, "Signatures of majorana fermions in hybrid superconductor-semiconductor nanowire devices," *Science*, vol. 336, no. 6084, pp. 1003–1007, 2012.

[213] A. Das, Y. Ronen, Y. Most, Y. Oreg, M. Heiblum, and H. Shtrikman, "Zero-bias peaks and splitting in an al-inas nanowire topological superconductor as a signature of majorana fermions," *Nature Physics*, vol. 8, no. 12, p. 887, 2012.

[214] L. P. Rokhinson, X. Liu, and J. K. Furdyna, "The fractional a.c. josephson effect in a semiconductor–superconductor nanowire as a signature of majorana particles," *Nature Physics*, vol. 8, no. 11, p. 795, 2012.

[215] H. O. H. Churchill, V. Fatemi, K. Grove-Rasmussen, M. T. Deng, P. Caroff, H. Q. Xu, and C. M. Marcus, "Superconductor-nanowire devices from tunneling to the multichannel regime: Zero-bias oscillations and magnetoconductance crossover," *Phys. Rev. B*, vol. 87, p. 241401, 2013.

[216] S. M. Albrecht, A. P. Higginbotham, M. Madsen, F. Kuemmeth, T. S. Jespersen, J. Nygård, P. Krogstrup, and C. M. Marcus, "Exponential protection of zero modes in majorana islands," *Nature*, vol. 531, pp. 206–209, 2016.

[217] A. Y. Kitaev, "Fault-tolerant quantum computation by anyons," *Annals of Physics*, vol. 303, no. 1, pp. 2 – 30, 2003.

[218] C. Nayak, S. H. Simon, A. Stern, M. Freedman, and S. Das Sarma, "Non-abelian anyons and topological quantum computation," *Rev. Mod. Phys.*, vol. 80, pp. 1083–1159, 2008.

[219] K. Flensberg, "Non-abelian operations on majorana fermions via single-charge control," *Phys. Rev. Lett.*, vol. 106, p. 090503, 2011.

[220] D. E. Liu and H. U. Baranger, "Detecting a majorana-fermion zero mode using a quantum dot," *Phys. Rev. B*, vol. 84, p. 201308, 2011.

[221] E. Vernek, P. H. Penteado, A. C. Seridonio, and J. C. Egues, "Subtle leakage of a majorana mode into a quantum dot," *Phys. Rev. B*, vol. 89, p. 165314, 2014.

[222] S. Hoffman, C. Schrade, J. Klinovaja, and D. Loss, "Universal quantum computation with hybrid spin-majorana qubits," *Phys. Rev. B*, vol. 94, p. 045316, 2016.

[223] M. T. Deng, S. Vaitiekenas, E. B. Hansen, J. Danon, M. Leijnse, K. Flensberg, J. Nygård, P. Krogstrup, and C. M. Marcus, "Majorana bound state in a coupled quantum-dot hybrid-nanowire system," *Science*, vol. 354, no. 6319, pp. 1557–1562, 2016.

[224] L. S. Ricco, Y. Marques, F. A. Dessotti, R. S. Machado, M. de Souza, and A. C. Seridonio, "Decay of bound states in the continuum of majorana fermions induced by vacuum fluctuations: Proposal of qubit technology," *Phys. Rev. B*, vol. 93, p. 165116, 2016.

[225] F. A. Dessotti, L. S. Ricco, Y. Marques, L. H. Guessi, M. Yoshida, M. S. Figueira, M. de Souza, P. Sodano, and A. C. Seridonio, "Unveiling majorana quasiparticles by a quantum phase transition: Proposal of a current switch," *Phys. Rev. B*, vol. 94, p. 125426, 2016.

[226] L. A. Landau, S. Plugge, E. Sela, A. Altland, S. M. Albrecht, and R. Egger, "Towards realistic implementations of a majorana surface code," *Phys. Rev. Lett.*, vol. 116, p. 050501, 2016.

[227] C. Schrade, S. Hoffman, and D. Loss, "Detecting topological superconductivity with φ_0 josephson junctions," *Phys. Rev. B*, vol. 95, p. 195421, 2017.

[228] L. Xu, X.-Q. Li, and Q.-F. Sun, "Majorana dc josephson current mediated by a quantum dot," *Journal of Physics: Condensed Matter*, vol. 29, no. 19, p. 195301, 2017.

[229] E. Prada, R. Aguado, and P. San-Jose, "Measuring majorana nonlocality and spin structure with a quantum dot," *Phys. Rev. B*, vol. 96, p. 085418, 2017.

[230] L. Fu and C. L. Kane, "Probing neutral majorana fermion edge modes with charge transport," *Phys. Rev. Lett.*, vol. 102, p. 216403, 2009.

[231] E. Prada, P. San-Jose, and R. Aguado, "Transport spectroscopy of ns nanowire junctions with majorana fermions," *Phys. Rev. B*, vol. 86, p. 180503, 2012.

[232] J. S. Lim, R. López, and L. Serra, "Transport through majorana nanowires attached to normal leads," *New Journal of Physics*, vol. 14, no. 8, p. 083020, 2012.

[233] A. A. Zyuzin, D. Rainis, J. Klinovaja, and D. Loss, "Correlations between majorana fermions through a superconductor," *Phys. Rev. Lett.*, vol. 111, p. 056802, 2013.

[234] D. Rainis, L. Trifunovic, J. Klinovaja, and D. Loss, "Towards a realistic transport modeling in a superconducting nanowire with majorana fermions," *Phys. Rev. B*, vol. 87, p. 024515, 2013.

[235] A. Zazunov, A. Altland, and R. Egger, "Transport properties of the coulomb–majorana junction," *New Journal of Physics*, vol. 16, no. 1, p. 015010, 2014.

[236] L. Weithofer, P. Recher, and T. L. Schmidt, "Electron transport in multiterminal networks of majorana bound states," *Phys. Rev. B*, vol. 90, p. 205416, 2014.

[237] F. m. c. Crépin, B. Trauzettel, and F. Dolcini, "Signatures of majorana bound states in transport properties of hybrid structures based on helical liquids," *Phys. Rev. B*, vol. 89, p. 205115, 2014.

[238] W. S. Cole, J. D. Sau, and S. Das Sarma, "Proximity effect and majorana bound states in clean semiconductor nanowires coupled to disordered superconductors," *Phys. Rev. B*, vol. 94, p. 140505, 2016.

[239] P. Szumniak, D. Chevallier, D. Loss, and J. Klinovaja, "Spin and charge signatures of topological superconductivity in rashba nanowires," *Phys. Rev. B*, vol. 96, p. 041401, 2017.

[240] D. Sticlet, C. Bena, and P. Simon, "Spin and majorana polarization in topological superconducting wires," *Phys. Rev. Lett.*, vol. 108, p. 096802, 2012.

[241] M. Guigou, N. Sedlmayr, J. M. Aguiar-Hualde, and C. Bena, "Signature of a topological phase transition in long sn junctions in the spin-polarized density of states," *EPL*, vol. 115, no. 4, p. 47005, 2016.

[242] D. Stanescu and S. Tewari *Journal of the Indian Institute of Science*, vol. 96, no. 2, p. 107, 2016.

[243] C.-X. Liu, J. D. Sau, T. D. Stanescu, and S. Das Sarma, "Andreev bound states versus majorana bound states in quantum dot-nanowire-superconductor hybrid structures: Trivial versus topological zero-bias conductance peaks," *Phys. Rev. B*, vol. 96, p. 075161, 2017.

[244] C. Moore, T. D. Stanescu, and S. Tewari *arXiv:1711.06256*.

[245] Y.-H. Chan, C.-K. Chiu, and K. Sun, "Multiple signatures of topological transitions for interacting fermions in chain lattices," *Phys. Rev. B*, vol. 92, p. 104514, 2015.

[246] T. Gulden, M. Janas, Y. Wang, and A. Kamenev, "Universal finite-size scaling around topological quantum phase transitions," *Phys. Rev. Lett.*, vol. 116, p. 026402, 2016.

[247] J.-H. Park, G. Yang, J. Klinovaja, P. Stano, and D. Loss, "Fractional boundary charges in quantum dot arrays with density modulation," *Phys. Rev. B*, vol. 94, p. 075416, 2016.

[248] W. Wernsdorfer, "From micro- to nano-squids: applications to nanomagnetism," *Superconductor Science and Technology*, vol. 22, no. 6, p. 064013, 2009.

[249] P. Stano, J. Klinovaja, A. Yacoby, and D. Loss, "Local spin susceptibilities of low-dimensional electron systems," *Phys. Rev. B*, vol. 88, p. 045441, 2013.

[250] T. Staudacher, F. Shi, S. Pezzagna, J. Meijer, J. Du, C. A. Meriles, F. Reinhard, and J. Wrachtrup, "Nuclear magnetic resonance spectroscopy on a (5-nanometer)3 sample volume," *Science*, vol. 339, no. 6119, pp. 561–563, 2013.

[251] L. Trifunovic, F. L. Pedrocchi, S. Hoffman, P. Maletinsky, A. Yacoby, and D. Loss, "High-efficiency resonant amplification of weak magnetic fields for single spin magnetometry at room temperature," *Nature Nanotechnology*, vol. 10, p. 541, 2015.

[252] M. J. Martínez-Pérez, B. Müller, D. Schwebius, D. Korinski, R. Kleiner, J. Sesé, and D. Koelle, "Nanosquid magnetometry of individual cobalt nanoparticles grown by focused electron beam induced deposition," *Superconductor Science and Technology*, vol. 30, no. 2, p. 024003, 2017.

[253] L. Thiel, D. Rohner, M. Ganzhorn, P. Appel, E. Neu, B. Müller, R. Kleiner, D. Koelle, and P. Maletinsky, "Quantitative nanoscale vortex imaging using a cryogenic quantum magnetometer," *Nature Nanotechnology*, vol. 11, pp. 677–981, 2016.

[254] S. Tewari, J. D. Sau, V. W. Scarola, C. Zhang, and S. Das Sarma, "Probing a topological quantum critical point in semiconductor-superconductor heterostructures," *Phys. Rev. B*, vol. 85, p. 155302, 2012.

Marcel Serina

Personal Data

Place and Date of Birth:	Trnava, Slovakia | 29 October 1990
Address:	Colmarerstrasse 26, 4055 Basel, Switzerland
Phone:	+41765111247
email:	marcel.serina@unibas.ch

Work Experience

Sep 2014-Sep 2018 | PhD. Student at University of Basel, Basel
Under supervision of Prof. Daniel Loss

Aug-Sep 2013, Aug 2012 | Research Assistant at Slovak Academy of Sciences, Bratislava
Learned fundamental principles of CTMRG algorithm for 2D lattice under supervision of Dr. Andrej Gendiar.

Sep 2010-Jun 2010 | Voluntary Lecturer at Gymnázium Jána Holleho, Trnava
Led voluntary lectures of elementar calculus for students ending high school, which were interested in maths and wanted to study science in the future.

Education

Jun 2014 Master Degree in Theoretical Physics, **Commenius University**, Bratislava, Slovakia
Major: Condensed Matter Theory, Particle Physics, Mathematical Physics
Thesis: "Phase transition analysis in asymptotic non-Euclidean geometries"
Advisor: Dr. Andrej Gendiar

Jun 2012 Bachelor Degree in Physics, **Commenius University**, Bratislava, Slovakia
Thesis: "Symmetries of Kepler problem and Runge-Lenz vector"
Advisor: Dr. Marián Fecko

May 2009 Graduation at **Gymnázium Jána Holleho**, Trnava, Slovakia